

FUJITSU

SCIENTIFIC & TECHNICAL JOURNAL

Winter 1989 VOL.25, NO.4

Special Issue on Printers and I/O Technology





(By Rei Watanabe, 1989)

This Issue's Cover:

The ideograph on the cover, "soh", means to bring into existence or to create. In Japanese, this character is used to express creativity.

The beginnings of the electronics industry in Japan closely mirrored European technology. Today however, advancement in electronics R&D has led to the creation of more original technology. Japan has entered the age of "soh".

Fujitsu is promoting its unique R&D to create original technology which contributes to the prosperity of communities everywhere.

FUJITSU Scientific & Technical Journal is published quarterly by FUJITSU LIMITED of Japan to report the results of research conducted by FUJITSU LIMITED, FUJITSU LABORATORIES LTD., and their associated companies in communications, electronics, and related fields. It is the publisher's intent that FSTJ will promote the international exchange of such information, and we encourage the distribution of FSTJ on an exchange basis. All correspondence concerning the exchange of periodicals should be addressed to the editor.

FSTJ can be purchased through KINOKUNIYA COMPANY LTD., 3-17-7 Shinjuku, Shinjuku-ku, Tokyo 160-91, (Telex No. 2424344, answerback KINOKUNI J).

The price is US \$5.00 per copy, without consumption tax, excluding postage.

FUJITSU LIMITED reserves all rights concerning the republication and publication after translation into other languages of articles appearing herein.

Permission to publish these articles may be obtained by contacting the editor.

FUJITSU LIMITED

Takuma Yamamoto, *President*

FUJITSU LABORATORIES LTD.

Masaka Ogi, *President*

Editorial Board

Editor Takahiko Misugi

Associated Editors Yukio Fukukawa Shigeru Sato

Editorial Representatives

Kunihiko Asama	Masakazu Fujita	Tatsuzumi Furukawa
Kazuhisa Kobayashi	Masaaki Kobayashi	Yoshimasa Miura
Makoto Mukai	Seiya Ogawa	Shinji Ohkawa
Shinya Okuda	Hirofumi Okuyama	Tohru Sato
Yoshio Tago	Shozo Taguchi	Jyun'ichi Tanahashi
Hirobumi Takanashi	Mitsuhiko Toda	Toru Tsuda
Akira Yoshida		

Editorial Coordinator

Kazuo Yono

FUJITSU LIMITED 1015 Kamikodanaka, Nakahara-ku,
Kawasaki 211, Japan

Cable Address: FUJITSULIMITED KAWASAKI

Telephone: +81-44-777-1111

Telex: 3842122, 3842221, 3842802, 3842803,

Answerback FTWKAW J

Printed by MIZUNO PRITECH Co., Ltd. in Japan

© 1990 FUJITSU LIMITED (January 25, 1990)

CONTENTS

Featuring Papers

Preface

249 **Special Issue Featuring Six Papers on Printers and I/O Technology**

● Takefumi Inagaki

251 **An Analysis of Two-Component Magnetic Brush Development**

● Masatoshi Kimura

● Makoto Kato

● Junzo Nakajima

262 **The Electrostatic Transfer of Toner Images**

● Masatoshi Kimura

● Masahiro Wanou

● Hiroshi Nou

272 **Color Gamut Evaluation Method for Color Hard Copies**

● Jun Moroo

● Toshio Konaka

● Tomohisa Mikami

279 **A Filter-Alternating Color Scanner**

● Shoji Suzuki

● Mitsuhiro Tsuda

● Masahiro Mori

287 **Holographic Fingerprint Sensor**

● Seigo Igaki

● Shin Eguchi

● Takashi Shinzaki

297 **Wavelength Independent Grating Lens System**

● Masayuki Kato

● Satoshi Maeda

● Fumio Yamagishi

Papers

306 **SVEX: Switching Program Verification Expert System**

● Jun'ichi Yamazaki

● Kiyoshi Miyazaki

● Tadamichi Suzuki

313 **Compact Three-Axis Accelerometer System (CTAS) for Microgravity Experiments**

● Fumio Takei

317 **Soft X-Ray Lithography Using Synchrotron Radiation**

● Yoshimi Yamashita

● Syunji Gotoh

● Hidetoshi Ishiwari

UDC 537.621:77.023.46:772.93

FUJITSU Sci. Tech. J., 25, 4, pp. 251-261(1990)

An Analysis of Two-Component Magnetic Brush Development

• Masatoshi Kimura • Makoto Kato • Junzo Nakajima

Two types of magnetic brush development using conductive and non-conductive carriers have been studied theoretically and experimentally. In the analysis, the relationship between developed toner mass and primary development factors, such as toner layer potential, toner charge to mass ratio, recording layer capacity and developer flow rate, has been investigated. The calculations agree well with the measurements.

This expression clarifies the parameters needed to obtain the required optical density of the developed image.

UDC 681.327.12

FUJITSU Sci. Tech. J., 25, 4, pp. 279-286(1990)

A Filter-Alternating Color Scanner

• Shoji Suzuki • Mitsuhiro Tsuda • Masahiro Mori

A small and fast color scanner having precise color digitization has been developed. The scanner was designed using colorimetric simulation so that its characteristics match the RGB standard response. The filters and compensation matrix are adjusted to minimize color differences between the simulated and measured colors of the CIELAB color specimens.

A filter-alternating mechanism for color separation was developed. A transparent filter is used for high speed monochrome scanning.

The prototype scanner features excellent color performance, an average color difference of seven, and high speed monochrome scanning (six seconds for an ISO A4-size document). This color scanner is as small as a monochrome scanner.

UDC 681.327.5:681.621.83

FUJITSU Sci. Tech. J., 25, 4, pp. 262-271(1990)

The Electrostatic Transfer of Toner Images

• Masatoshi Kimura • Masahiro Wanou • Hiroshi Nou

Electrostatic toner image transfer has been studied theoretically and experimentally. Three transfer methods have been investigated: corona transfer, conductive roller transfer, and dielectric roller transfer.

It has been shown theoretically and experimentally that the dependence of the transfer ratio on the electric field between transfer material and toner layer is the same for all three methods. The optimum toner charge to mass ratio gives a maximum transfer ratio. Theory suggests that the maximum transfer speed is 6.7 m/s for corona transfer and 125 m/s for roller transfer.

Toner images are transferred to plain paper with a transfer ratio above 80 percent at a paper speeds up to 2 m/s.

UDC 343.982:681.183

FUJITSU Sci. Tech. J., 25, 4, pp. 287-296(1990)

Holographic Fingerprint Sensor

• Seigo Igaki • Shin Eguchi • Takashi Shinzaki

A sensor for personnel identification that uses a laser light source has been developed. It consists of a transparent light-conducting glass plate with a plain grating hologram, and a focusing lens under the hologram. Because the plate is plane-parallel, all optical paths from each point on the fingerprint to the hologram are equal, and a bright fingerprint image is obtained without the trapezoidal distortion inherent in prism sensors.

UDC 681.6.62:778.63

FUJITSU Sci. Tech. J., 25, 4, pp. 272-278(1990)

Color Gamut Evaluation Method for Color Hard Copies

• Jun Moroo • Toshio Konaka • Tomohisa Mikami

In this paper, an image quality evaluation method for color gamut is studied. In subjective assessments for color gamut in color hard copies, color wedges were found to be more useful than natural images for designing color devices.

Furthermore, it is also shown by experiment that unwanted density can be assessed in addition to primary density by calculating a block ink density whose color hexagon inscribes that of actual inks.

UDC 681.7.066

FUJITSU Sci. Tech. J., 25, 4, pp. 297-305(1990)

Wavelength Independent Grating Lens System

• Masayuki Kato • Satoshi Maeda • Fumio Yamagishi

Grating lenses can be made small and light, and can be mass-produced. However, wavelength variations in the light source cause aberrations and change the focal length of the grating lens. Therefore, it has been difficult to use grating lenses in high-precision optical systems that use light sources with wavelength variation. A new grating lens system with a high numerical aperture was proposed to suppress the aberration and keep the focal length constant over a wavelength range of a few tens of nanometers. Aberration calculations showed that the acceptable wavelength range was ± 15 nm for a system with a numerical aperture of 0.50. The gratings were made using electron beam lithography, and their focusing ability was then evaluated.

UDC 001.81:621.395.345:681.3.06
FUJITSU Sci. Tech. J., **25**, 4, pp. 306-312(1990)

SVEX: Switching Program Verification Expert System

• Jun'ichi Yamazaki • Kiyoshi Miyazaki • Tadamichi Suzuki

This paper describes SVEX, which can automatically find errors in switching programs. SVEX can also generate service specifications from the programs for testers to confirm that the programs meet the original specifications.

SVEX simulates switching on an object-oriented model of a target switching system. Logic errors are found by comparing the behavior of the model with the verification rules represented by demands. State transition diagrams are generated by tracing the behavior of the model.

SVEX has been applied to the development of Fujitsu's digital PBXs. SVEX has found 72 percent of all errors in logic, including some errors overlooked by the usual online testing.

UDC 621.3.049.77:77.022
FUJITSU Sci. Tech. J., **25**, 4, pp. 317-324(1990)

Soft X-Ray Lithography Using Synchrotron Radiation

• Yoshimi Yamashita • Syunji Gotoh • Hidetoshi Ishiwari

The BL-17C beamline was constructed for soft X-ray lithography at the Photon Factory of the National Laboratory for High Energy Physics. Research on the fundamental characteristics of pattern replication has been conducted using the beamline.

This report describes replicated resist pattern profiles and pattern replication accuracy. A method of accuracy evaluation was proposed and the exposure conditions necessary for accurate replication using positive resist (CMR) were obtained.

These results indicated a fair possibility of high replication accuracy in sub quarter-micron patterns.

UDC 528.27:629.78
FUJITSU Sci. Tech. J., **25**, 4, pp. 313-316(1990)

Compact Three-Axis Accelerometer System (CTAS) for Microgravity Experiments

• Fumio Takei

The measurement of the acceleration environment in microgravity experiments is very important. Conventional accelerometer systems, however, are too large and bulky for microgravity experiments. A microcomputer-based compact system that uses a static memory IC module for data storage was developed. The system's servo accelerometers ensure its accuracy and reliability. Usefulness of the system was verified in a microgravity experiment on-board NASA's KC-135, which is designed for parabolic flight.

Special Issue Featuring Six Papers on Printers and I/O Technology

● Takefumi Inagaki

Electronic Systems Division, Fujitsu Laboratories Ltd.

The networking and personal use of computer systems are now rapidly advancing. The equipment with which people come into direct contact, for example, printers and I/O devices, is becoming increasingly important. The next six papers introduce the research on printers and I/O devices conducted by the Electronic Systems Division of Fujitsu Laboratories.

Printers are now making the transition from impact printers (IP) to nonimpact printers (NIP). Because electrophotographic printers can print high-quality characters more quietly than any other types of printer, a wide range of models are now being developed. These new printers range from large printers for computer peripheral devices to the small desktop printers that have recently appeared in great numbers. For electrophotographic printers, an electrophotographic process that ensures high reliability and high printing quality must be developed. In particular, the reliability of the developing and transfer processes must be improved.

This increase cannot be achieved simply by trial and error, and research and development based on theory is necessary. *An Analysis of Two-Component Magnetic Brush Development*, the first of this special issue describes advances made in the development process. The development process is the key to electrophotographic printing. To determine the development conditions required to obtain toner images that are dark enough for the photoconductive drum, various models and formulas for the development process have been developed. These models and formulas enable optimum design of the entire development process, including the physical characteristics of the photoconductive drum and developer. The second, *The Electrostatic Transfer of Toner Images* describes the results of research to find the transfer process conditions under which a toner image on the photoconductive drum is most efficiently transferred to paper. From our modeling and formulation of the transfer process, it was clear that the transfer efficiency is solely determined by the transfer charge on the paper. In the above two papers, we describe the physical phenomena observed during the development and transfer processes. These observations were used to obtain a theoretical and practical understanding of the electrophotographic process, and to determine the optimum design conditions for the process.

There is an increasing demand for printers and I/O devices that can process color images. For this reason, devices that take human vision into consideration and methods to evaluate such devices are becoming important. *Color Gamut Evaluation Method for Color Hard Copies* describes the results of our research on evaluation methods for the color gamut for color hard copies. After repeated subjective assessments, it was found that to evaluate color images, it is more effective to use color wedges such as yellow, magenta, cyan, red, green, blue, and black than to use the natural images we usually see. A color image device design standard that use this method was developed. By using this method, we can predict subjective assessment values from the physical characteristics of the color image device. *A Filter-Alternating Color Scanner* describes the technology used in the filter-alternating color scanners that digitize the color images. This paper also describes an optical mechanism and algorithm that were developed to produce a device that takes human vision into consideration.

Conventional optical devices such as lenses, prisms, and mirrors are often used in I/O devices, and recent times have also seen the employment in I/O devices of advanced optical technology, especially lasers.

To satisfy the requirements for small, lightweight, and high-performance devices, the development of an optical device based on new principles is anticipated. Recently, holography, which is well known for its use in three-dimensional image reconstruction, has drawn considerable attention because it offers a variety of optical modulations using optical diffraction in spite of its thin structure. *Holographic Fingerprint Sensor* describes an optical sensor system for realtime fingerprint identification that uses Fujitsu's hologram technology. Because the number of people who access computer systems is increasing, it is very important to manage computer security. The use of fingerprints in this area is promising because they are fixed and unique. Unlike conventional prism systems, holograms do not distort input fingerprint images. They can reduce the load of the fingerprint verification algorithm and enable development of a high recognition performance system. *Wavelength Independent Grating Lens System* processes a new lens structure using typical holographic optical elements (HOEs). Unlike conventional holographic lenses, these lenses can be used with diode lasers having unstable wavelengths. The theory and experiments demonstrate their effectiveness.

As described above, these six papers introduce a wide range of technologies: from processes that can be applied to printers and I/O devices; to devices, systems, and algorithms. Before starting this research and development, we must set clear targets by anticipating market demands, and we must also understand the physical phenomena involved by using new theories and concepts.

We hope that these six papers will help you understand our basic attitude towards research on printers and I/O devices.

The Electronic Systems Division is conducting research and development in the important field of production engineering. Fujitsu's gross sales now exceeds two trillion (10^{12}) yen, and therefore, a standardized high-level of production engineering is indispensable. The next issue will introduce the production engineering technology that has been developed with the Corporate Production Engineering Group.

UDC 537.621:77.023.46:772.93

An Analysis of Two-Component Magnetic Brush Development

• Masatoshi Kimura • Makoto Kato • Junzo Nakajima

(Manuscript received November 1, 1989)

Two types of magnetic brush development using conductive and non-conductive carriers have been studied theoretically and experimentally. In the analysis, the relationship between developed toner mass and primary development factors, such as toner layer potential, toner charge to mass ratio, recording layer capacity and developer flow rate, has been investigated. The calculations agree well with the measurements.

This expression clarifies the parameters needed to obtain the required optical density of the developed image.

1. Introduction

Two-component magnetic brush development is widely used in electrophotography and electrostatic recording because it is dry and develops quickly. This paper explains our systematic study of the magnetic brush development process, focusing on the quantitative analysis of the developed toner on the recording layer.

Many studies have been done on this type of development¹⁾⁻¹¹⁾. Studies dealing with the developed toner mass can be classified into two types. The first one uses the potentials of the developed toner layer on the recording layer to determine the relationship between various development factors and the developed toner mass. This is called static analysis. The second type is dynamic analysis, which includes velocity-related factors such as the speed of recording drum and the magnetic brush.

Kutsuwada used static analysis to determine the relationship between the potential of the latent image and the developed toner mass by calculating the surface potential of the developed recording layer^{2),3)}. His group also studied the electrostatic force acting on the toner during developing. Kondo used static analysis to study the quantitative relationship

between the potential of the developed toner layer and the developed toner mass⁴⁾. Static analysis is based on potential calculation and is best suited to examine the development process before the latent image is completely filled with the charged toner. However, static analysis is limited because velocity-related factors which greatly influence development are not considered. Dynamic analysis is required to design development units. Schein and Harpavat made important studies in dynamic analysis. Both researchers used the ratio between the peripheral speed of the recording drum and that of the magnetic brush as a principal parameter. Schein studied the relationship between this parameter and the developed toner mass⁶⁾. Harpavat studied the influence of various development factors theoretically⁷⁾.

The above studies are important, but both static analysis and dynamic one have not been adequately conducted for the requirements for the latent and the developed images to achieve the necessary developed density. Among the dynamic-analysis studies, Schein dealt with the toner adhering to the conductive surface⁶⁾. He failed to consider the recording layer capacity which greatly influences development. He did not deal with the influence of the

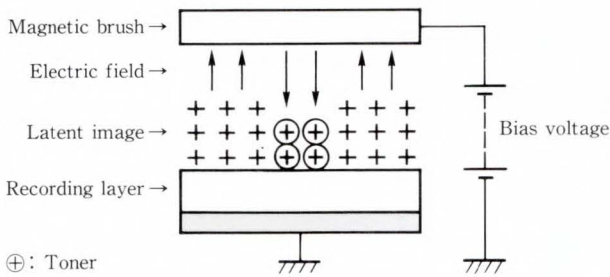


Fig. 1—Reversal development.

toner charge to mass ratio. Harpavat calculated the relationship between the primary development factors and the developed toner mass⁷⁾. However, he lacked measurements to back up his conclusions. In addition, his analysis was complex. Both studies were unclear in relation to the results from static analysis.

The authors theoretically and experimentally studied the relationship between development factors and the developed toner mass. In particular, the authors examined recording material, developer, latent image strength, and the developing conditions needed to obtain the necessary developed density. The study combined static analysis and dynamic one in a consistent manner. The authors have also developed a quantitative model based on a consistent theory of dynamic development that includes static analysis. The authors used this model to clarify the requirements for latent images to obtain sufficient developed density.

2. Theoretical analysis

In reversal development, a toner with the same polarity as the latent image (here, we will talk about a case of positively charged toner) is attracted to the discharged part of the latent image (see Fig. 1). This chapter deals with the relationship between the primary development factors and the developed toner mass through static analysis and dynamic one.

The reason this toner sticks is the same in forward development.

2.1 Static analysis^{12), 13)}

Figure 2 shows a model of the toner after

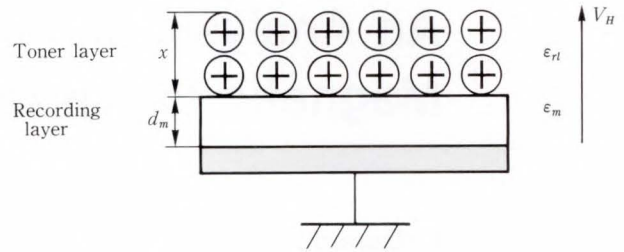


Fig. 2—Toner charge on the recording layer.

saturated development. The developed toner mass *M* is obtained using this model, where *M* represents the mass of the toner adhering to a unit recording area. MKS units are used for this calculation. Let the thickness of toner layer be *x*, then the surface potential of the toner layer *V_H* is given by:

$$V_H = \int_0^x \frac{\rho(x-s)}{\epsilon_0 \epsilon_{rl}} ds + \frac{\rho x + Q_0}{\epsilon_0 \epsilon_m} d_m$$

$$= \frac{1}{2} \frac{\rho x^2}{\epsilon_0 \epsilon_{rl}} + \frac{\rho x d_m}{\epsilon_0 \epsilon_m} + \frac{Q_0 d_m}{\epsilon_0 \epsilon_m}, \dots \dots (1)$$

- where, ρ : volume charge density of developed toner layer
- ϵ_0 : dielectric constant of vacuum
- ϵ_m : relative dielectric constant of recording layer
- ϵ_{rl} : relative dielectric constant of toner layer
- d_m : thickness of recording layer
- Q_0 : initial charge of recording layer per unit area
- s : toner layer thickness (variable for integration).

The first term is the voltage which the toner layer produces by itself, the second term is the voltage produced on the recording layer by the toner charge, and the third term is the initial surface potential of the recording layer before developing.

Let *V₀* be the initial surface potential of the recording layer and *V_t* be the surface potential generated by the developed toner on recording layer. This is called the toner layer potential.

The toner layer potential *V_t* is given by:

$$V_t = V_H - V_0 \dots \dots \dots (2)$$

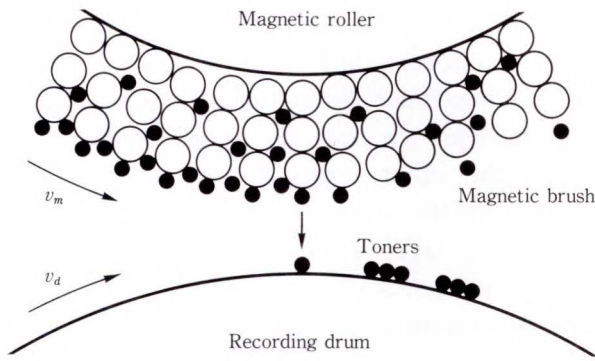


Fig. 3—Developer.

Substituting Equation (2) into Equation (1) and solving for x , we obtain

$$x = -\frac{\epsilon_{rl}d_m}{\epsilon_m} + \sqrt{\left(\frac{\epsilon_{rl}d_m}{\epsilon_m}\right)^2 + 2\frac{\epsilon_0\epsilon_{rl}}{\rho}V_t} \dots (3)$$

The volume charge density ρ of the toner layer is given by:

$$\rho = \delta p \frac{q}{m}, \dots (4)$$

- where, δ : toner density
- p : packing density of toner layer
- $\frac{q}{m}$: toner charge to mass ratio.

Using Equations (3) and (4), the developed toner mass per unit area M is given by:

$$M = \delta p x = \delta p \left\{ -\frac{\epsilon_{rl}d_m}{\epsilon_m} + \sqrt{\left(\frac{\epsilon_{rl}d_m}{\epsilon_m}\right)^2 + 2\frac{\epsilon_0\epsilon_{rl}}{\delta p \frac{q}{m}}V_t} \right\} \dots (5)$$

Thus, developed toner mass per unit area is determined by toner density, packing density of toner layer, ratio of the relative dielectric constant of recording layer to the thickness of recording layer $\frac{d_m}{\epsilon_m}$ (this can be determined from the capacity of the recording layer), toner

charge to mass ratio $\frac{q}{m}$ and toner layer potential

V_t . The most important of these are the capacity of recording layer, the toner charge to mass ratio, and the toner layer potential.

2.2 Dynamic analysis^{14),15)}

We considered a development process where the recording layer moves at a velocity v_d and the magnetic brush moves at a velocity v_m as shown in Fig. 3.

The developer flow rate θ is defined by:

$$\theta = n \frac{v_m}{v_d}, \dots (6)$$

where, n : development repetitions.

Developing is divided into two steps: supplying toner and transferring toner to the recording layer by electrostatic force. The first step is evaluated by the developer flow rate θ and the second step is evaluated by the electric flux density in the developing area. The electric flux density is expressed as the product $\epsilon_0 E(x)$ of the electric field $E(x)$ which is a function of the toner layer x and the dielectric constant ϵ_0 of vacuum.

Here, we will examine developed toner charge per unit area Q which is proportional to developed toner mass per unit area M . We assume that the differential of Q is proportional to the differential of developer flow rate $d\theta$ and dielectric flux density $\epsilon_0 E(x)$.

The following equation is obtained:

$$dQ = \gamma \epsilon_0 E(x) d\theta, \dots (7)$$

where, γ : proportionality constant.

The developed toner charge per unit area Q is expressed by the thickness of the developed toner layer and the volume charge density.

$$Q = \rho x. \dots (8)$$

Using Equation (8), Equation (7) can be written

$$\frac{dx}{d\theta} = \gamma \frac{\epsilon_0 E(x)}{\rho}. \dots (9)$$

When this differential equation is solved, the relationship between the mass of stuck toner

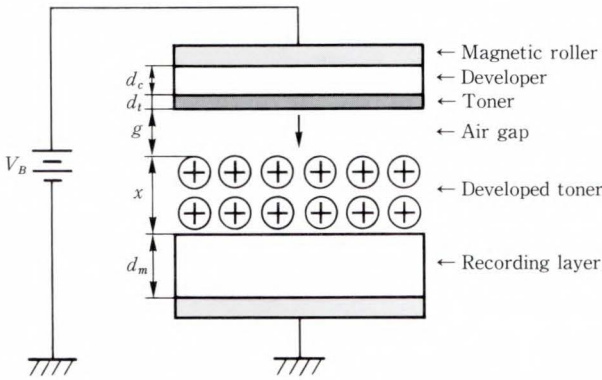


Fig. 4—Magnetic brush development.

and various factors, including the developer flow rate, is obtained.

First, let us determine the electric field $E(x)$ across the air gap using the model in Fig. 4. The charged toner layer with a thickness of x is stuck to the recording layer d_m thick, and the toner layer d_t is above the magnetic brush with gap g between the two. The magnetic brush consists of the developer thickness d_c .

$E(x)$ across the air gap is given by:

$$E(x) = \frac{V_{ts} - \left(\frac{\rho x^2}{2\epsilon_0 \epsilon_{rl}} + \frac{\rho x}{\epsilon_0 \epsilon_m} d_m \right)}{\frac{x}{\epsilon_{rl}} + g + \frac{d_m}{\epsilon_m} + \frac{d_t}{\epsilon_{rl}} + \frac{d_c}{\epsilon_c}}, \quad (10)$$

where, ϵ_c is the relative dielectric constant of developer.

V_{ts} is the toner layer potential in the saturated state. It is obtained by subtracting the voltage corresponding to the adhesion between a toner and a carrier particle from the potential difference (effective latent image strength) between the magnetic roller bias voltage and the initial surface potential of recording layer. The term in parentheses is the voltage resulting from the adhesion of toner to the recording layer, or the toner layer potential V_t . When the toner voltage reaches V_{ts} , the electric field across the air gap becomes 0, stopping developing. The terms in the denominator in Equation (10) are the effective thickness of the stuck toner layer, the gap, the effective thickness of the recording layer,

the effective thickness of the toner layer on the developer, and the effective thickness of the developer. Since the air gap is considered to be $1 \mu\text{m}$ or less, it is negligible compared with the other terms. Since the toner layer stuck to the developer is transferred to the recording layer after development and is included in x , d_t is also negligible.

Substituting Equation (10) into Equation (9), we calculate the developed toner layer x under two conditions. When the conductive carrier is used, coating layer thickness is zero, and when the non-conductive carrier is used, d_c is not negligible.

The developed toner mass M is given by:

$$M = \delta p x \quad \dots \dots \dots (11)$$

Using Equation (4) which gives the volume charge density, the developed toner mass M is given by the following equations:

1) When a conductive carrier is used

$$M = \delta p x = \delta p \left\{ - \frac{\epsilon_{rl} d_m}{\epsilon_m} + \sqrt{\left(\frac{\epsilon_{rl} d_m}{\epsilon_m} \right)^2 + \frac{2 \epsilon_0 \epsilon_{rl}}{\delta p \frac{q}{m}} V_t} \right\}, \quad (12)$$

where, $V_t = V_{ts}(1 - e^{-r\theta})$. $\dots \dots \dots (13)$

Equations (12) and (13) are the basic equations for dynamic analysis. Equation (12) indicates the developed toner mass when a toner voltage is given. Equation (13) indicates how the toner layer potential V_t is determined in the development process.

2) When a non-conductive carrier is used

$$M = \delta p \left\{ \frac{(B^2 - A^2) \left(1 - e^{-\frac{r}{L \epsilon_{rl}} B \theta} \right)}{(B - A) e^{-\frac{rB}{L \epsilon_{rl}} \theta} + (A + B)} \right\}, \quad \dots \dots \dots (14)$$

where, $A = \frac{\epsilon_{rl}}{\epsilon_m} d_m$, $\dots \dots \dots (15)$

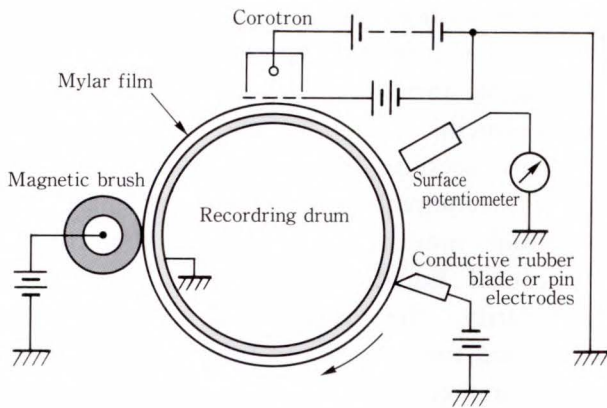


Fig. 5—Test setup.

$$B = \sqrt{\left(\frac{\epsilon_r d_m}{\epsilon_m}\right)^2 + \frac{2\epsilon_0 \epsilon_r}{\delta p \frac{q}{m}} V_{ts}} \quad (18)$$

$$L = \frac{d_m}{\epsilon_m} + \frac{d_c}{\epsilon_c} \quad \dots\dots\dots (17)$$

3) If developer flow rate is very large, Equations (12) and (14) can be reduced to:

$$M = \delta p \left\{ -\frac{\epsilon_r d_m}{\epsilon_m} + \sqrt{\left(\frac{\epsilon_r d_m}{\epsilon_m}\right)^2 + \frac{2\epsilon_0 \epsilon_r}{\delta p \frac{q}{m}} V_{ts}} \right\} \quad \dots\dots\dots (18)$$

Equation (18) agrees with Equation (5) which comes from static analysis. Thus, this dynamic analysis is consistent with static analysis.

The relationship between the developed toner mass and the primary development parameters will be clarified later through calculations based on these equations as well as measurements.

3. Method of experiment

We measured the relationship between the developed toner mass and the optical density to determine the developed toner mass required for practical use. We then measured the surface

potential of the recording layer after development and established a potential model for the saturated state. We also clarified the relationship between the developed toner mass and the primary parameters, such as the capacity of the recording layer, the toner charge to mass ratio, and the toner layer potential.

Figure 5 shows the test setup. The recording drum was a metal drum coated with Mylar film with metal vapor-deposited on the back. Around the recording drum were a corotron with a mesh for uniform charging, a conductive rubber blade or pin electrodes for latent image formation, a magnetic brush developer, and a surface potentiometer. The Mylar films were 25 μm thick (with a capacitance of 1.13 μF/m²) and 50 μm (0.57 μF/m²). The developer was a mixture of carrier and toner at a weight concentration of five percent. The carriers were 100 μm to 200 μm iron particles with irregular shapes. Three types of positively charged toner with different charges were used. The diameter of the toner particles was 10 μm to 20 μm.

Latent image formation and developing are briefly explained below:

1) Uniform charging

The recording layer is uniformly charged by a corotron with a mesh to a positive potential and we measured the charging potential V_{s0} with the surface potentiometer.

2) Latent image formation

We used a conductive rubber blade with a negative bias voltage is applied and put it into contact with the recording layer to remove charges from the recording layer. Since a developing potential model is used, we measured the potential V_0 after removing the charge using a non-contact pin electrode.

3) Developing

We applied the development bias potential V_B to the developing roller. Toner was transferred to the area without charges by reversal development to obtain a solid black area. After developing, we measured the potentials on the latent image (V_H) and the uniformly charged area (V_s).

4) Toner layer potential V_t

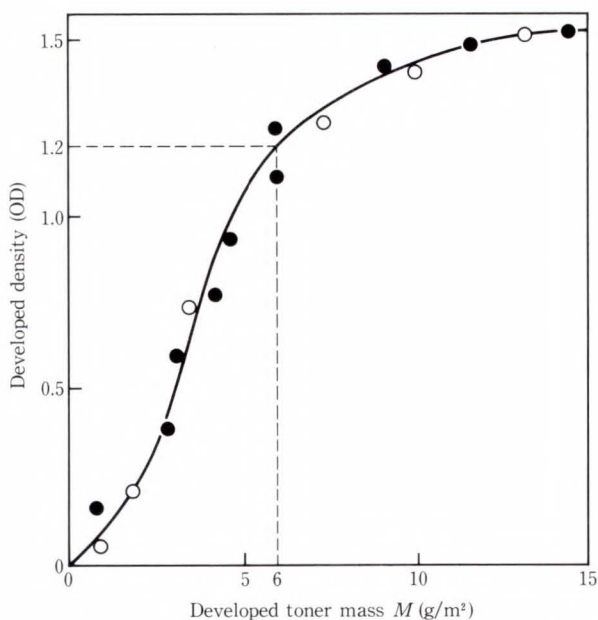


Fig. 6—Developed toner mass vs. developed density.

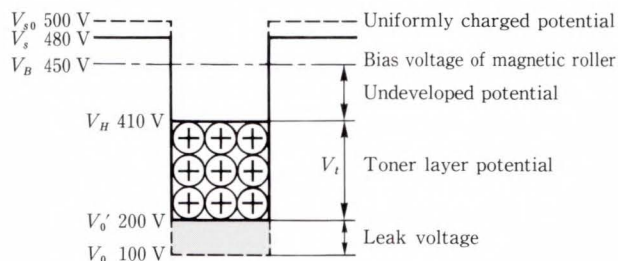


Fig. 7—Potential model of developed image.

Nitrogen gas blows the toner off a part of the developed recording layer. We measured the surface potential V_0 of the latent image area. The toner layer potential voltage is given by $V_t = V_H - V_0$.

5) Measurement of mass of stuck toner M

We measured the weight of the Mylar film with a chemical balance before and after development. The developed density can be measured with an optical reflection densitometer. The toner charge to mass ratio can be measured from the toner blown off after development¹⁶⁾.

4. Results and discussion

4.1 Static analysis^{12), 13)}

This section clarifies the required developed toner mass and a potential model, discusses

the relationship between the developed toner mass and the primary development parameters, comparing the values from Equation (5) and measurements.

This section discusses the measurement of the required developed toner mass, the potential model, and explains the use of theoretical Equation (5) and the experiments to clarify the relationship between the developed toner mass and the primary development parameters.

4.1.1 Relationship between mass of ahead toner and developed density

Figure 6 shows the relationship between the developed toner mass and the developed density. We found no significant difference between the two types of toner we used. When the required developed density is 1.2, the necessary developed toner mass is 6 g/m^2 (see Fig. 4). We use 6 g/m^2 as the standard for evaluation.

4.1.2 Potential model of developed image

The potential model is of a developed image (see Fig. 7) by developing a latent image until saturation. The Mylar film is uniformly charged to +500 V, then a negative potential is applied to the non-contacting pin electrodes to form a latent image. The latent image potential V_{l0} is +100 V and the latent image intensity ($V_{s0} - V_{l0}$) is +400 V. The latent image is developed by a magnetic roller bias voltage of +450 V to saturation, then the toner fills the latent image to +410 V. The toner does not fill the latent image to the bias voltage because of the electrostatic force between the toner and carrier.

This undeveloped potential is about 40 V. After development, uniformly charged potential V_{s0} decreases by 20 V and the bottom of the latent image potential V_{l0} increases by 100 V. This is caused by leakage current between the magnetic brush and the latent image. As a result, the latent image intensity decreases. The leak current greatly depends on the contact between the magnetic brush and recording layer, and can be decreased by reducing the contact. Finally, the toner layer potential V_t is 210 V, which is 60 percent

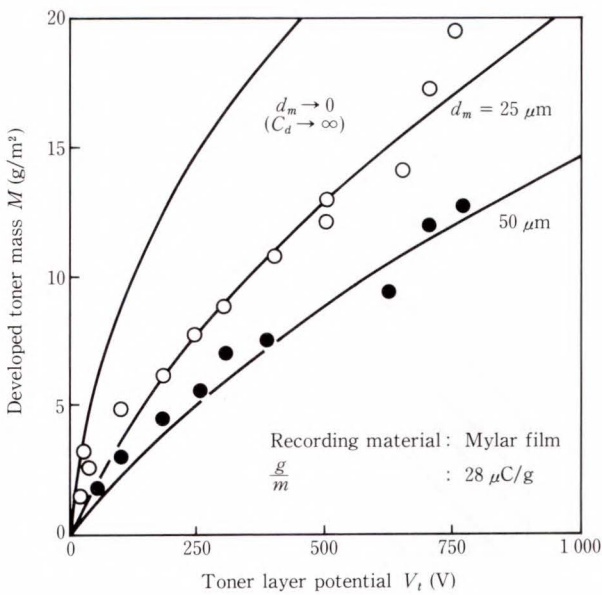


Fig. 8—Relationship between toner layer potential and developed toner mass.

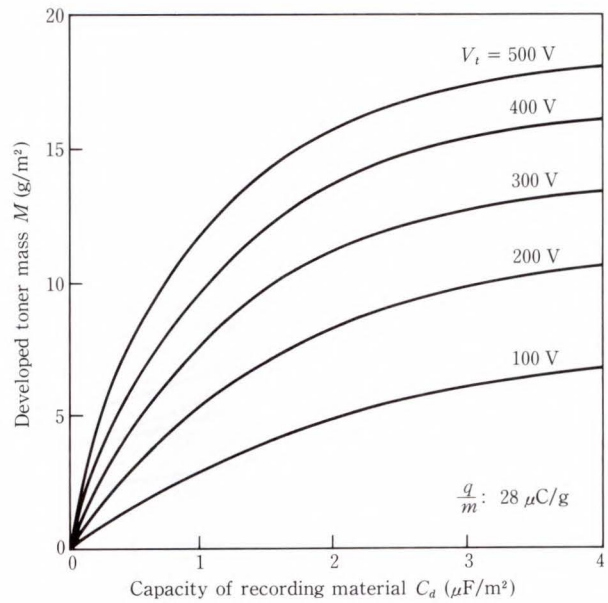


Fig. 9—Relationship between capacity of recording material and developed toner mass.

of the effective latent image intensity ($V_B - V_0$). The toner does not reach the developing bias potential, because of the electrostatic attraction between the toner and carrier. As developing proceeds, the latent image is filled with the toner. As a result, the electrostatic force of the latent image weakens until it equals the electrostatic attraction between the toner and carrier. Development then stops.

4.1.3 Relationship between toner layer potential and developed toner mass

To determine the relationship between the developed toner mass and the toner layer potential using Equation (5), the parameters were measured or estimated as follows:

- δ : toner density $1.1 \times 10^3 \text{ kg/m}^3$
- p : packing density of toner layer 0.6
- ϵ_{rl} : relative dielectric constant of toner layer 2.2
- ϵ_m : relative dielectric constant of recording layer 3.2
- d_m : thickness of recording layer 25 μm or 50 μm
- ϵ_0 : dielectric constant of vacuum $8.85 \times 10^{-12} \text{ F/m}$
- $\frac{q}{m}$: toner charge to mass ratio 28 $\mu\text{C/g}$.

By substituting these values into Equa-

tion (5), the theoretical value of the developed toner mass can be calculated. Figure 8 shows relationship between the developed toner mass M and the toner layer potential V_t . Calculated and measured capacities of recording layer ($0.57 \mu\text{F/m}^2$ and $1.13 \mu\text{F/m}^2$) are shown. The good agreement between the calculations and the measurements shows the validity of our analysis. To obtain the required developed toner mass of 6 g/m^2 , the toner voltage must be +170 V when the Mylar film is 25 μm thick (a capacitance of $1.13 \mu\text{F/m}^2$), and it must be +280 V when the Mylar film is 50 μm thick (a capacitance of $0.57 \mu\text{F/m}^2$).

4.1.4 Relationship between capacity of recording layer and developed toner mass

Development, when viewed as a potential model, is a process in which a potential hole with a charge of $Q = CV$ is filled up with toner particles with charge q . The developed toner mass increases with C and V . Figure 9 shows the relationship between the capacity of the recording layer and the developed toner mass, which is calculated from Equation (5) using the toner layer potential as a parameter. As the capacity of the recording layer increases, the developed toner mass increases, but its

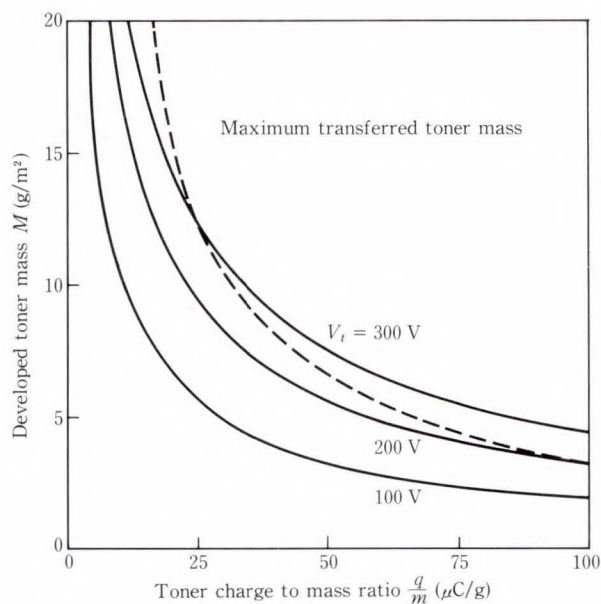


Fig. 10—Relationship between toner charge to mass ratio and developed toner mass.

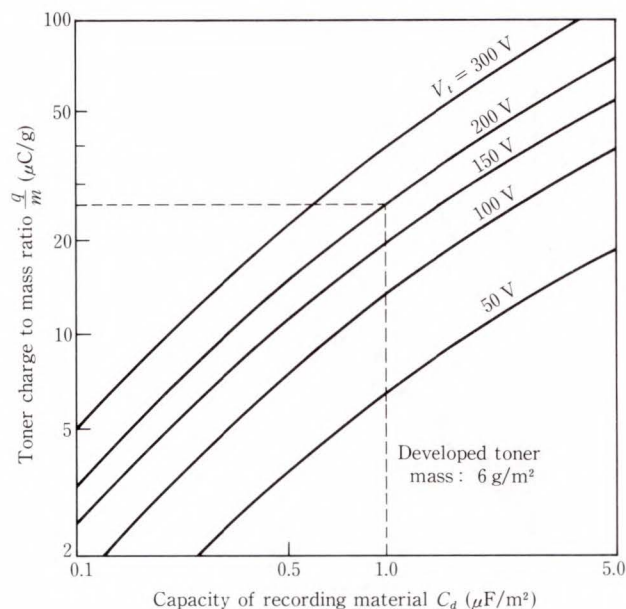


Fig. 11—Requirements of developer and recording material characteristics.

rate gradually saturates. Infinite capacity is illustrated in Fig. 8 above. This diagram can be used for evaluating the capacity of recording materials.

4.1.5 Relationship between toner charge to mass ratio and developed toner mass

Figure 10 shows the relationship between toner charge to mass ratio and developed toner mass calculated from Equation (5). The developed toner mass increases with decreasing toner charge to mass ratio. When the toner charge to mass ratio is too small, the electrostatic force between toner and carrier is weak so toner particles are liable to scatter during the rotation of magnetic brush. However, the minimum charge to mass ratio depends on several factors, such as the speed of magnetic roller and the distribution of toner charge to mass ratios. Thus, the lower limit cannot be determined absolutely. Usually, the lower limit is from 5 μC/g to 10 μC/g.

We will consider the upper limit of developed toner mass for a recording process that includes toner transfer. The amount of toner which can be transferred is limited. We call this limit the maximum transferred toner mass (see Fig. 10). If developed toner

mass exceeds the limit, excessive toner remains on recording layer. There is an optimal transfer charge Q_{opt} which gives the maximum transfer efficiency. It is 320 μC/m² 17). When the charge on the recording paper exceeds this limit, discharge occurs across the air gap between the paper and the recording layer. This not only decreases electric field, but neutralizes the toner charge, thus decreasing the transfer efficiency. Since the maximum toner charge allowing toner transfer is equal to the charge on the paper, the maximum transferred toner mass M_{tmax} is given by:

$$M_{tmax} = \frac{Q_{opt}}{\frac{q}{m}} \dots \dots \dots (19)$$

When the developed toner mass exceeds M_{tmax} , the amount of toner remaining on the recording layer increases.

4.1.6 Requirements for developer and recording layer

Figure 11 shows the toner charge to mass ratio, the capacity of the recording layer and the toner layer potential required for a developed toner mass of 6 g/m². Using this, we can design the developer, recording layer

and latent image formation method. For example, when the capacity of the recording layer is $1 \mu\text{F}/\text{m}^2$ and the toner layer potential is $+200 \text{ V}$, a developer with a toner charge to mass ratio of $28 \mu\text{C}/\text{g}$ or less and more than $5 \mu\text{C}/\text{g}$ to $10 \mu\text{C}/\text{g}$ is required.

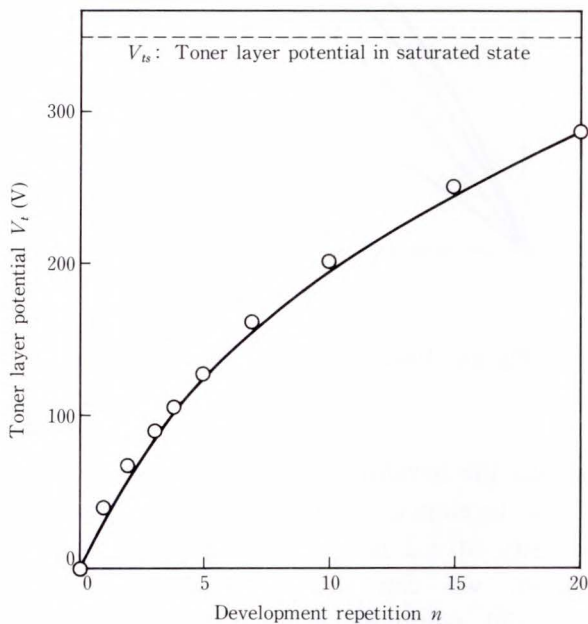


Fig. 12—Relationship between development repetition and toner layer potential.

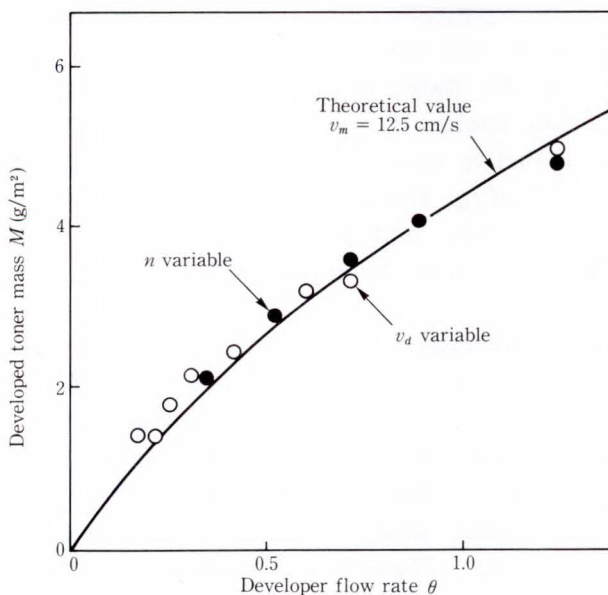


Fig. 13—Relationship between developer flow rate and developed toner mass.

4.2 Results from dynamic analysis^{14), 15)}

This section discusses the measured relationship between the developer flow rate and developed toner mass, and compares values calculated with Equations (12) and (13) and measured values. We then explain the conditions for obtaining the necessary developed density using equations.

4.2.1 Influence of developer flow rate

Figure 12 shows the relationship between the number of development cycles and the toner layer potential, where the magnetic roller speed v_m is $12.5 \text{ cm}/\text{s}$ and the recording drum speed v_d is $70 \text{ cm}/\text{s}$. The proportionality constant γ in Equation (13) is determined from this figure. The measured saturated toner layer potential V_{ts} is 350 V . When this value is substituted in Equation (13), we obtain $\gamma = 0.5$. Figure 13 shows the relationship between the developer flow rate and the developed toner mass. The open circles indicate measurements, where magnetic roller speed v_m is held at $12.5 \text{ cm}/\text{s}$ and the recording speed v_d is varied between $10 \text{ cm}/\text{s}$ and $70 \text{ cm}/\text{s}$. The black dots indicate results given in Fig. 14. The solid line is the theoretical curve obtained when the saturated toner voltage V_{ts} is 350 V and the proportionality constant γ is 0.5 . Even when the number

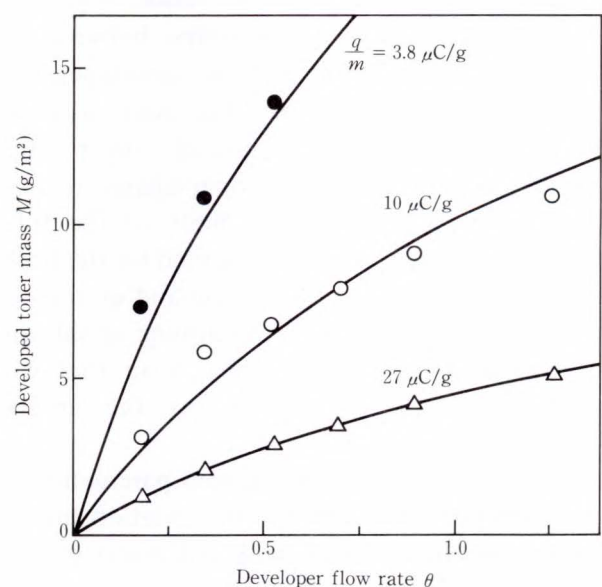


Fig. 14—Developed toner mass vs. developer flow rate.

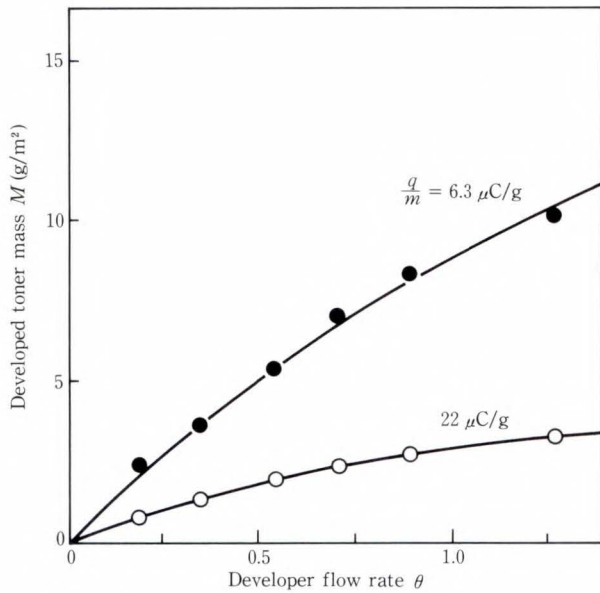


Fig. 15—Developed toner mass vs. developer flow rate (non-conductive carrier).

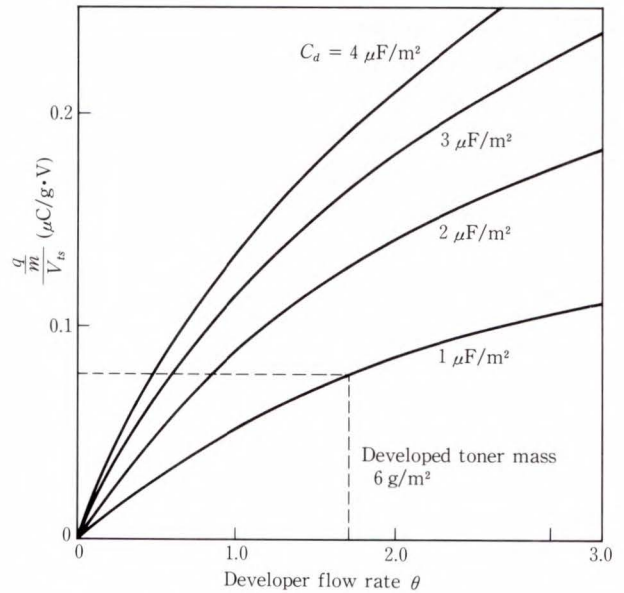


Fig. 16—Development parameter design chart.

of development cycles or the recording drum speed is changed, the developed toner mass is constant if the developer flow rate θ is constant. The good agreement between the calculations and the experiments shows the validity of the analysis.

4.2.2 Toner charge to mass ratio and carrier coating

We examined several developers with different toner charge to mass ratios. Figures 14 and 15 show the relationships between the developed toner mass and the developer flow rate of these developers. The solid lines are theoretical curves. Developed toner mass increases with decreasing toner charge to mass ratio. The practical lower limit of the toner charge to mass ratio is determined by the beginning of toner particle scattering and an increase in background density. Developing speed with a conductive carrier is higher than that with a dielectric coated carrier, as the analysis predicted.

4.2.3 Design of development parameters

Analysis has clarified the relationship between developed toner mass and primary development parameters. Through this analysis, we have determined the necessary development conditions for high developed density. Figure 16

shows the development parameter requirements for a developed density of 6 g/m². A developed density of 1.2 is very dense printing. With this graph, we can design developer, recording material, latent image intensity or development device.

For example, the capacity of a selenium-alloy photoconductive drum is about 1 $\mu\text{F/m}^2$ and toner layer potential in the saturated state is expected to be about +250 V. From Fig. 16, we can see that magnetic roller speed must be more than 1.7 times the recording drum speed, if we use a developer with a conductive carrier with a charge to mass ratio of 20 $\mu\text{C/g}$. The same applies to a non-conductive carrier, and roller speed must be more than two times the drum speed.

5. Conclusion

We introduced a potential model for the development process and equations of developed toner mass for two-component magnetic brush reversal development. We used both dynamic and static analysis, resulting in consistent equations. These studies agreed well with measurements. Using these results, we clarified the relationship between developed toner mass and development parameters, such as the

capacity of the recording layer, the toner charge to mass ratio, the toner layer potential, and the developer flow rate. Our theory is a practical guideline for designing development and equipment.

In the future, we plan to determine the relationship between development conditions and other image quality parameters, such as sharpness.

References

- 1) Schaffert, R.M.: Electrophotography. 2nd. ed., New York, Focal Press, 1975, 989p.
- 2) Kutsuwada, N., and Ando, Y.: A Consideration of Forces Acting on Toner in Electrophotographic Powder Development. *Jpn. Soc. Appl. Phys.*, **39**, 5, pp. 406-412 (1977).
- 3) Kutsuwada, N., and Ando, Y.: Imaging process in electrophotography. *Image Technol.*, **11**, p. 65 (1971).
- 4) Kondo, A., and Kamiya, M.: Mechanism of Powder Development and Methods of Measuring Toner Parameters. (in Japanese), *Tech. Rep. IECE, Jpn.*, **75**, 112, IE-75-65, pp. 33-42 (1975).
- 5) Schein, L.B.: Electric Field Enhancement in the Magnetic Brush Developer. *Phot. Sci. Eng.*, **19**, 1, pp. 3-5 (1975).
- 6) Schein, L.B.: Microscopic Theory of Magnetic Brush Development. *Phot. Sci. Eng.*, **19**, 5, pp. 255-265 (1975).
- 7) Harpavat, G.: Electrostatic Field Stripping Model of Magnetic Brush Development. IEEE IAS'75 Annual Meet., (1975), pp. 128-134.
- 8) Verliden, W., Van Engeland, J., and Van Biesen, J.: Granularity of Electrophotographic Images. *J. Photogr. Sci. (GB)*, **25**, 4, pp. 154-158 (1977).
- 9) Hays, D.A.: Neutrization of electrophotographic developer. *J. A. Phys.*, **48**, 11, pp. 4430-4434 (1977).
- 10) Hays, D.A.: Electric Field Detachment of Toner. *Photo. Sci. Eng.*, **22**, 4, pp. 232-235 (1978).
- 11) Williams, E.M.: An Electrostatic Model for Toner Deposition onto a Photoconductor. IEEE IAS Annual Meet., 1978, pp. 215-221.
- 12) Nakajima, J., Kimura, M., Horie, M., and Matsuda, T.: An Analysis of Magnetic Brush Reversal Development. (in Japanese), *Trans. IECE, Jpn.*, **J61-C**, 7, pp. 416-423 (1978).
- 13) Nakajima, J., Kimura, M., and Takahashi, H.: An Analysis of Magnetic Brush Reversal Development. *FUJITSU Sci. Tech. J.*, **15**, 3, pp. 115-125 (1979).
- 14) Nakajima, J., Kimura, M., Horie, M., and Matsuda, T.: Dynamic Analysis of Magnetic Brush Development. (in Japanese), *Trans. IECE, Jpn.*, **J61-C**, 9, pp. 601-606 (1978).
- 15) Nakajima, J., Matsuda, T., Horie, M., and Takahashi, H.: Dyanamic Analysis of Magnetic Brush Development. IEEE IAS Annual Meet., 1978, pp. 225-229.
- 16) Nakajima, J., Aikawa, H., Horie, M., and Takahashi, H.: A New Measuring Method of Toner Charge. (in Japanese), *Trans. IECE, Jpn.*, **J59-C**, 3, pp. 175-177 (1976).
- 17) Takahashi, H., Kimura, M., Nakajima, J., and Horie, M.: Studies on Corona Discharge Transfer of Toner Image. *Trans. IECE, Jpn.*, **J60-C**, 3, pp. 148-153 (1977).



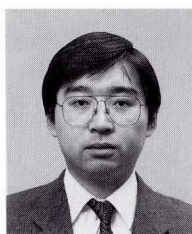
Masatoshi Kimura

Printer Technology Laboratory
FUJITSU LABORATORIES, ATSUGI
Bachelor of Electron Eng.
Okayama University 1973
Dr. of Electron Eng.
Osaka University 1986
Specializing in Electrophotographic
Process and Electrostatic Recording



Junzo Nakajima

R & D Coordination Office
FUJITSU LABORATORIES, ATSUGI
Bachelor of Electrical Eng.
Musashi Institute of Technology 1966
Dr. of Electronic Eng.
Tokyo Insitute of Technology 1982
Specializing in Electrophotography and
Electrostatic Recording



Makoto Kato

Printer Technology Laboratory
FUJITSU LABORATORIES, ATSUGI
Bachelor of Mechanical Eng.
Science University of Tokyo 1983
Specializing in Electrophotographic
Process and Mechanical Design

The Electrostatic Transfer of Toner Images

• Masatoshi Kimura • Masahiro Wanou • Hiroshi Nou

(Manuscript received September 6, 1989)

Electrostatic toner image transfer has been studied theoretically and experimentally. Three transfer methods have been investigated: corona transfer, conductive roller transfer, and dielectric roller transfer.

It has been shown theoretically and experimentally that the dependence of the transfer ratio on the electric field between transfer material and toner layer is the same for all three methods. The optimum toner charge to mass ratio gives a maximum transfer ratio. Theory suggests that the maximum transfer speed is 6.7 m/s for corona transfer and 125 m/s for roller transfer.

Toner images are transferred to plain paper with a transfer ratio above 80 percent at a paper speeds up to 2 m/s.

1. Introduction

Toner is transferred in one of two ways: mechanically, using the mechanical adhesion of the toner to the paper, and electrostatically, using the charge of the toner. Electrostatic transfer is widely used because it is simple and reliable. Electrostatic transfer involves pressing paper against the toner image and generating an electric field which helps move the charged toner onto the paper. Electrostatic transfer is further divided into two methods.

They are corona transfer, which uses corona ions to generate the electric field, and bias roller transfer, which uses an elastic rubber roller which is pressed against the paper and to which a voltage is applied to generate the electric field.

Although there are several techniques¹⁾⁻⁴⁾, systematic studies of the physics of electrostatic transfer are lacking, particularly concerning the toner charge/mass ratio and transfer speed.

This report examines the primary factors affecting the transfer ratio and the optimum conditions for toner transfer.

The transfer speed is investigated here,

together with the transfer mechanism, optimum transfer conditions, optimum toner charge/mass ratio and theoretical limits of transfer speed. The mechanism, optimum conditions and toner charge/mass ratio are the same for both transfer techniques. The transfer ratio is determined solely by the electric field in the air gap in the transfer region, and reaches a peak at 36 MV/m. There is an optimum toner charge/mass ratio which gives a maximum transfer ratio. The theoretical limit of the transfer speed is 125 m/s for roller transfer, and 6.7 m/s for corona transfer.

2. Conditions for transfer and transfer ratio⁵⁾⁻⁸⁾

2.1 Principle of electrostatic transfer

Figure 1 is a simplified model of electrostatic transfer. Transfer material is placed against the developed toner image on the photoconductive layer and a charge opposite to the toner charge is applied to the transfer material. When the electrostatic force attracting the toner toward the transfer material is stronger than that to the photoconductive layer, the toner is transferred to the transfer material.

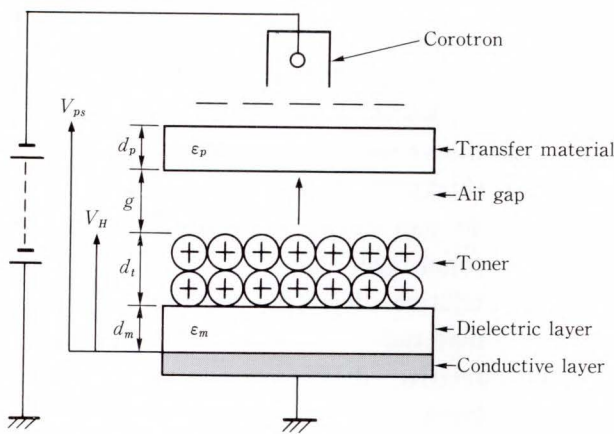


Fig. 1—Electrostatic toner image transfer.

A charged toner layer with thickness d_t and volume charge density ρ is on a photoconductive surface with thickness d_m in Fig. 1. Transfer material with thickness d_p comes into contact with the charged toner. Let g be the gap between the toner and the transfer material. When the transfer material has a charge opposite to the toner, σ_c , the electric force $F_e(x)$, which acts on the charged toner q_t in the direction of the transfer material at distance x from the photoconductive surface is given by

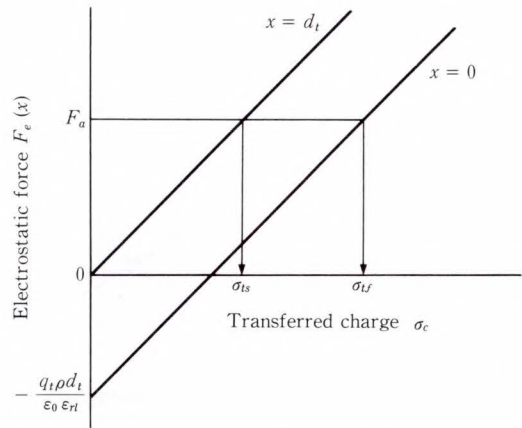
$$F_e(x) = q_t \frac{-\sigma_c - \rho(d_t - x)}{\epsilon_0 \epsilon_{rl}}, \quad \dots (1)$$

where ϵ_{rl} is the relative dielectric constant of the toner layer.

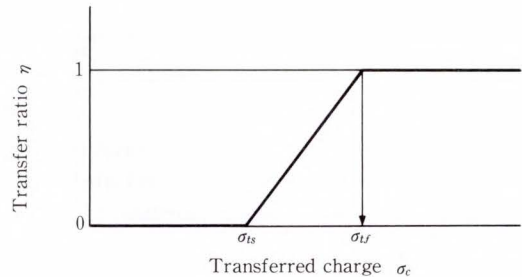
Assuming that $F_e(x)$ acting on the charged toner at distance x from the photoconductive surface is balanced with mechanical adhesion F_a and that only the toner with thickness $(d_t - x)$ is transferred to the paper, the transfer ratio η is given by

$$\eta = \frac{d_t - x}{d_t} = \begin{cases} 0 & \sigma_{ts} < \sigma_c \\ -\frac{1}{\rho d_t} \left(\sigma_c + \frac{\epsilon_0 \epsilon_{rl}}{q_t} F_a \right) & \sigma_{tf} < \sigma_c \leq \sigma_{ts} \\ 1 & \sigma_c \leq \sigma_{tf}. \end{cases} \dots (2)$$

Figure 2 graphs Equations (1) and (2) with σ_c as the variable. $F_e(d_t)$ on the toner surface



a) Electrostatic force



b) Transfer ratio

Fig. 2—Influence of transfer charges.

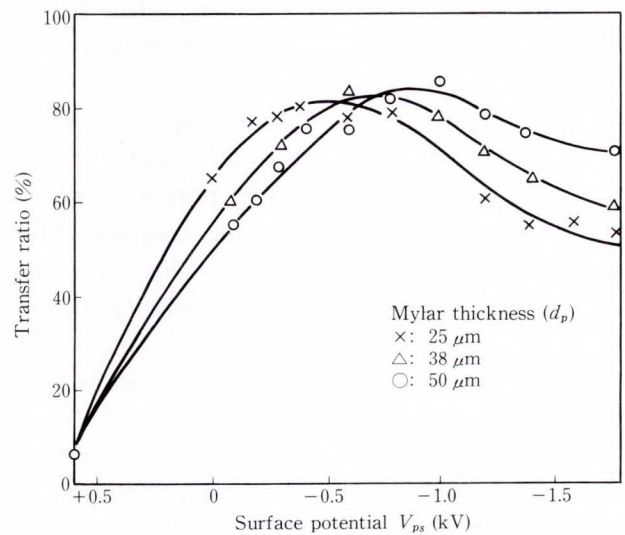


Fig. 3—Relationship between transfer ratio and surface potential for transfer materials with different thicknesses (corona transfer).

($x = d_t$) increases linearly with the transfer charge. The toner layer on the photoconductive surface receives $F_e(0) = -q_t \rho d_t / \epsilon_0 \epsilon_{rl}$ in the

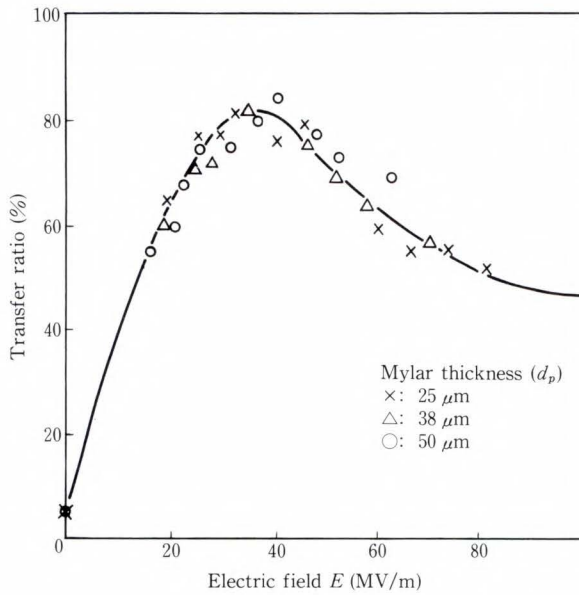


Fig. 4—Relationship between transfer ratio and electric field in the air gap between the transfer material and toner layer (corona transfer).

opposite direction because of the charge on the toner. When σ_c and the F_e cancel each other out, an upward force is generated. Thus, transfer begins where $F_e(d_t)$ exceeds F_a . The transfer ratio thus increases linearly. It becomes 100 percent when $F_e(0)$ acting on the toner on the surface of the photoconductive layer exceeds F_a .

Figure 3 shows the relationship between transfer ratio and surface potential of the transfer material for corona transfer. Three kinds of thickness of Mylar film were used as transfer material. Its high resistivity prevents the surface charge from leaking. The surface potential at which the transfer ratio is at its maximum decreases as the thickness of the film decreases in Fig. 3. Figure 3 is replotted in Fig. 4 to clearly show the relationship between the transfer ratio and the electric field in the air gap.

The electric field is calculated by the following equation:

$$E = \frac{V_H - V_{ps}}{\frac{d_p}{\epsilon_p} + \frac{d_t}{\epsilon_{rl}} + \frac{d_m}{\epsilon_m} + g} \quad \dots \dots \dots (3)$$

where

V_H : surface potential of developed toner

image

V_{ps} : surface potential of transfer material

d_p : thickness of transfer material

d_t : thickness of toner layer

d_m : thickness of photoconductive layer

g : air gap between transfer material and toner layer

ϵ_p : relative dielectric constant of transfer material

ϵ_{rl} : relative dielectric constant of toner layer.

ϵ_m : relative dielectric constant of photoconductive layer.

The parameters were measured and calculated as follows:

V_H : +600 V

d_p : 25 μm , 38 μm , 50 μm

d_t : 12 μm

d_m : 25 μm

g : 1 μm (assumed)

ϵ_p : 3.2

ϵ_{rl} : 2.2

ϵ_m : 3.2.

Figure 4 shows the relationship between the electric field across the gap $E_g (= \sigma_c / \epsilon_0)$ and transfer ratio. Only one curve is given for the three thicknesses of Mylar. As suggested by Equation (2), the most important factor influencing transfer is the electric field across the gap, which is the transferred charge. Transfer ratio assumes that when a peak for a given transfer electric field across the gap exceeds a certain level, breakdown occurs^{2),3)}, reducing the electric field. Transfer ratio reaches its maximum just before this reduction occurs. This discharge is confirmed by observing the light emitted on the toner layer formed on a transparent base using a photomultiplier⁹⁾. The electric field across the gap immediately before the discharge gives the maximum transfer ratio, and is 36 MV/m, which corresponds to a surface charge density of 320 $\mu\text{C}/\text{m}^2$. This value gives the optimum amount of transfer charge Q_0 .

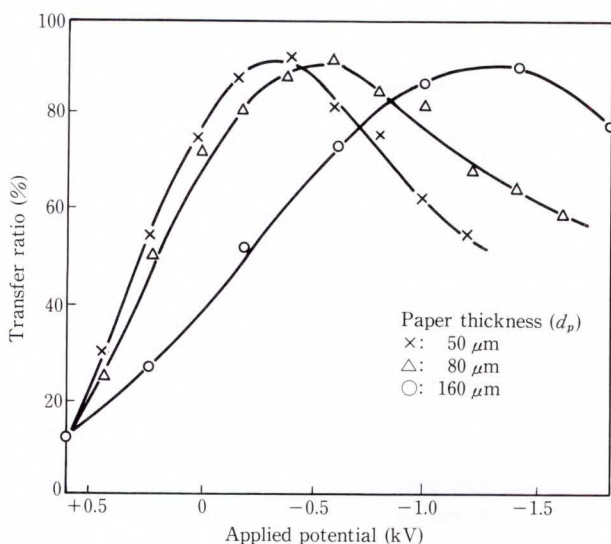


Fig. 5—Relationship between transfer ratio and potential applied to transfer materials with different thicknesses (conductive roller transfer).

Figure 5 shows the relationship between the transfer ratio and the voltage applied to the roller for conductive roller transfer. This relationship was found to be almost the same as that for corona transfer. Figure 6 shows the relationship between the transfer ratio and electric field in the air gap for conductive and dielectric roller transfer and corona transfer. The dielectric roller was constructed by attaching seamless, 25 μm -thick Mylar film to a conductive rubber roller. Plain paper was used as the transfer material.

The curves for conductive roller transfer and dielectric roller transfer are almost identical (see Fig. 6). The transfer ratios for corona transfer are consistently lower than those for roller transfer due to charge leakage through the transfer material. However, if the transfer material had sufficient resistivity, all three curves would be the same.

The theoretical curve in Fig. 6 is calculated from Equation (2) using the volume charge density of toner layer, $\rho = 21 \text{ C/m}^3$, and the thickness of toner layer, $d_t = 12 \mu\text{m}$. According to the equation, the transfer ratio should be 100 percent if the electric field is greater than 28.5 MV/m.

However, the obtained maximum transfer

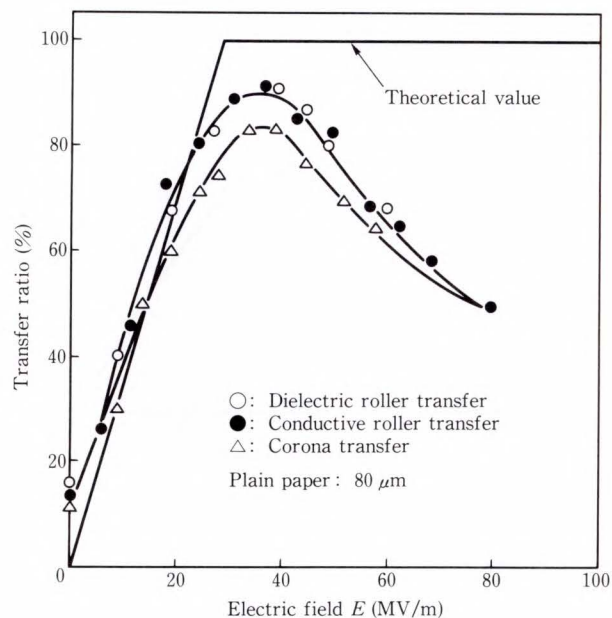


Fig. 6—Relationship between transfer ratio and electric field in the air gap between the transfer material and toner.

ratio was 90 percent, mainly because of the following factors:

- 1) The bottom of the toner layer adheres to the photoconductive drum due to Van der Waals forces.
- 2) Partial discharge between transfer material and photoconductive drum occurs when the transfer material separates from the drum.

2.2 Charge/mass ratio and transfer characteristics of toner

The factors influencing toner transfer include paper thickness, surface resistance, charged-toner resistance, the charge/mass ratio of the toner, and the diameter of the toner particles. The following discussion focuses on the charge/mass ratio of the toner particles which greatly influences F_e .

Volume charge density ρ of the toner layer is given by the following equation using charge/mass ratio T_p of the toner,

$$\rho = \delta p T_p, \quad \dots \dots \dots (4)$$

where δ is the toner density and p is the packing density.

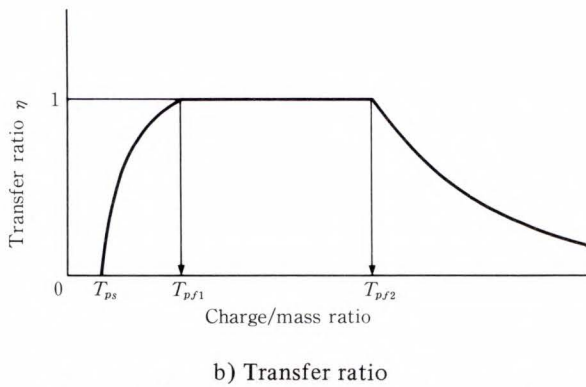
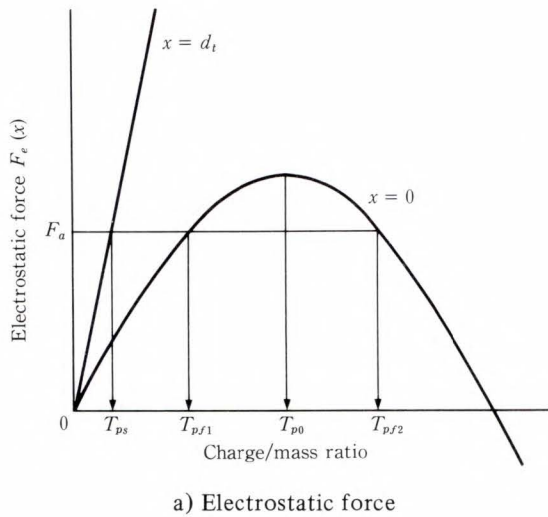


Fig. 7—Influence of toner charge to mass ratio.

When Equation (4) is substituted into Equations (1) and (2), $F_e(x)$ of the charged toner is given as a function of T_p and transfer ratio η ,

$$F_e(x) = \frac{-Q_0 m T_p - \delta p m (d_t - x) T_p^2}{\epsilon_0 \epsilon_{rl}}, \quad \dots (5)$$

$$\eta = \begin{cases} 0 & T_p < T_{ps} \\ \frac{1}{d_t} \left(-\frac{Q_0}{\delta p T_p} - \frac{\epsilon_0 \epsilon_{rl}}{\delta p T_p^2} \frac{F_a}{m} \right) & T_{ps} \leq T_p < T_{pf1} \\ 1 & T_{pf2} < T_p \\ 1 & T_{pf1} < T_p \leq T_{pf2}, \end{cases}$$

where m is the mass of one toner particle.

Let T_{ps} be the charge/mass ratio of the toner when transfer begins, that is, when $F_e(d_t)$ exceeds F_a . Let T_{pf1} be the charge/mass ratio

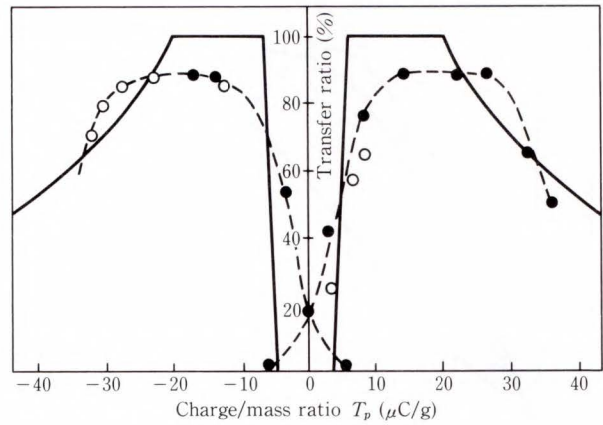


Fig. 8—Relationship between transfer ratio and toner charge to mass ratio.

of the toner when transfer ratio reaches 100 percent and T_{pf2} be the charge/mass ratio when transfer ratio begins to drop below 100 percent {when $F_e(0)$ equals F_a }. Let T_{po} be the charge/mass ratio where the electrostatic force is at its maximum on the photoconductive surface ($x = 0$) (see Fig. 7).

As is clear from Equation (5), F_e at the toner surface ($x = d_t$) increases linearly with the charge/mass ratio. F_e at the photoconductive surface in relation to T_p is a convex parabola. When T_p increases, transfer begins when $F_e(d_t)$ acting on the toner surface exceeds F_a . The transfer ratio then gradually increases. When $F_e(0)$ exceeds F_a , the transfer ratio reaches 100

percent. When the charge/mass ratio increases further, $F_e(0)$ increases until T_{po} is reached, then decreases below F_a . When T_p exceeds T_{pf2} , the transfer ratio decreases.

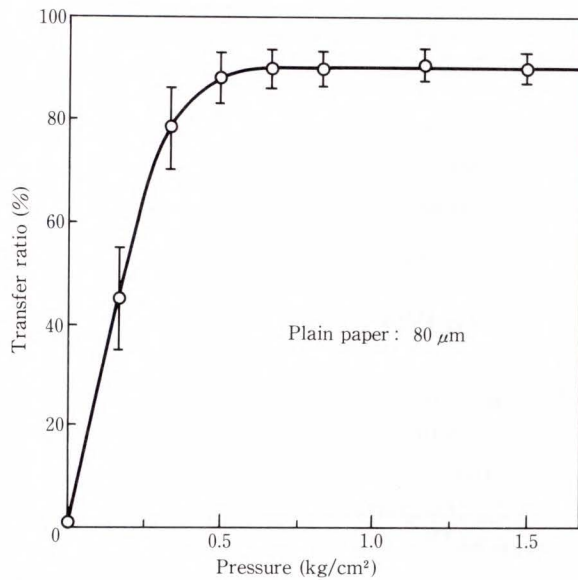


Fig. 9—Relationship between transfer ratio and pressure on the roller (conductive roller transfer).

Figure 8 shows the measured relationship between T_p and transfer ratio η^{10} . Corona charger recharges the toner to vary T_p . A black dot indicates that the toner is positively charged before recharging, and white dot indicates that the toner is negatively charged. Note the optimal charge/mass ratio. The toner had a toner density $\delta = 1110 \text{ kg/m}^3$, $p = 0.6$, $d_t = 20 \text{ }\mu\text{m}$, and $Q_0 = 320 \text{ }\mu\text{C/m}^2$. Values obtained by substituting these parameters into Equation (5) are plotted as a solid line. The theoretical and measured curves agree, suggesting that the theory is reasonable. For toner powder, a developed toner layer thickness $d_t = 20 \text{ }\mu\text{m}$ to $30 \text{ }\mu\text{m}$ is obtained from Equation (5) and the relationship between the optimal charge/mass ratio of the toner and the toner layer thickness. The optimal charge/mass ratio of the toner is about $10 \text{ }\mu\text{C/g}$. For a liquid toner, the optimal charge/mass ratio is ten times greater than that for toner powder because the toner particles are smaller and the developed toner layer is thinner.

2.3 Influence of mechanical contact and paper thickness

2.3.1 Mechanical contact

Figure 9 shows the relationship between

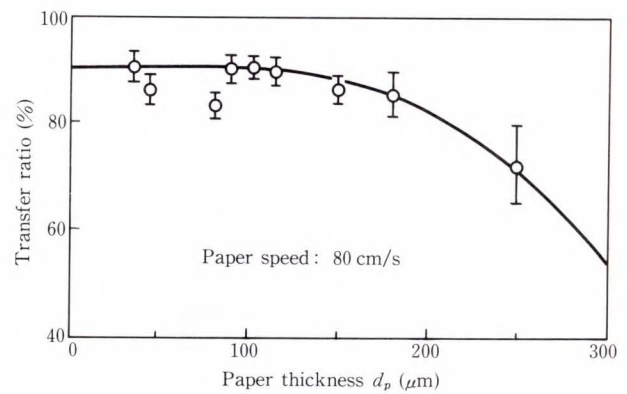


Fig. 10—Relationship between transfer ratio and paper thickness (corona transfer).

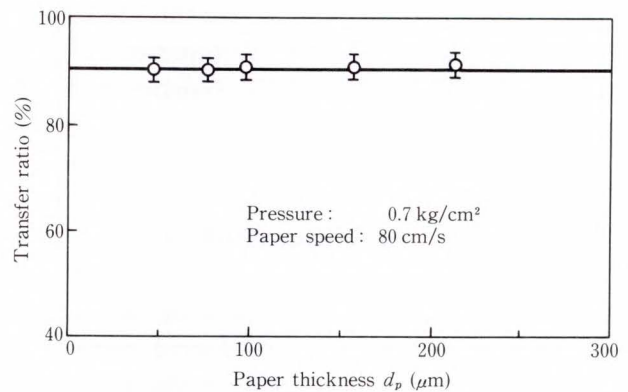


Fig. 11—Relationship between transfer ratio and paper thickness (conductive roller transfer).

transfer ratio and the pressure applied to the conductive roller. The voltage which produces the optimum electric field was applied to the roller, and the standard deviation of the transfer ratio was calculated from the measurements. The error bars in Fig. 9 represent a standard deviation of 1.5 (90 percent). High transfer ratio and low variation are achieved by pressures above 0.7 kg/cm^2 . Pressure is necessary for good image transfer. Pressure ensures that the transfer material is in good contact with the recording drum.

2.3.2 Paper thickness

Figure 10 shows the relationship between the transfer ratio and the thickness of the paper used as transfer material under optimum conditions using corona transfer. A pressure roller in front of the transfer corotron dampens vibra-

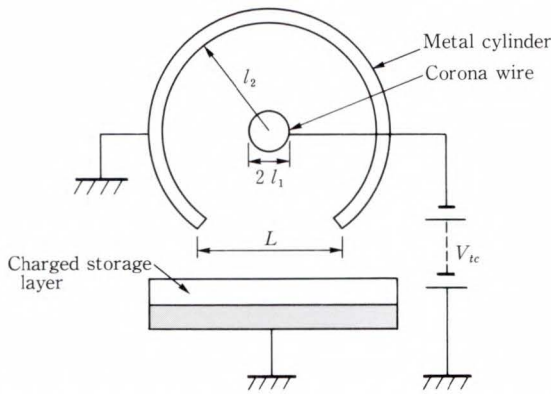


Fig. 12—Cylindrical corona charging unit (corotron).

tions. The transfer ratio is independent of paper thickness below 120 μm. Above this the transfer ratio decreases because of imperfect contact between paper and drum. The transfer ratio with 80 μm paper is lower because the resistivity of the 80 μm paper is one tenth that of the other paper.

Figure 11 shows the results for the roller transfer technique. The transfer ratio is independent of paper thickness up to 220 μm, and toner images are transferred onto plain paper with a transfer ratio of 90 percent and variation of ±2 percent.

3. Transfer speed^{7),11)}

Transfer time includes both the charging time to obtain the optimum electric field and toner migration time from the image formation surface to the paper. Each of these factors was investigated theoretically to estimate the limit of the speed of corona transfer and roller transfer for comparison with measurements.

3.1 Theoretical analysis

3.1.1 Charging time

1) Corona transfer

Consider the corona discharge unit (corotron) shown in Fig. 12, with concentric cylindrical electrodes of radii l_1 and l_2 . The corona discharge start voltage V_0 is given by the following equation¹²⁾. (All calculations use SI units.)

$$V_0 = 3.1l_1 \ln\left(\frac{l_2}{l_1}\right) \left(1 + \frac{0.0308}{\sqrt{l_1}}\right) \times 10^6. \quad (6)$$

When corotron voltage V_{tc} is applied to the corona wire, the total corona current per unit length¹³⁾ is given by

$$i_c = \frac{8\pi\epsilon_0\mu}{(l_2)^2 \ln\left(\frac{l_2}{l_1}\right)} V_{tc}(V_{tc} - V_0), \quad \dots (7)$$

where μ is the ion mobility ($2 \times 10^{-4} \text{ m}^2/\text{Vs}$).

In a cylindrical corona discharge unit with one section of the outer electrode removed (see Fig. 12), the charge Q in the charge storage layer is given by¹³⁾

$$Q(t) = CV_{tc} \frac{1 - \exp\left(\frac{A_s V_0}{C} t\right)}{1 - \frac{V_{tc}}{V_{tc} - V_0} \exp\left(\frac{A_s V_0}{C} t\right)}, \quad \dots (8)$$

where C is the capacitance of the charge storage layer, t is the charging time and

$$A_s = \frac{4\epsilon_0\mu}{(l_2)^3 \ln\left(\frac{l_2}{l_1}\right)}$$

Using Equation (8), the charging time τ_c required to store the charge necessary for image transfer ($Q_0 = 320 \mu\text{C}/\text{m}^2$) is given by

$$\tau_c = \frac{C}{A_s V_0} \ln \frac{(V_{tc} - V_0)(CV_{tc} - Q_0)}{V_{tc} \{C(V_{tc} - V_0) - Q_0\}} \quad (9)$$

2) Roller transfer

There are two methods of roller transfer, conductive and dielectric. If the capacitance of the dielectric roller is included in the total capacitance of the photoconductive layer, the two methods of roller transfer can be analyzed with the same model. Therefore, only conductive roller transfer is considered here.

The charge storage layer is charged through the resistance R of the conductive roller. Since $t = 0$ and V_{tR} is a step function, the amount of charge stored in capacitance C is obtained

by

$$Q(t) = CV_{tR} \left\{ 1 - \exp\left(-\frac{t}{CR}\right) \right\}. \quad \dots (10)$$

Defining charge time τ_R as the time required to reach 90 percent of the required charge starting from 10 percent, the charge time τ_R can be expressed as

$$\tau_R = 2.2CR. \quad \dots (11)$$

3.1.2 Toner migration time

Assuming that the optimum amount of charge Q_0 is stored in the transfer paper, the electric field $E(z)$ in the toner layer (see Fig. 1) which is at distance z from the recording layer is given by

$$E(z) = \frac{Q_0}{\epsilon_0} - \frac{\rho}{\epsilon_0} (d_t - z). \quad \dots (12)$$

The toner traverses the air gap with the acceleration produced by the electric field and arrives at the transfer paper. The time necessary for this is

$$t = \sqrt{\frac{2gm}{q} \frac{1}{\frac{Q_0}{\epsilon_0} - \frac{\rho}{\epsilon_0} (d_t - z)}}. \quad (13)$$

Equation (13) describes the motion of the toner at point z . Therefore, the thickness W_t of the toner layer that is transferred in time t is

$$W_t = d_t - z. \quad \dots (14)$$

Combining Equations (13) and (14) gives

$$W_t = \frac{\epsilon_0}{\rho} \left(\frac{Q_0}{\epsilon_0} - \frac{2gm}{qt^2} \right). \quad \dots (15)$$

The final toner layer thickness W_∞ (W_t at $t = \infty$ in Equation (15)) is given by

$$W_\infty = \frac{Q_0}{\rho}. \quad \dots (16)$$

If the toner migration time τ_t is defined as 90 percent of W_∞ , the toner transfer time becomes

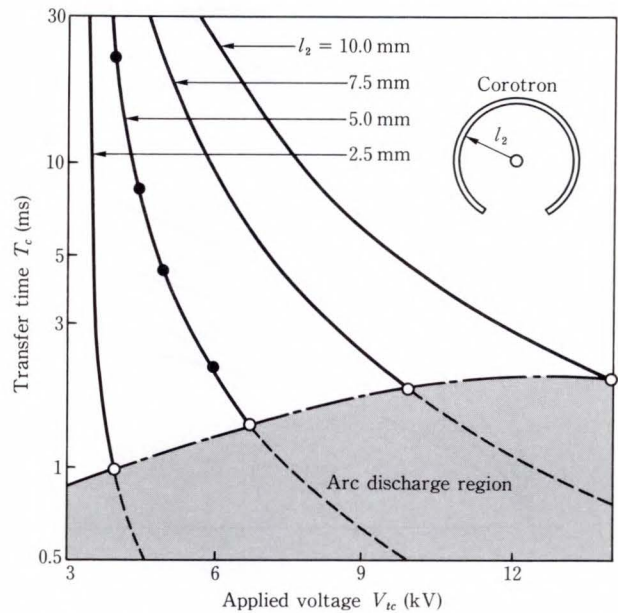


Fig. 13—Relationship between transfer time and voltage applied to the corona wire. The solid line shows theoretical values, and dots are experimental data. The gray area shows the arc discharge region.

$$\tau_t = \sqrt{\frac{20gm}{q} \frac{\epsilon_0}{Q_0}}. \quad \dots (17)$$

In one of the setups, the following values were obtained: $C = 0.4 \mu\text{F}/\text{m}^2$ (capacitance of $25 \mu\text{m}$ Mylar film, $12 \mu\text{m}$ toner layer and $80 \mu\text{m}$ line printer paper), $V_{tc} = 6 \text{ kV}$, $l_1 = 30 \mu\text{m}$, $l_2 = 5.0 \text{ mm}$, $R = 0.38 \Omega\text{m}^2$ (the measured value of the conductive roller), $Q_0 = 320 \mu\text{C}/\text{m}^2$, $g = 1 \mu\text{m}$, $q/m = 30 \mu\text{C}/\text{g}$. Therefore, the charging times and toner transfer time are $\tau_c = 2 \text{ ms}$, $\tau_R = 0.33 \mu\text{s}$ and $\tau_t = 4.4 \mu\text{s}$. Since $\tau_t \ll \tau_c$, the corona transfer time T_c is essentially τ_c . Also, since $\tau_R \ll \tau_t$, the roller transfer time T_R is essentially τ_t . Therefore, T_c and T_R can be expressed as

$$\begin{aligned} T_c &= \tau_c + \tau_t \approx \tau_c, \\ T_R &= \tau_R + \tau_t \approx \tau_t. \end{aligned} \quad \dots (18)$$

3.2 Results and discussion

3.2.1 Transfer time

Figure 13 shows the relationship between T_c and V_{tc} for various corotron geometries.

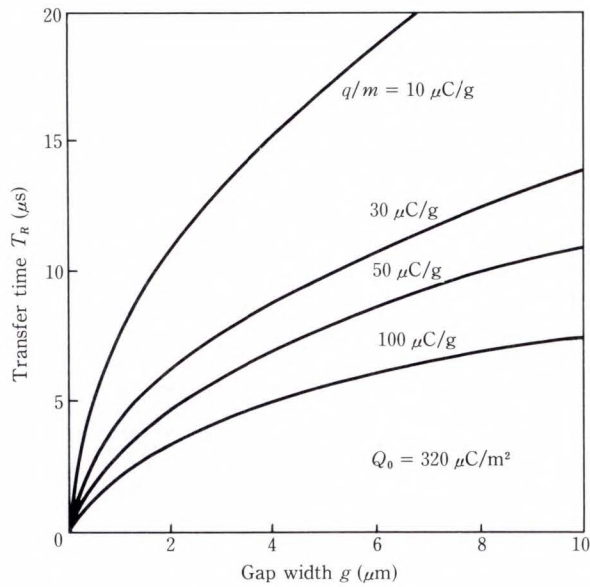


Fig. 14—Relationship between transfer time of roller transfer and width of gap between transfer material and toner layer. The term q/m is toner charge to mass ratio. Q_0 is the charge applied to the transfer material.

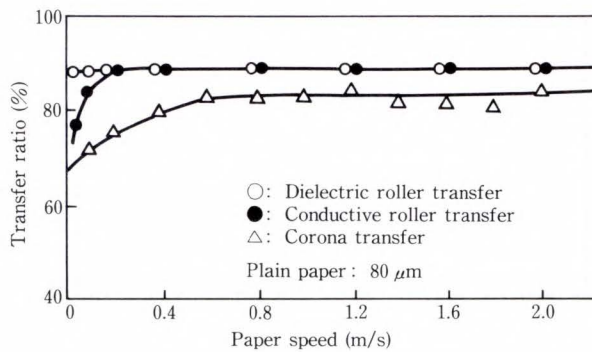


Fig. 15—Relationship between transfer ratio and paper speed.

The curves were calculated from Equation (9) with a composite capacitance of $0.4 \mu\text{F/m}^2$. The maximum applied voltage before arc discharge was measured for various corotrons. These values are indicated in Fig. 13 by circles. Thus, the corotron cannot be used in the shaded region of Fig. 13.

The smaller the corotron, the higher the corona discharge ratio and the shorter the transfer time. A short transfer time prevents charge from leaking through the transfer material to the toner layer. However, if the corotron is too small, the amount of corona

is affected by small fluctuations in the power source. It is found that the optimal corotron dimensions are $l_2 = 5.0 \text{ mm}$ with a 10 mm opening. The agreement between the theory and experiment is excellent. With this corotron design, the minimum transfer time is 1.5 ms and the maximum paper speed is 6.7 m/s.

Figure 14 shows the relationship between transfer time and the air gap between the toner layer and transfer paper as calculated by Equation (17). The smaller the air gap, the shorter the transfer time. If enough pressure is applied to the roller, the air gap can be reduced to $1 \mu\text{m}$. With this gap, the transfer time is less than $8 \mu\text{s}$ and, if the nip is 1 mm, the paper speed can be 125 m/s.

3.2.2 Measuring high-speed transfer

The transfer ratio of the three transfer techniques is shown in Fig. 15. At paper speeds faster than 60 cm/s, the transfer ratio of each technique is greater than 80 percent and is constant. At low paper speeds, the transfer ratio of dielectric roller transfer is constant, but those of conductive roller transfer and corona transfer decrease because at low paper speeds, more charge leaks through the transfer material, neutralizing the toner charge and decreasing the electric field.

4. Conclusion

Electrostatic transfer was investigated both theoretically and experimentally.

The transfer mechanism and optimum transfer conditions were the same for corona transfer and roller transfer (both conductive roller transfer and dielectric roller transfer). The transfer ratio reached a maximum in an electric field of 36 MV/m in the air gap, which corresponds to a surface charge density of $320 \mu\text{C/m}^2$ due to air breakdown. There is a toner charge/mass ratio which gives the maximum transfer ratio at the electric field. At least 0.7 kg/cm^2 of pressure is required for good toner image transfer.

The theoretical limit of the transfer speed is 6.7 m/s for corona transfer and 125 m/s for roller transfer. An acceptable toner transfer image, with a transfer ratio of more than

80 percent was obtained on plain paper at paper speeds up to 2 m/s.

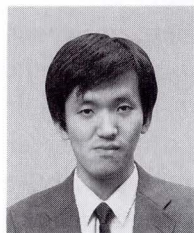
References

- 1) Sato, F., Maki, H., and Nakamura, K.: On electrophotographic transfer. (in Japanese), *Electrophoto.*, **4**, 2, pp. 32-36 (1962).
- 2) Nagashima, S., and Goto, K.: The photoengraving process using electrophotographic materials. (in Japanese), *Electrophoto.*, **3**, 1, pp. 32-38 (1961).
- 3) Kutsuwada, N., and Namiki, R.: Studies on the transfer of electrophotographic powder image (1). (in Japanese), *Electrophoto.*, **9**, 3, pp. 18-24 (1970).
- 4) Yang, C.C., and Hartman, G.C.: Electrostatic separation of a charged-particle layer between electrodes. *IEEE Trans. Electron Devices*, **ED-23**, 3, pp. 308-312 (1979).
- 5) Takahashi, H., Kimura, M., Nakajima, J., and Horie, M.: Studies on Corona Discharge Transfer of Toner Image. (in Japanese), *Trans. IECE, Jpn.*, **J60-C**, 3, pp. 148-153 (1977).
- 6) Takahashi, H., Kimura, M., Nakajima, J., and Horie, M.: Studies on Roller Transfer of Toner Image. (in Japanese), *Trans. IECE, Jpn.*, **J60-C**, 4, pp. 213-218 (1977).
- 7) Kimura, M., Nakajima, J., and Horie, M.: Electrostatic Transfer of Toner Image. *FUJITSU Sci. Tech. J.*, **18**, 2, pp. 267-285 (1982).
- 8) Kimura, M.: Charged Particles in Transfer and Cleaning Processes. (in Japanese), *Electrophoto.*, **27**, 4, pp. 601-606 (1988).
- 9) Hyakutake, N., and Terao, K.: Study on Electrostatic Transfer. (in Japanese), *Proc. Electrostatics*, pp. 105-108 (1984).
- 10) Hida, M., Nakajima, J., and Takahashi, H.: Effects of toner charge on electrostatic toner transfer. *IEEE Ind. Appl. Soc.*, 1982 Annual Meet. Conf. Rec., pp. 1225-1228.
- 11) Horie, M., Kimura, M., Nakajima, J., and Takahashi, H.: High Speed Transfer of Toner Image. (in Japanese), *Trans. IECE, Jpn.*, **J60-C**, 6, pp. 335-342 (1977).
- 12) Schaffert, R.M.: *Electrophotography*. 2ed., New York, Focal Press, 1975, pp. 254-256.
- 13) Cobine, T.D.: *Gaseous Conductors*. 1ed., New York, Pover, 1958, pp. 233-238.



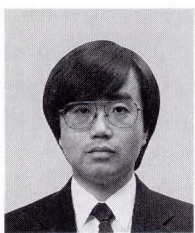
Masatoshi Kimura

Printer Technology Laboratory
FUJITSU LABORATORIES, ATSUGI
Bachelor of Electronic Eng.
Okayama University, 1973
Dr. of Electronic Eng.
Osaka University, 1986
Specializing in Electrophotography
and Electrostatic Recording



Hiroshi Nou

Printer Technology Laboratory
FUJITSU LABORATORIES, ATSUGI
Ube Technical College, 1984
Specializing in Electrophotography



Masahiro Wanou

Printer Technology Laboratory
FUJITSU LABORATORIES, ATSUGI
Bachelor of Electrical Eng.
Kobe University, 1978
Master of Electronics
Kobe University, 1980
Specializing in Electrophotography

Color Gamut Evaluation Method for Color Hard Copies

• Jun Moroo • Toshio Konaka • Tomohisa Mikami

(Manuscript received November 1, 1989)

In this paper, an image quality evaluation method for color gamut is studied. In subjective assessments for color gamut in color hard copies, color wedges were found to be more useful than natural images for designing color devices.

Furthermore, it is also shown by experiment that unwanted density can be assessed in addition to primary density by calculating a block ink density whose color hexagon inscribes that of actual inks.

1. Introduction

When designing and fabricating color imaging devices such as color printers and copiers, it is important to first determine a target opinion score for image quality. Major parameters for color image quality are resolution, number of gradation levels, graininess, and color gamut. This paper discusses the evaluation of color gamut. Design of color imaging devices requires optimization of parameters. This is not possible unless we know exactly the available range of parameters, and the relationship between the parameters and opinion scores. Knowledge of this relationship enables determination of parameters for the target opinion score, and prediction of opinion scores of color imaging devices. The relationship is especially important in color printer design because of the large trade-off between parameters.

So far, many studies have been conducted to evaluate the relationship between opinion score and resolution, gradation levels, and graininess. However, no evaluation has been made for color gamut. This may be due to the complexity of the relationship, which depends heavily on the kinds of images used for the subjective assessments.

The authors have already proposed finding the exact relationship between opinion score

and resolution, and that between opinion score and number of gradation levels, by using simple artificial patterns such as black circles and color wedges instead of natural images¹⁾. In this paper, a similar approach was taken to find the relationship between opinion score and color gamut. When evaluating color gamut, the unwanted density as well as the primary density should be taken into account. This paper also discusses the evaluation of color gamut using equivalent block ink density, which is calculated using the CIE 1976 UCS diagram ($u'v'$ chromaticity diagram).

This paper first describes the evaluation of the relationship between the opinion score and color gamut using natural and artificial images. Then the measurement of color gamut using equivalent block ink density is discussed.

2. Evaluation of relationship between opinion score and color gamut

2.1 Natural image

The ten natural images shown in Fig. 1 were printed with four density ranges, and were subjectively assessed. The images were printed on 114.2 mm × 91.4 mm paper by a photothermographic printer with the resolution of 11.2 pixels/mm and 256 gradation levels. Ten people were asked to grade the image



Fig. 1—Natural images used for subjective assessment.

Table 1. Subjective evaluation category

Score	Impairment
5	Imperceptible
4	Perceptible but not annoying
3	Slightly annoying
2	Annoying
1	Very annoying

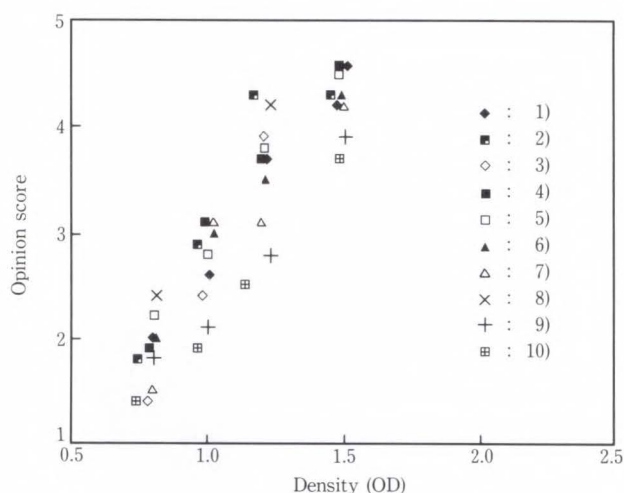


Fig. 2—Evaluation results of natural images.

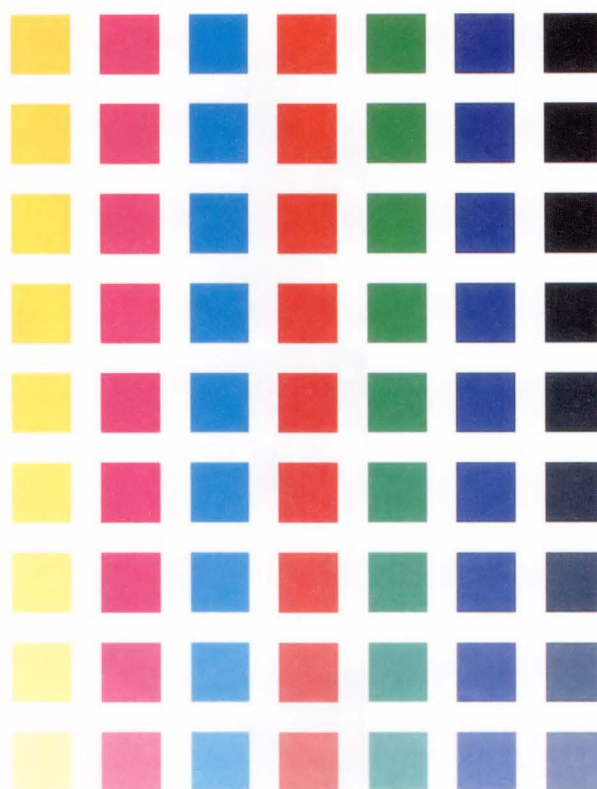
quality on the CCIR five-grade scale shown in Table 1.

Figure 2 lists the assessment results. The horizontal axis is optical ink density. The vertical axis is the opinion score. For equal optical densities, opinions scores depend greatly on the kinds of images.

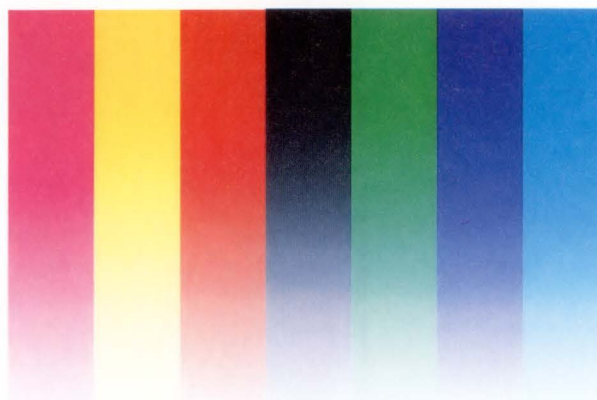
2.2 Artificial image

To make the assessment results more objective, the authors looked for images that are always scored more severely than any natural image. First, 10 mm × 10 mm color patches in Y (yellow), M (magenta), C (cyan), R (Red), G (green), B (blue), and K (black) were subjectively assessed. Figure 3a) shows the color patches.

All the primary densities for Y, M, C, R, G, B, and K were set equal to one of eight densities. Some opinion scores were lower than those of natural images, but the others were higher,



a) Color patch

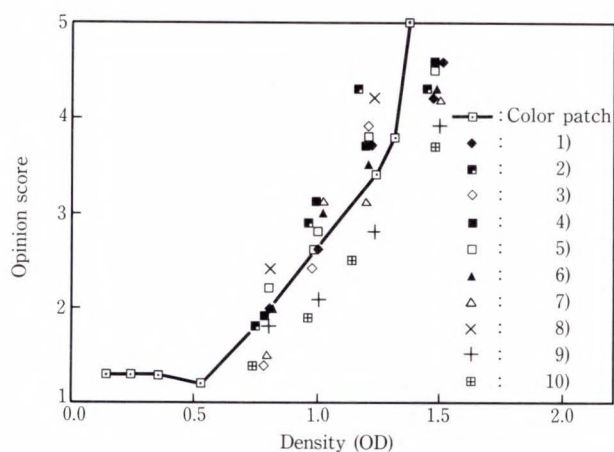


b) Color wedge

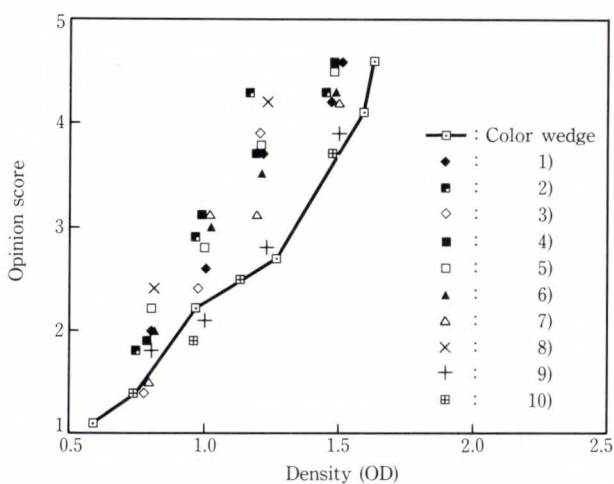
Fig. 3—Artificial patterns.

as shown in Fig. 4a). This means that color patches are not suitable for the assessment of color gamut.

Color wedges of Y, M, C, R, G, B, and K were then assessed. Each had a primary density of zero at one side and the maximum value at the other side. All the primary densities



a) Color patch



b) Color wedge

Fig. 4—Evaluation results of artificial patterns.

for Y, M, C, R, G, B, and K were set equal to one of six densities. Figure 3b) shows the color wedges. The printed area is 113 mm × 91 mm. As is shown in Fig. 4b), color wedges are judged more severely than natural images, but not too severely. The solid line in Fig. 4 gives the relationship between primary density and the minimum opinion score. Accordingly, color wedge patterns are better than natural images for assessing color gamut.

3. Measurement of color gamut

3.1 Primary density

In reproducing color images, inks in three or more colors are needed. Generally, three primary inks are used. These are Y, M, and C. Consequently, there are three primary densities

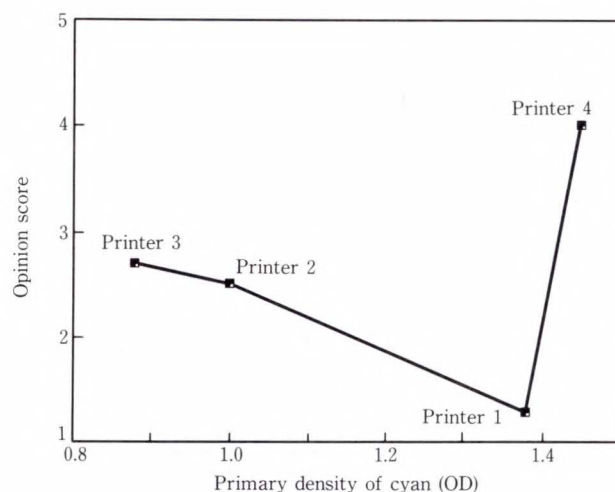


Fig. 5—Results of assessing devices using the primary density of cyan.

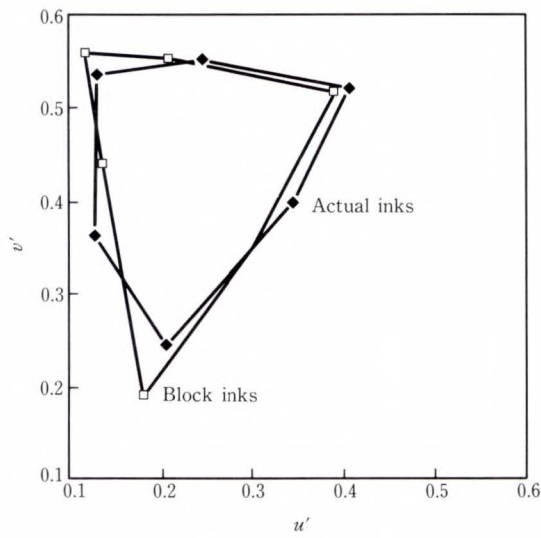
Table 2. RGB densities of each device (Cyan)

Printer	Primary density	Unwanted density		Printing technology
	R	G	B	
Printer 1	1.38	0.61	0.57	Photography
Printer 2	1.00	0.51	0.30	Dye diffusion thermal transfer
Printer 3	0.88	0.32	0.26	Dye diffusion thermal transfer
Printer 4	1.45	0.59	0.35	Photo-thermography

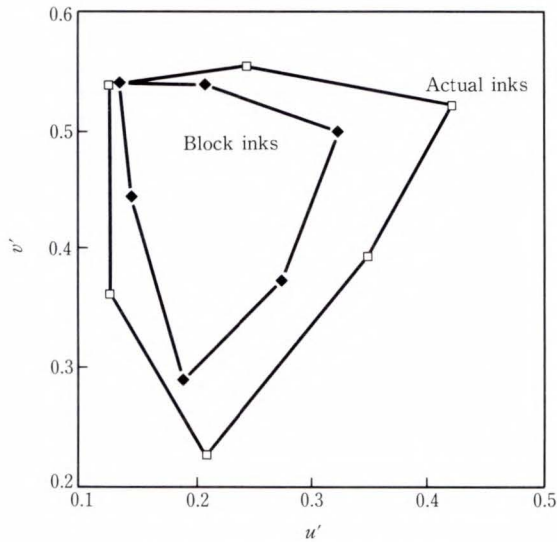
for a certain set of color inks. In addition, primary density is largely dependent on the color filter bandwidth used to measure the primary density. It is therefore difficult to compare color gamuts of sets of color inks using primary density.

Furthermore, primary density neglects unwanted density, which sometimes degrades color gamut to a large extent. Figure 5 gives the results of assessing color wedges printed by four color printers: an instant photographic video printer, two dye diffusion thermal transfer video printers, and a photothermographic printer. Opinion scores do not increase with primary density. This is mainly due to the unwanted density.

Table 2 lists the primary and unwanted densities of cyan. The primary densities of



a) Equal area method



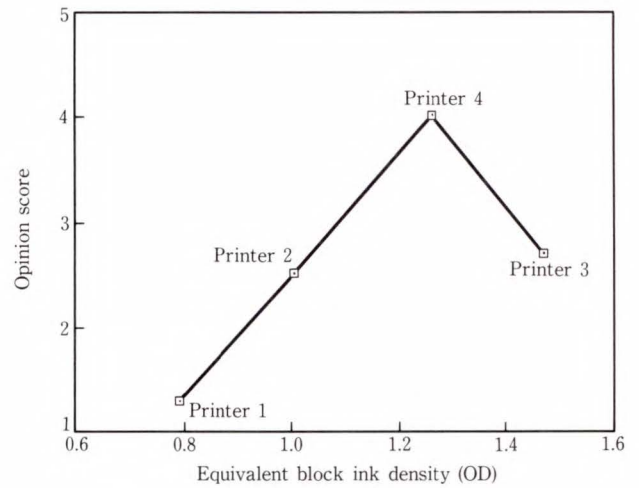
b) Inscribed density method

Fig. 6—Calculation of equivalent block ink density.

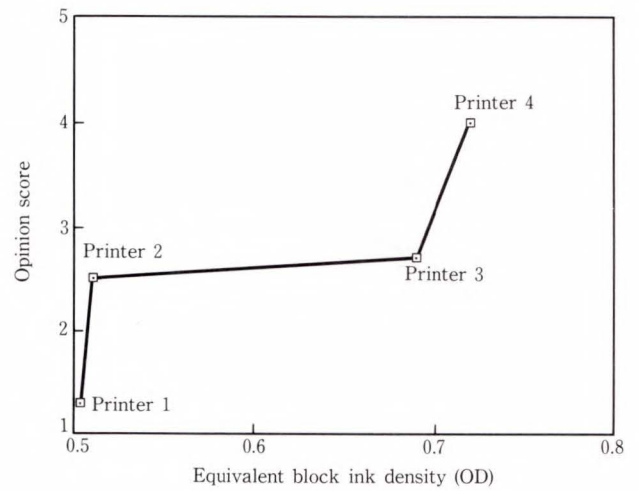
printers 1 and 4 are almost equal. Unwanted blue density of printer 1 is much higher than that of printer 4. This raises the opinion score of printer 4. The primary density of printer 2 is higher than that of printer 3, but printer 2 has a higher unwanted green density. Consequently, the opinion scores of printers 2 and 3 are almost equal.

CIE chromaticity diagrams (xy or $u'v'$) are widely used to compare color gamut²⁾. These diagrams only allow rough comparisons because the comparison is made in shapes, not numbers.

In the evaluation of colorants, the color



a) Equal area



b) Inscribed area

Fig. 7—Results of assessing devices using equivalent block ink density.

circle method³⁾ is generally used. This method compares hue differences and unwanted densities graphically. However, no study had been made to clarify the relationship between opinion scores.

3.2 Equivalent block ink density

The authors propose calculating equivalent block ink density as a solution to these problems. In this calculation, the block inks which make color hexagon with the largest area in $u'v'$ chromaticity diagram is used. Densities of reflective areas are equal to zero. Densities of absorptive areas for Y, M, and C are all

Table 3. Primary densities of printer 4

	Y	M	C
a)	0.68	0.59	1.31
b)	0.82	0.58	1.29
c)	0.82	0.78	1.29
d)	1.48	1.15	1.24
e)	1.61	1.59	1.60

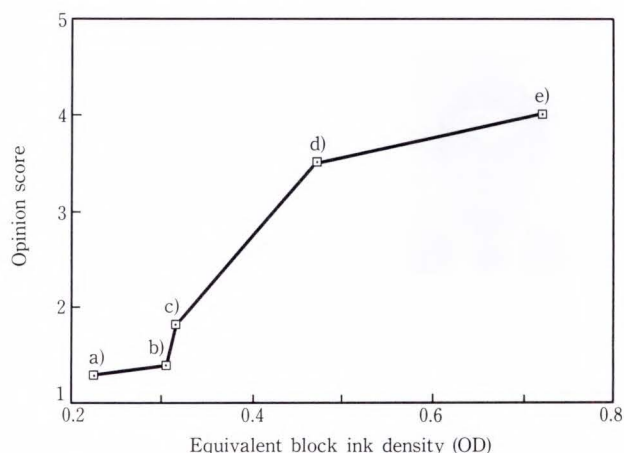


Fig. 8—Results of assessing a photothermographic printer using equivalent block ink density.

equal. By simulation, transition wavelengths of the block inks which make the largest color hexagon in $u'v'$ chromaticity diagram were found to be 495 nm and 580 nm. It is preferable to make calculations in $L^*a^*b^*$ uniform color space⁴⁾, but the amount of calculation is enormous.

When block ink density is zero, color hexagon area is zero. Color hexagon area increases as block ink densities become higher. When block inks and actual inks have the same densities, color hexagon area of block inks is always larger than that of actual inks because block inks have no unwanted densities. First, block inks with the same color hexagon area as that of actual inks, as shown in Fig. 6a), were studied. The four color printers listed in Table 2 were evaluated. Opinion scores do not increase with the equivalent block ink density, as is shown in Fig. 7a). It seemed that distortion of the color hexagon shape had a large influence on the results. According to this result,

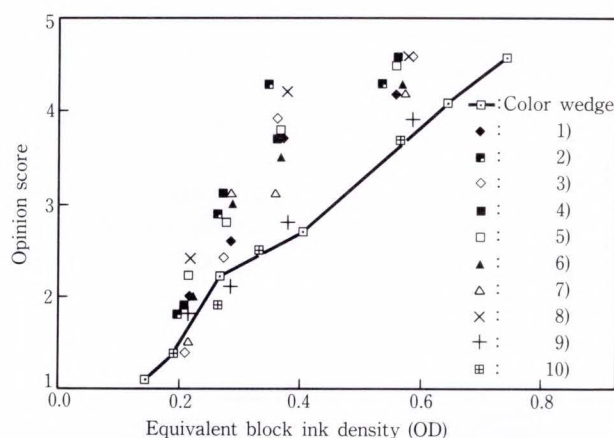


Fig. 9—Results of assessing color gamut using equivalent block ink density.

equivalent block ink density was calculated based on the color hexagon shape, not area. Block inks that make a color hexagon inscribing that of actual inks, as shown in Fig. 6b), were then studied.

Assessment results for the four color printers using the equivalent block ink density are shown in Fig. 7b). Opinion scores increase with the equivalent block ink density. Next, color wedges were printed by printer 4 with density range combinations shown in Table 3. Figure 8 shows the results of assessment. Opinion scores also increase with the equivalent block ink density. When equivalent block ink density is used, Fig. 4 becomes Fig. 9.

4. Conclusion

An evaluation method for color gamut in color imaging devices has been proposed. It is shown that color wedges in Y, M, C, R, G, B, and K are scored more severely than any natural images. Consequently, the artificial pattern is useful in subjective assessment of color imaging devices.

It is also shown that the density of block inks that make a color hexagon inscribing that of actual inks in $u'v'$ chromaticity diagram has good correlation with opinion scores for color gamut. This enables numerical comparison of color gamut using density while taking unwanted density into account.

References

- 1) Naka, T., Mikami, T., and Mori, M.: Tolerant values of gradation levels and resolution for color printers. (in Japanese), Proc. 2nd Joing Conf. Color Tech., 1987, pp. 81-84.
- 2) Kotera, H.: Tone and Color Reproduction Method for Hard-copy Devices. (in Japanese), *J. Inst. Television Eng. Jpn.*, **37**, 7, pp. 546-552 (1983).
- 3) Color Science Assoc., Jpn.: Handbook of Color Science. (in Japanese), Tokyo, University of Tokyo Press, 1980, pp. 1016-1017.
- 4) Tamune, M., Sayanagi, K.: Considerations on transition wavelength of block inks in subtractive color mixtures. (in Japanese), Proc. 1st Joint-Conf. Color Tech., 1984, pp. 25-28.



Jun Moroo

Printer Technology Laboratory
FUJITSU LABORATORIES, ATSUGI
Bachelor of Electronic Eng.
Tokyo University of Agriculture and
Technology 1984
Master of Electronic Eng.
Tokyo University of Agriculture and
Technology 1986
Specializing in Processing and Evaluation
of Color Images



Tomohisa Mikami

Printer Technology Laboratory
FUJITSU LABORATORIES, ATSUGI
Bachelor of Electronic Eng.
Hokkaido University 1974
Master of Electronic Eng.
Hokkaido University 1976
Specializing in Imaging Device Control



Toshio Konaka

Printer Technology Laboratory
FUJITSU LABORATORIES, ATSUGI
FUJITSU Technical Colledge 1975
Specializing in Imaging Device Control

A Filter-Alternating Color Scanner

• Shoji Suzuki • Mitsuhiro Tsuda • Masahiro Mori

(Manuscript received August 31, 1989)

A small and fast color scanner having precise color digitization has been developed. The scanner was designed using colorimetric simulation so that its characteristics match the RGB standard response. The filters and compensation matrix are adjusted to minimize color differences between the simulated and measured colors of the CIELAB color specimens.

A filter-alternating mechanism for color separation was developed. A transparent filter is used for high speed monochrome scanning.

The prototype scanner features excellent color performance, an average color difference of seven, and high speed monochrome scanning (six seconds for an ISO A4-size document).

This color scanner is as small as a monochrome scanner.

1. Introduction

Recent developments in computers have made full color image processing practical and easy. More and more areas are using digital color images, and several color scanners have been developed¹⁾. The most important requirement for color scanners is precise color digitization. Precise color digitization means that the output has exactly the same colors as the source. Colors must be expressed quantitatively. The CIE-RGB standard (human eye characteristics) established by the CIE (Commission Internationale de l'Eclairage), and the NTSC-RGB TV standard are both widely used. If the scanner output follows a common standard, image processing and display can be more precise. As yet, no scanner output standard has been defined; but in the future, such a standard will become a necessity.

To make the output match a standard, the scanner's spectral response must also match a standard. We developed a way to determine a scanner's spectral response by using computer colorimetric simulation.

A color separation method must be selected when the scanner is manufactured. There are many ways to separate color, for example: three filters and three line sensors, a color sensor of

picture elements covered with color filters, and light source switching^{2),3)}. The method used affects the scanner's performance, size, speed, and cost. A scanner using three filters and three line sensors is fast but big. It is also very hard to adjust the scanning lines of each sensor. A scanner using a color sensor of picture elements covered with color filters is fast and compact, but precise color digitization is difficult because the filters cannot be freely selected. Light source switching is slow and requires bulky equipment. We aimed at precise color digitization by free selection of color filters in a small device. The filter-alternating mechanism we developed switches color filters in front of an image sensor for each line. To achieve both precise color digitization and high speed monochrome scanning, white (transparent), yellow, and red filters are used. Monochrome scanning uses a white filter only.

This paper describes the design of the scanner, its color characteristics and color separation, and the prototype⁴⁾.

2. Scanner structure and design objectives

2.1 Scanner structure

Figure 1 is a schematic of the color scanner. A color document is illuminated by the white

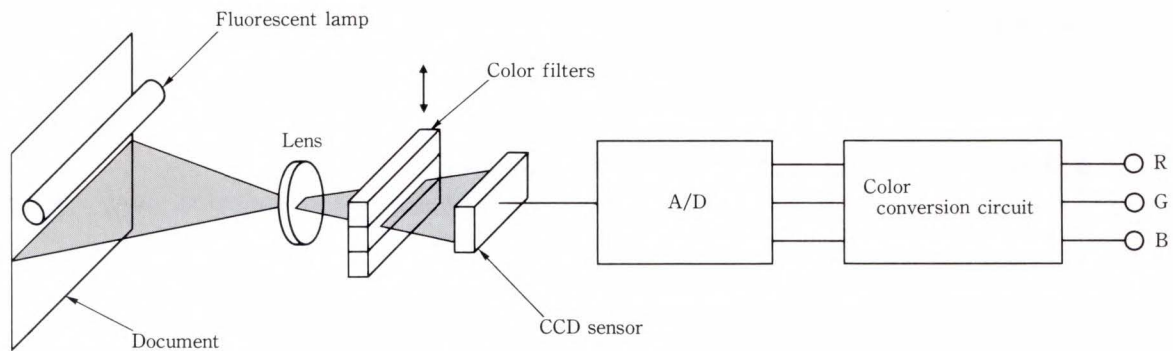


Fig. 1—Model of color scanner.

fluorescent lamp. The reflected light is focused by the lens through the color filters and onto the CCD sensor. The sensor transduces the amplitude of the incident light to an electrical signal. The sensor output is digitized by the A/D converter and the color conversion circuit converts this into red, green, and blue signals.

2.2 Scanner design objectives

Color scanners must have precise color digitization, and must be small and fast. Color scanners should not be much larger or slower than monochrome scanners.

1) Precise color digitization

For the scanner output to match a standard, the synthesized spectral response should also match a standard. However, electrical compensation cannot exactly match the scanner and standard spectral responses. This is because of bright lines from the fluorescent lamp and the uneven spectral response of the CCD sensor. To match responses we minimized the error for as many colors as possible and developed a way to minimize the average error.

2) High speed monochrome scanning

Generally, a color scanner can be used for both color and monochrome scanning. However, until now, color scanning has been three times slower than monochrome scanning. Our goal was a monochrome scanning speed equal to that of a monochrome scanner.

3) Compact optical system

Color scanners should not be much larger than monochrome ones. We decided to develop a compact color separation mechanism.

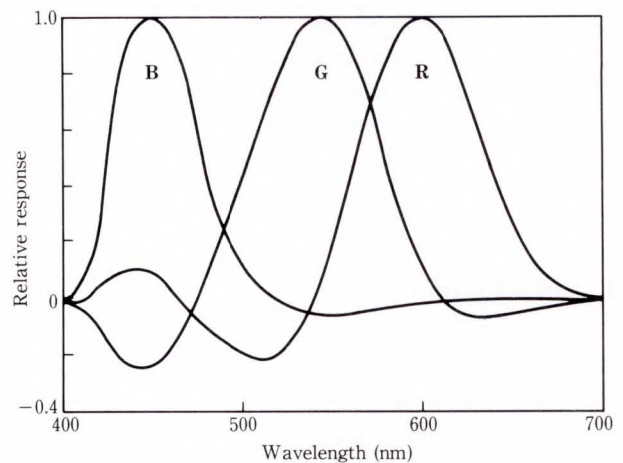


Fig. 2—NTSC-RGB response.

3. Design of color performance

To match the scanner's output with a standard, we developed a way to determine the spectral response using computer colorimetric simulation.

3.1 Spectral response design

Electrical compensation is useful because it is difficult to design color separation filters to compensate for the bright lines of the fluorescent lamp and the uneven response of the CCD sensor. Further more, standards like NTSC-RGB (see Fig. 2) have a negative response. Optical elements all have positive responses. Color performance without a negative response decreases the color depth of all digitized colors (see Fig. 3). A method to create a negative response (electronic compensation of sensor output) is necessary. Because of the uneven

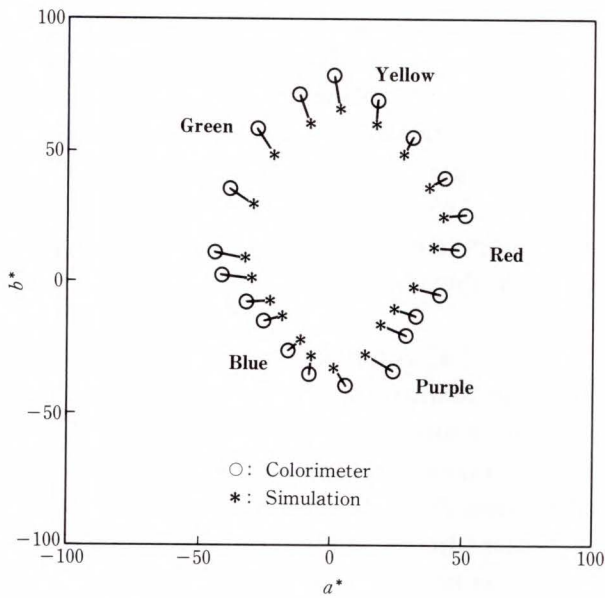


Fig. 3—Color performance without negative response.

response and the negative response, we developed an electronic compensation method.

Sensor output O_i is expressed by

$$O_i = \int D(\lambda)L(\lambda)F_i(\lambda)C(\lambda)S(\lambda)d\lambda, \quad (1)$$

where,

- i : Separation color (1, 2, 3)
- λ : Wavelength
- O_i : Sensor output
- $D(\lambda)$: Spectral reflectance from color specimen
- $L(\lambda)$: Spectrum of fluorescent lamp
- $F_i(\lambda)$: Spectral transmittance of color filter
- $C(\lambda)$: Spectral sensitivity of CCD image sensor
- $S(\lambda)$: Spectral response of other optical elements.

Negative response is achieved using the matrix operation in Equation (2). This is color conversion.

$$\begin{pmatrix} R \\ G \\ B \end{pmatrix} = \begin{pmatrix} m_1 & m_2 & m_3 \\ m_4 & m_5 & m_6 \\ m_7 & m_8 & m_9 \end{pmatrix} \begin{pmatrix} O_1 \\ O_2 \\ O_3 \end{pmatrix}, \quad \dots (2)$$

where,

- $T(R, G, B)$: Scanner output
- $M(m_1 - m_9)$: Conversion matrix
- $O(O_1, O_2, O_3)$: Sensor output.

To compensate using Equation (2), the nine elements of the matrix must be determined. These elements depend on the optics and on an objective standard response. Generally, the nine elements can be determined from nine equations, which come from the three colors. If these elements are determined from three colors, these three colors can be converted perfectly. However, there is no guarantee that other colors will be precisely digitized. A way to minimize the average error for a large number of colors is needed.

3.2 Definition of matrix elements

We used the least squares method to minimize the average error. We chose the nine elements to minimize the average errors of color values.

The method of minimizing the average error is expressed in Equation (3)⁵.

$$M = (P_n \cdot O_n^t)(O_n \cdot O_n^t)^{-1}, \quad \dots (3)$$

where,

- P_n : Color value in the objective standard for n color specimens
- O_n : Sensor output for n color specimens
- M : Conversion matrix.

P_n and O_n are three-row, n -column matrixes. O_n is calculated by computer from Equation (1), P_n is the color value consisting of n color specimens in a standard. These values were measured with a colorimeter. From Equation (3) the conversion matrix M is fixed to minimize the error of P_n and O_n .

There are two problems with this method. The first is how to select colors to determine the matrix. (Compensation is considerably influenced by this selection.) The second is the quantitative estimate of the error.

People evaluate color error using a combination of hue, brightness, and saturation. If the conversion matrix is designed using colors which can be converted from the RGB scanner output and matches our visual characteristics, the error people perceive can be minimized. We used the colors in the CIELAB color space (see Fig. 4). This space was determined by

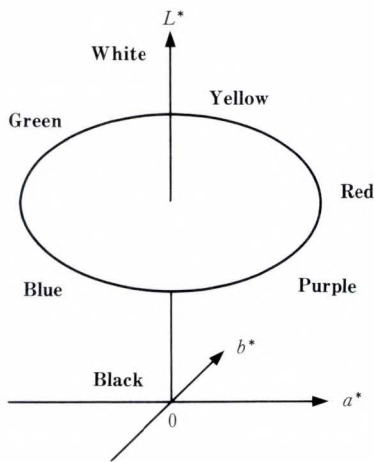
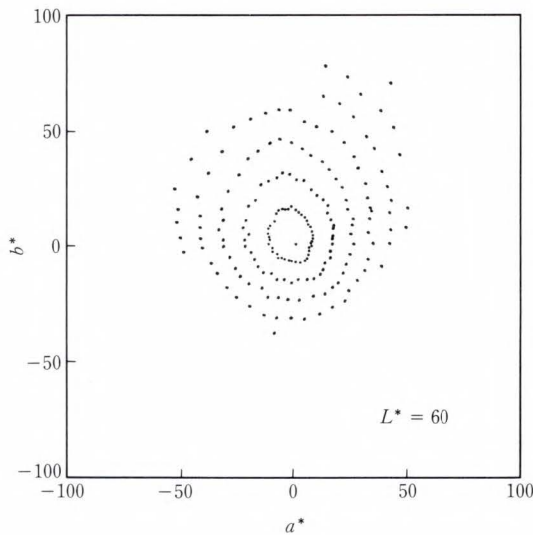
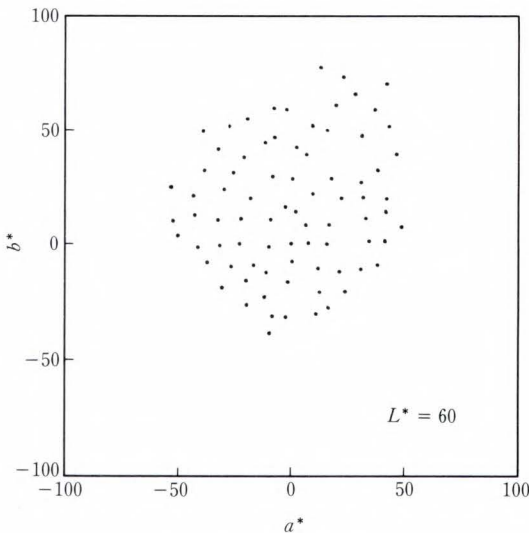


Fig. 4—CIELAB color space.



a) JIS color chips



b) Selected colors

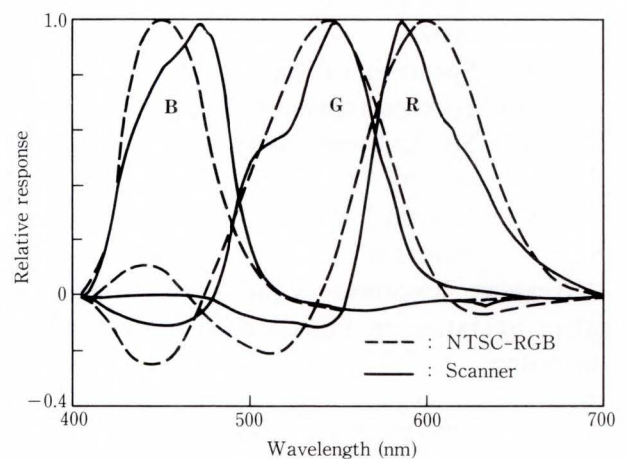
Fig. 5—Color selection.

CIE and is based on the eye's color response. L^* represents brightness, and the position in the a^* and b^* planes define hue and saturation. The distance between colors is the color difference and is proportional to the eye's sensitivity. We filled our conversion matrix with colors equally distributed in this space, and used the color difference to evaluate the error.

The 1142 color chips of the Japanese Industrial Standards were measured and their positions within the space were determined. Figure 5a) shows the colors within the a^* and b^* planes when L^* is 60. Colors are concentrated at the center. In the matrix obtained, the colors at the center are more weighted. The conversion error of the colors in the periphery is larger than that of those at the center. To minimize the error for many colors, the colors must be equally distributed. We selected 439 equally distributed colors in Fig. 5b) and chose the matrix elements to minimize the average error.

3.3 Performance evaluation

We evaluated the matching between the scanner output and the NTSC-RGB standard, and evaluated the average matching error.



Colorimetric factor	
R	0.93
G	0.97
B	0.90

Fig. 6—Synthesized spectral response.

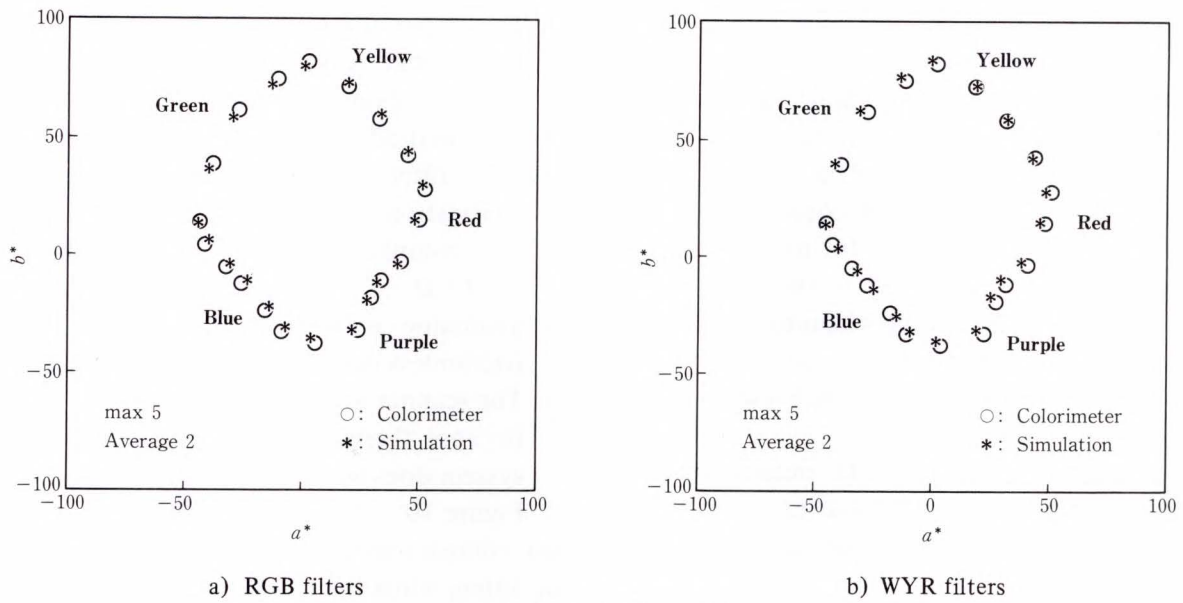


Fig. 7—Color performance.

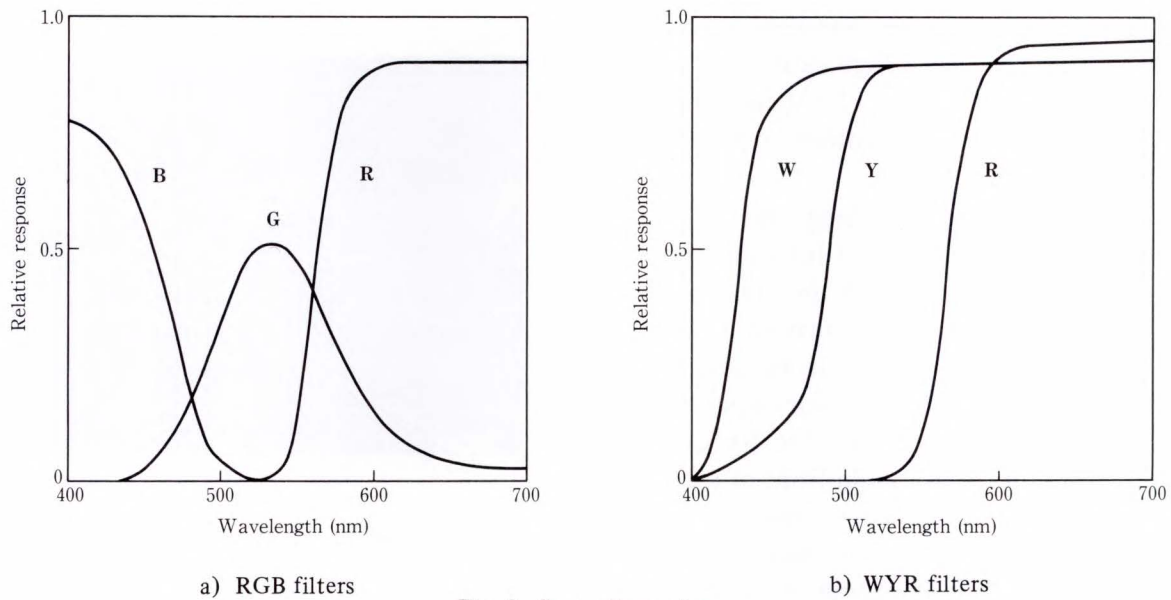


Fig. 8—Separation color.

Figure 6 is the synthesized spectral response which combines the response of the optical system with the conversion matrix. Each colorimetric factor of R, G, and B is more than 0.9, and this is sufficient⁶⁾. Scanner characteristics agree almost perfectly with the NTSC-RGB standard.

Figure 7a) is the simulated color performance of a scanner having the characteristics shown in Fig. 6. Using RGB separation, twenty colors were precisely digitized. The differences between the measured and simulated

values are less than five, which is barely discernible.

3.4 Color separation

The matrix operation combines color compensation and color conversion. It can be used for color separation with non-RGB filters {see Fig. 7b)}. These results are also good. We use WYR color separation for fast monochrome scanning.

Figure 8 shows the spectral response of the RGB and WYR filters. RGB color scanners

use a green filter for monochrome scanning. The green filter passes green light but over-attenuates other frequencies and thus slows scanning. To get the same intensity of light as in a monochrome scanner, a white filter should be used. We chose WYR color separation and used only the white filter for monochrome scanning. The scanning speed is the same for both color and monochrome scanning. In color scanning, the WYR output is converted to RGB without increasing the color error (see Fig. 7).

To obtain the same CCD output level, the white filter requires 2.1 ms per line and the green filter requires 6.9 ms per line.

4. Color separation mechanism

To achieve precise color digitization, high speed monochrome scanning, and compactness, we must be able to select filters easily and scan with only one CCD sensor. To achieve this, we developed a color separation mechanism using filter switching.

Generally, in filter switching, the whole page needs to be scanned once for each color because the switching speed is too slow. Page memory is needed for color conversion. It is better if the three color signals can be obtained line-by-line. We developed a color separation mechanism which does this (see Fig. 9). Color strip filters are quickly placed in front of a CCD sensor. The filters are placed so that the displacement of the filters and the light required can be minimized. This is energy efficient and allows fast filter switching.

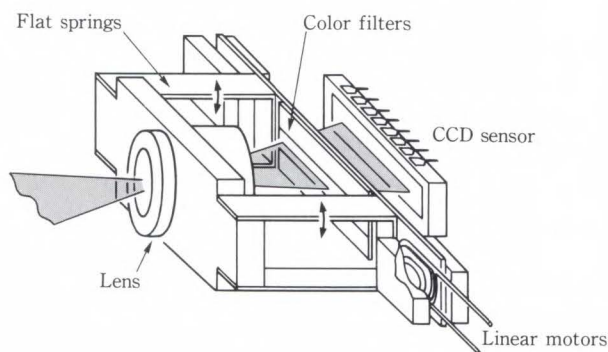


Fig. 9—Filter switching mechanism.

The upper filter is red, the center is white, and the lower is yellow. Filters are switched by moving-coil linear motors.

This method has several advantages:

- 1) Easy filter selection permits precise color digitization.
- 2) The compact optics use only one lens and one CCD.
- 3) Switching is fast. (This is done using a frictionless mechanism with flat springs.)
- 4) The scanner is simple.
- 5) Because there is only one CCD, the optical system does not have to be adjusted.

Figure 10 shows the filter movement. Our compact servo-positioning system positions the filters while the CCD integrates the reflected

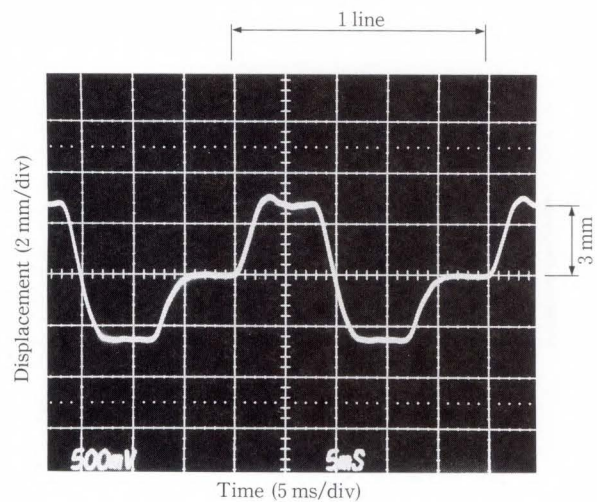


Fig. 10—Filter movement.



Fig. 11—Prototype scanner.

Table 1. Specifications

Item	Specification
Document size	A4-size max
Scanning system	Flat-bed
Color separation	Filter-alternation
Separation color	White, yellow, red
Scanning time	60 s/A4-size (color) 6 s/A4-size (monochrome)
Scanning resolution	8 pels/mm
Graduation level	256 levels
Output signal	NTSC-RGB

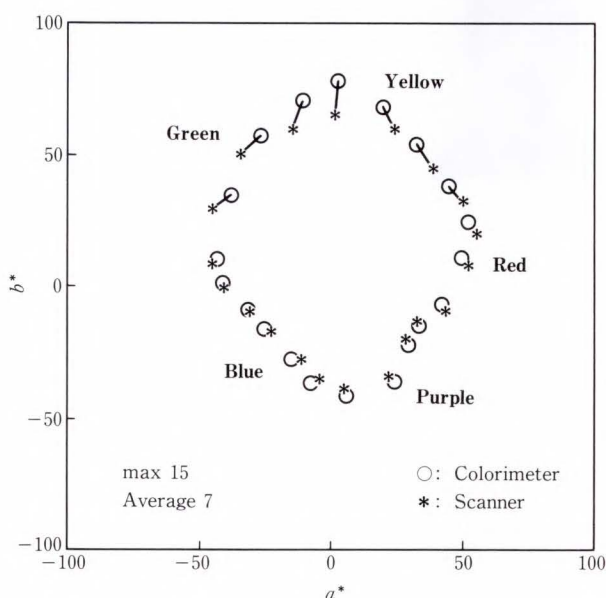


Fig. 12—Color performance.

light. Scanning a line involves three filter switchings and three color integrations. The CCD integration time is 10 ms, and the total switching time is 15 ms. It takes only 25 ms to scan one line. This is 40 lines per second. An ISO A4-size document can be scanned in 1 min. This is slower than most monochrome scanners, but very fast for a color scanner.

5. Prototype scanner

Figure 11 shows our prototype scanner, and Table 1 gives its specifications. Flat-bed scanning is used so that both books and single sheets can be scanned. The scanning time for an ISO A4-size document is 60 s for color and 6 s for monochrome. The resolution is

eight picture elements per millimeter and the gradation is 256 levels for each color. The output conforms to the NTSC-RGB standard. This is convertible from CIE-RGB and is convenient for color CRT monitors.

WYR is converted to RGB by ROMs holding the conversion tables. This is compact and keeps the conversion time short.

Figure 12 shows the color performance for 20 colors. The results agree well with the simulation. The average color difference is seven. Unfortunately, because a standard for color scanners has not been defined, exact comparison with other scanners is impossible; however, most scanners would have a color difference of more than ten.

A considerable portion of the average error is due to the relatively poor color performance for yellow. We are now looking for ways to overcome this problem.

6. Conclusion

We have developed a way to design color scanners so that the spectral response matches a standard. The sensor output was adjusted to minimize the average error for a large number of colors equally distributed in the CIELAB color space.

WYR color separation enables a monochrome scanning speed that is 3.3 times faster than RGB scanners. Color compensation and WYR to RGB conversion are done at the same time. Color digitization was precise and monochrome scanning was fast.

For color separation, we developed a compact mechanism that quickly switches filters.

Our prototype scanner features excellent color performance, an average color difference of seven, and high-speed monochrome scanning (six seconds for an ISO A4-size document).

References

- 1) Nagano, F., Misaka, S., and Mori, H.: Desktop Color Document Scanner. Proc. SID 1985 SID Int. Symp., Orlando, Fla., pp. 40-41.
- 2) Takeuchi, R., Tsumura, M., Tadauchi, M., and Shio, H.: Color Image Scanner with an RGB Linear Image Sensor. *J. Imaging Technol.*, **14**, 3, pp. 68-72 (1988).

- 3) Katoh, M., Hamaguchi, T., Satoh, T., Yashima, O., and Ishikura, H.: A Contact Type Color Image Sensor and its Color Reproduction Characteristics. Proc. IGC 1989 Electronic Imaging '89 West, 2, Pasadena, Calif., pp. 556-561.
- 4) Suzuki, S., Tsuda, M., and Mori, M.: A Filter-Alternating Color Scanner. Proc. IGC 1988 Electronic Imaging '88 East, 2, Boston, Mass., pp. 1018-1023.
- 5) Wallis, R.H.: "Appendix B. Multidimensional mappings, and least squares curve fitting of surfaces". *Film Recording of Digital Color Image*, Los Angeles, Calif., USCIPI Rep. 570, 1975, pp. 174-178.
- 6) Yule, J.A.C.: "6. Special sensitivities for color separation". *Principles of Color Reproduction*, 1st ed., New York, John Wiley & Sons, 1967, pp. 126-150.



Shoji Suzuki

Holography and Color-Imaging Laboratory
FUJITSU LABORATORIES, ATSUGI
Bachelor of Precision Machinery Eng.
The University of Tokyo, 1980
Specializing in Color Imaging Technology



Masahiro Mori

Holography and Color-Imaging Laboratory
FUJITSU LABORATORIES, ATSUGI
Bachelor of Mechanical Eng.
Tokyo Institute of Technology, 1973
Master of Mechanical Eng.
Tokyo Institute of Technology, 1975
Specializing in Color Imaging Technology



Mitsuhiro Tsuda

Holography and Color-Imaging Laboratory
FUJITSU LABORATORIES, ATSUGI
Bachelor of Mechanical Eng.
Kansai University, 1983
Master of Mechanical Eng.
Kansai University, 1985
Specializing in Color Imaging Technology

Holographic Fingerprint Sensor

• Seigo Igaki • Shin Eguchi • Takashi Shinzaki

(Manuscript received November 10, 1989)

A sensor for personnel identification that uses a laser light source has been developed. It consists of a transparent light-conducting glass plate with a plain grating hologram, and a focusing lens under the hologram. Because the plate is plane-parallel, all optical paths from each point on the fingerprint to the hologram are equal, and a bright fingerprint image is obtained without the trapezoidal distortion inherent in prism sensors.

1. Introduction

Security continues to be an extremely important consideration in computer systems, and the ways in which it is implemented are legion. One popular way is the ID card, which provides efficient entry control to secure areas. However, cards can be lost or stolen. The use of a secret code is another efficient method of identification. It can be used, for example, to control the use of data entry terminals. But such codes can be easily guessed, especially in this age of personal computers and inventive hackers.

The fingerprint, being unique and unchangeable, remains the most reliable means of identification. A variety of ID and access control systems have been developed to identify users by fingerprint¹⁾.

Such fingerprint identification systems must operate in realtime and use an algorithm that quickly compares an input with previously registered fingerprints.

Such systems must also produce distortion-free fingerprint images unaffected by latent fingerprint images.

2. Conventional sensors

Most fingerprint sensors use a prism (see Fig. 1) into which a beam is introduced through one of the prism's angled surfaces. The beam undergoes total internal reflection at the top of the prism. When a finger is placed on the

prism, total internal reflection no longer occurs at the points of contact. Light incident at these points is not reflected, and a fingerprint image is imposed on the light reflected to the other angled surface. This image is then focused on the image pickup element (CCD) by a lens.

This method has two major problems:

- 1) Trapezoidal distortion caused by unequal optical paths between each point of the fingerprint and the image focusing lens.
- 2) Light noise caused by latent fingerprints.

A partial solution to these problems is shown in Fig. 2²⁾. The image pickup element is positioned beyond the light scattered from fingerprint ridges. This improves the contrast and is effective against light noise, but does little to eliminate trapezoidal distortion.

To solve the above problems completely, we developed a holographic sensor³⁾ consisting of a plain grating hologram and a flat glass plate with a laser light source.

3. Holographic fingerprint sensor³⁾

The transparent flat glass plate used in the holographic sensor has a hologram at one end and a fingerprint input port at the other (see Fig. 3). The laser beam is directed to the fingerprint input port from the back of the glass plate. The finger is simply pressed against the glass plate.

The sensor produces contrast by using the differences in the scattered light reflected

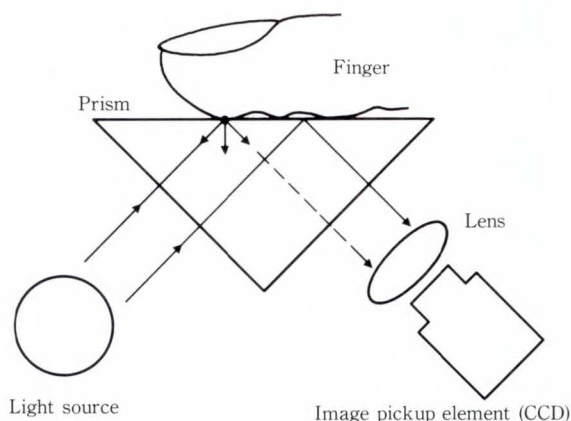


Fig. 1—Principle of prism fingerprint sensor-1.

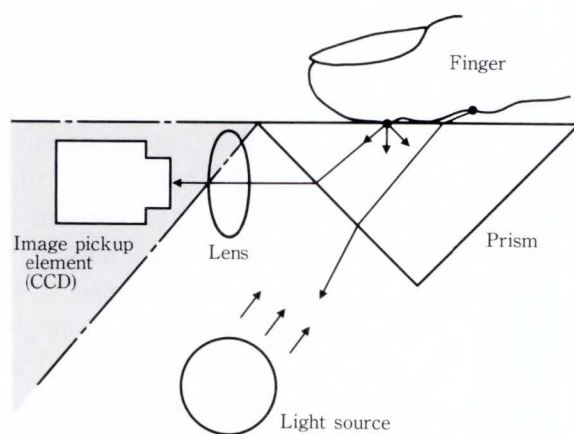


Fig. 2—Principle of prism fingerprint sensor-2.

in the glass from the fingerprint's grooves and ridges. Because of the thin layer of air between fingerprint grooves and the glass, the reflected light enters the glass from the air layer and then exits the other side at the angle of incidence. This reflected light enters the glass at different angles depending on how the fingerprint ridges touch the glass. Light entering at an angle of incidence below the critical angle is reflected repeatedly within the glass (total internal reflection) and propagates through the glass plate. Other light exits the glass in the same way as light scattered from a grooved surface. The repeatedly reflected light carrying the image of the fingerprint ridges exits the glass at the hologram. The external image-forming optical system then forms an image of the ridges.

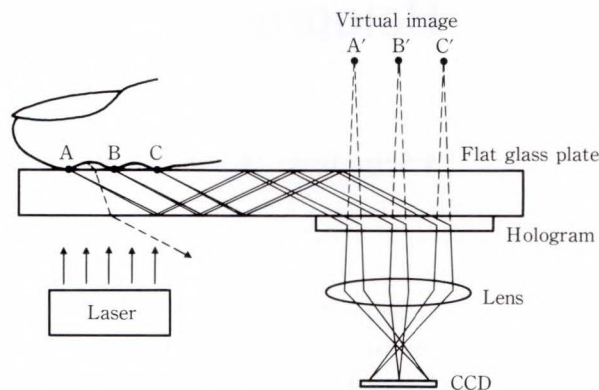


Fig. 3—Principle of holographic fingerprint sensor.

The parallel-plate of the holographic sensor equalize, all optical paths from the fingerprint to the hologram and eliminates trapezoidal distortion.

4. Designing the sensor optical system

4.1 Hologram design

Designing the hologram for the sensor presented some challenges. First, the incline angle of the hologram grating had to be large enough to bend and efficiently direct into the air the light coming through the flat glass plate. This angle had to be greater than the critical angle during reconstruction. In construction, one of the two construction waves of the hologram had to meet the conditions for total internal reflection. However, light could not enter from the air, and the hologram could not be created by interference. A hologram exposure method had to be developed that was free of these problems.

We used two-light flux interference exposure and plane waves (see Figs. 4 and 5).

The following symbols are used in this discussion:

- θ_1, θ_2 : Angle of incidence for hologram construction
- θ_3 : Angle of incidence for hologram reconstruction
- θ_4 : Outgoing angle for hologram reconstruction.

If the angle of incidence at the glass surface is θ_{3g} , the scattered light from a fingerprint ridge with upheaval image information will

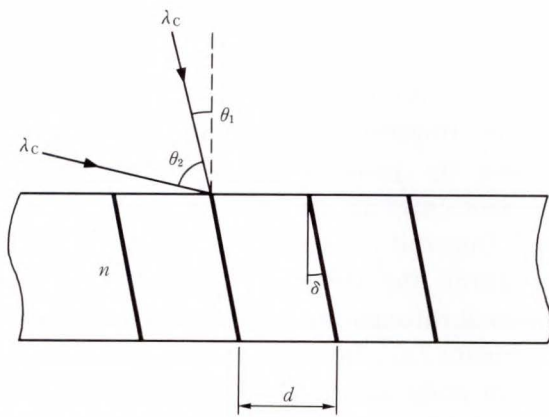


Fig. 4—Angle of incidence for hologram construction.

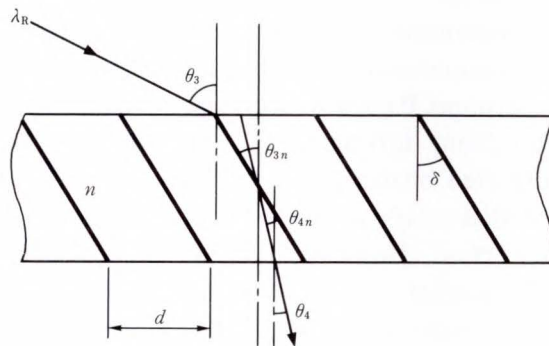


Fig. 5—Hologram reconstruction.

cause total internal reflection at the glass surface of the sensor if the following condition is satisfied:

$$\theta_{3g} > 42^\circ. \quad \dots\dots\dots (1)$$

Taking the mechanical margin into account, we set the angle of incidence for the prototype sensor to:

$$\theta_{3g} = 45^\circ. \quad \dots\dots\dots (2)$$

θ_4 for directing scattered light from the glass to the air is 0 degrees because the external image-forming optical system is inlined. That is:

$$\theta_{3g} = 45^\circ, \quad \theta_4 = 0^\circ. \quad \dots\dots\dots (3)$$

When a hologram meeting the above condition is created, interference cannot be used for its construction.

This is because one of the construction waves must enable conditions for total internal reflection in the glass but no light can enter from the air. Adding a trapezoidal prism to holo-

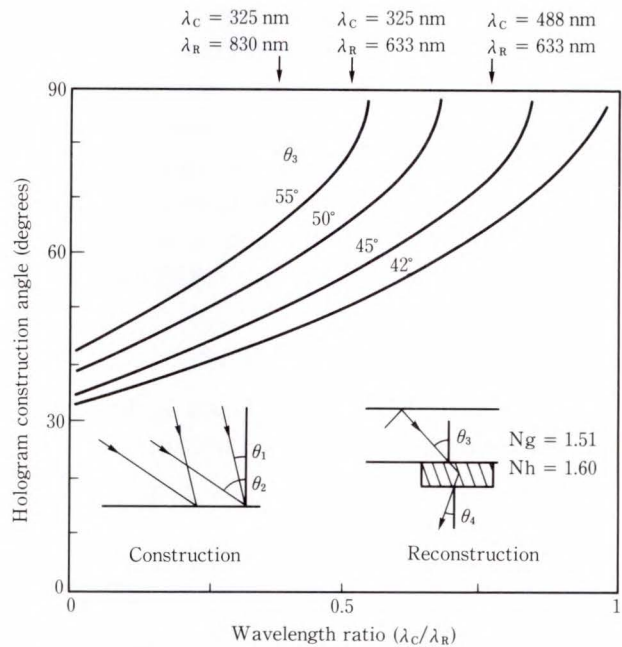


Fig. 6—Relationship between hologram construction angle and wavelength ratio.

gram materials may enable light to enter at an angled surface, but this is hard to achieve.

Therefore, we used light with a wavelength that was λ_c shorter than λ_R for reconstruction as the light source to construct the hologram. This results in a grating inclination angle of δ and a spatial frequency f that meets the conditions for efficient light entry into the air at the critical angle (or wider angle). This enables standard two-light flux interference exposure.

Figure 6 shows the relationship between the angle of incidence for construction and the wavelength ratio. The Y-axis indicates the angle of incidence, θ_1 or θ_2 , whichever is larger.

The parameter is the propagation angle, θ_{3g} , of the light that passes through the glass because of total internal reflection in reconstruction. The reconstruction and construction wavelength ratio λ_c/λ_R cannot be made continuous as shown by the arrows in Fig. 6 because the laser wavelength is discrete. If the θ_2 value is too large, hologram exposure optics cannot be implemented, so the value must be as small as possible. Construction wavelength λ_c was made shorter than reconstruction wavelength λ_R to reduce the θ_2 value to less than 90 degrees and to enable light to enter from the air. As θ_{3g}

approaches the critical angle, the θ_2 value becomes small and hologram construction becomes easy. θ_2 also decreases if the construction/reconstruction wavelength ratio λ_C/λ_R decreases. Because the prototype fingerprint sensor uses a He-Cd laser ($\lambda_C = 442 \text{ nm}$) for hologram exposure and a semiconductor laser for reconstruction ($\lambda_R = 830 \text{ nm}$), θ_1 and θ_2 were set as follows:

$$\theta_1 = 14.1^\circ, \theta_2 = 54.3^\circ. \dots (4)$$

The spatial frequency f and incline angle δ of the hologram grating then become:

$$f = 1286 \text{ lines/mm}, \delta = 21.0^\circ. \dots (5)$$

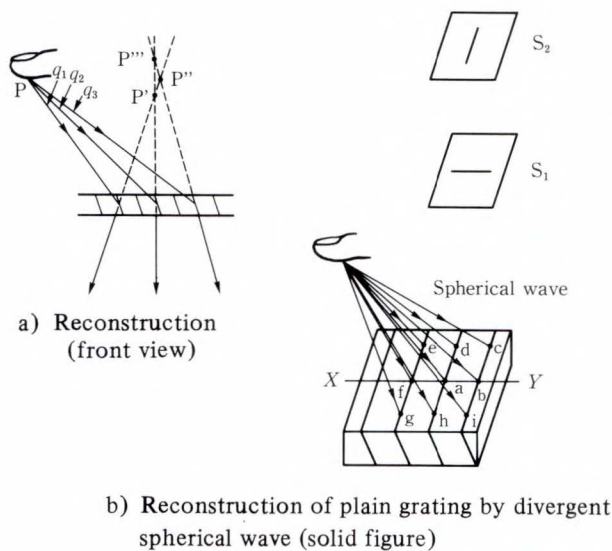


Fig. 7—Cause of astigmatism.

4.2 Designing the image-forming optical system

4.2.1 Astigmatism

As mentioned in section 4.1, the hologram for the fingerprint sensor uses a plane grating created by plane wave interference. Because the light entering the hologram from each point on a fingerprint ridge has a divergent spherical waveform, the virtual image of the fingerprint observed through the hologram has astigmatism.

Figure 7a) shows how astigmatism occurs. At any point on the hologram {Fig. 7b), points a to i}, reconstructed waves do not have the same wavefront as constructed ones. This is because divergent spherical waves scattered by fingerprint ridges are used in reconstruction. The reconstructed wave entering the hologram from point P goes to the image pickup element after being diffracted by the hologram. When diffracted beams $q_1, q_2,$ and q_3 are extended, a virtual image of point P should appear where they cross. However, because the constructed and reconstructed waveforms differ, the three beams cross at points P', P'', and P''' instead of at a single point {see Fig. 7a)}. Because many light paths contribute to the formation of a virtual image, point P on the finger becomes a horizontal stripe (S_1) near the hologram, and becomes a vertical stripe (S_2) at a distance from the hologram {see Fig. 7b)}. Image S_1 is called a vertical virtual image because it is vertically focused. Image S_2 is called a horizontal virtual image because it is horizontally focused.

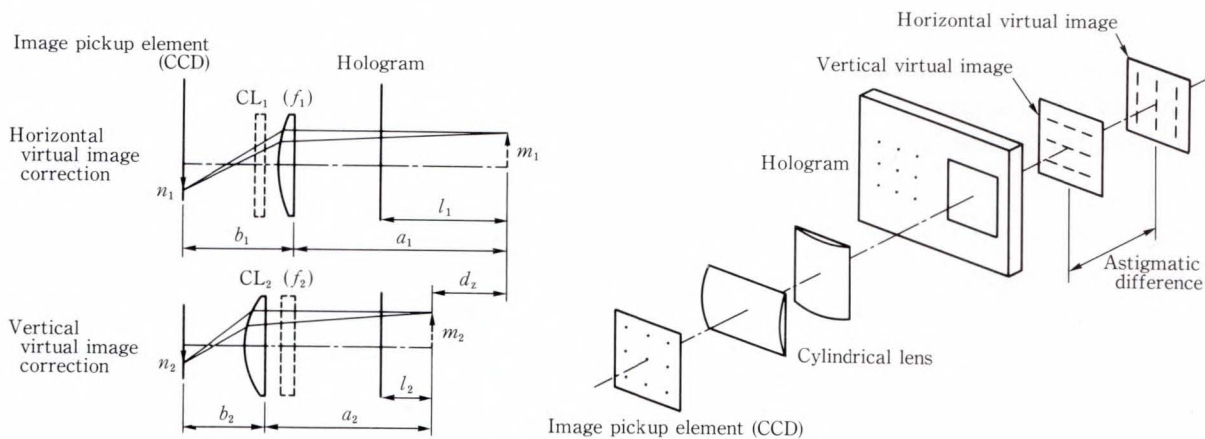


Fig. 8—Astigmatism correction using orthogonal cylindrical lenses.

4.2.2 Orthogonal cylindrical lens

The vertical and horizontal images are best formed independently on the image-forming surface. That is, the lens for vertical images should only contribute to forming vertical images and the lens for horizontal images should only contribute to forming horizontal images. A cylindrical lens is the most suitable for such unidirectional focusing. If two cylindrical lenses are positioned orthogonally, the images can be formed independently (see Fig. 8). Cylindrical lenses CL₁ and CL₂ with focusing distances f_1 and f_2 are used to form the horizontal and vertical image components. If the distances from the image-forming surface to the lenses are a_1 and a_2 and the distances from the lenses to the horizontal and vertical images are b_1 and b_2 , the expression below can be derived from the following lens formula:

$$\frac{1}{a_1} + \frac{1}{b_1} = \frac{1}{f_1}, \quad \frac{1}{a_2} + \frac{1}{b_2} = \frac{1}{f_2}. \quad \dots (6)$$

Because images are formed on the same image-forming surface, the following expression is true when the astigmatic difference is d_z , where

$$d_z = (a_1 + b_1) - (a_2 + b_2). \quad \dots (7)$$

The three expressions below must be satisfied in image formation. If the magnification rates of the horizontal and vertical images are m_1 and m_2 , the following expressions are true:

$$m_1 = \frac{b_1}{a_1}, \quad m_2 = \frac{b_2}{a_2}. \quad \dots (8)$$

a_1 , a_2 , b_1 , and b_2 are deleted from the expressions as follows:

$$d_z = \frac{f_1 \cdot (m_1 + 1)}{m_1} - \frac{f_2 \cdot (m_2 + 1)}{m_2}. \quad (9)$$

The astigmatic difference, d_z , can be calculated if the distance (optical path length of scattered light) from the finger to the hologram is determined. The magnification rates of the horizontal and vertical images should therefore be set to the desired values to determine the combination of f_1 and f_2 .

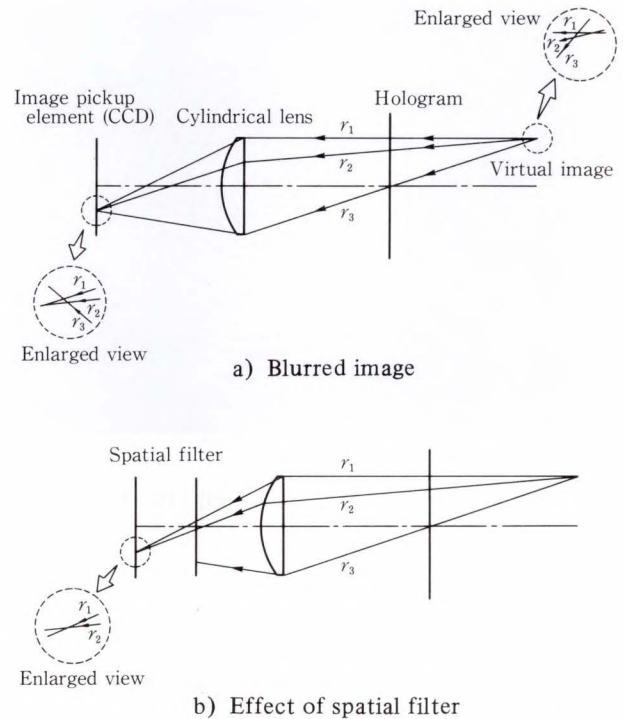


Fig. 9—Improved resolution using spatial filter

So far, only the perpendicular outgoing light from the hologram has been discussed. However, light exiting askew and entering the lens off-axis contributes to form imaging and blurs the image on the image-forming surface {see Fig. 9a}. To simplify this, only one of the two orthogonal image-forming lenses is shown. Of the light forming a virtual image, all rays (r_1 , r_2 , and r_3) that pass through the lens contribute to image formation. A new technique is needed to form the entire input pattern clearly on the image-forming surface.

We developed an optical system with a slit spatial filter at the focusing position of the lens, {see Fig. 9b}. This filter is positioned so that it enables light from r_1 to r_2 to form an image and eliminates light from r_2 to r_3 , thus improving resolution. In addition, because all incident light perpendicular to the lens passes the focus point, a spatial filter at this position functions effectively over the entire input area.

Creating an isotropic image in image memory is important for enlarging the identification logical margin so that the fingerprint

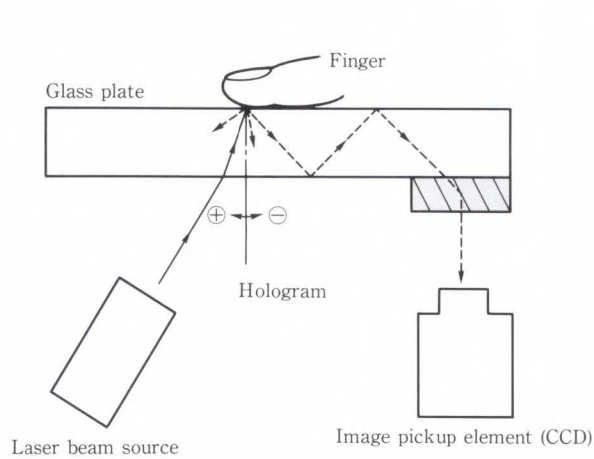


a) Touching

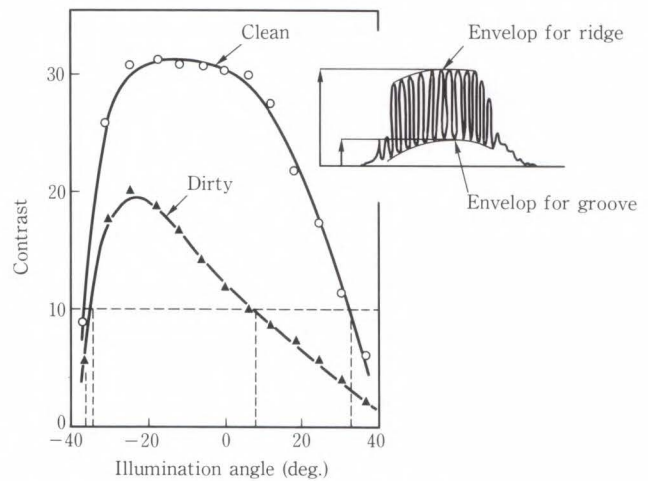


b) Removed

Fig. 10—Examples of detected fingerprint images.



a) Experimental system



b) Experiment data

Fig. 11—Relationship between contrast and lighting angle from inside flat glass plate.

can be identified if the finger is turned. In general, the cell spacing of the image pickup element (CCD) is not isotropic. Therefore it is hard to form an isotropic image in memory, and special software and processing time are needed to correct magnification. Vertical and horizontal magnification rates are controlled independently and optical super-parallel operations in holographic sensor optics can quickly and easily produce an isotropic image in memory.

4.3 Optimizing the lighting angle

As mentioned in Chapter 3, the sensor only detects an image formed by scattered light

beams from fingerprint ridges. If the input surface is blurred by sweat or grease, light may be reflected and superimposed on the grooves (see Fig. 10). The influence of these latent fingerprints must be eliminated.

Figure 11 shows the relationship between sensor output contrast and the angle of lighting from inside the flat glass plate. Sensor output contrast is defined by the ratio of ridge signal levels to groove signal levels. The lighting angle is plus if it is not on the hologram side of the finger and minus if it is on the hologram side of the finger. The input surface is rated clean immediately after being wiped with isoprophyl alcohol (IPA) and is rated dirty after being

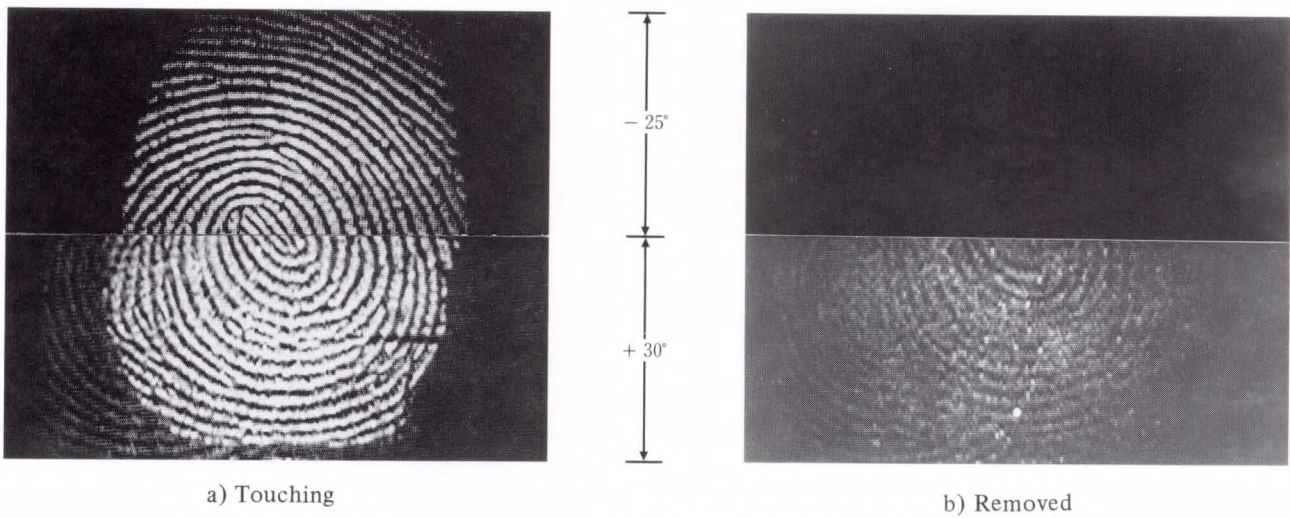


Fig. 12—Eliminating the influence of latent fingerprints by optimizing the lighting angle.

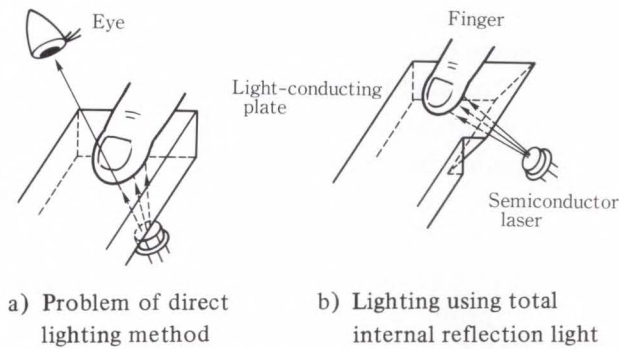


Fig. 13—Ridge selective lighting.

touched by fingers a few times. When the surface was clean, the contrast was almost stable at a lighting angle from -25 degrees to $+7$ degrees. When the lighting angle was under -25 degrees or over $+7$ degrees, the contrast deteriorated. This deterioration was probably caused because the light intensity per unit area and the intensity of light that could become internal reflected light from scattered information decreased.

When a fingerprint was entered through a surface blurred with latent fingerprints, the contrast was low at all lighting angles. This was especially so on the plus side. If the contrast is sufficient even when the input surface is blurred (i.e. 10 or more), the lighting angle from inside the glass can be set within the range from -33 degrees to $+7$ degrees.

Figure 12 compares fingerprint images ob-

tained at lighting angles of -25 degrees and $+30$ degrees. The image was greatly affected by latent fingerprints when the angle was $+30$ degrees. However, only the current fingerprint appeared when the angle was -25 degrees.

5. Problems and techniques

5.1 Selective ridge lighting

This holographic fingerprint sensor uses light efficiently because the transparent flat glass plate is lit from directly underneath. This has the disadvantage of light leaking from the fingerprint input port { see Fig. 13a)}. The amount of leakage light is about four times larger than that allowed by laser safety standards. A contact detection mechanism could be installed at the fingerprint input port and the light switched off when not in use. But light would still leak from the sides of the finger when in use. Covering the fingerprint input port would make it uncomfortable to use. To protect the user's eye from the laser beam, the fingerprint sensor must prevent light leaking from the fingerprint input port.

To solve this problem, we developed a ridge-selective lighting system { see Fig. 13b)}. Instead of lighting the transparent flat glass plate from directly underneath, we used a transparent plane plate with a diagonally cut edge through which the light is irradiated.

Figure 14 shows the light leakage at differ-

ent angles. (For the “Clean” result, the glass surface was cleaned with isopropyl alcohol.) The leakage ratio decreases rapidly as the angle of incidence exceeds the critical angle. This is especially true for a clean surface but, even if the surface is dirty, the leakage ratio is only about 9×10^{-3} at 50 degrees of incidence.

The maximum permissible exposure calculated based on IEC Class 1 laser safety standards is 0.18 mW for 830 nm. We use a 25-mW laser diode to obtain a high contrast image. At an angle of incidence of 0 degrees, 0.7 mW would

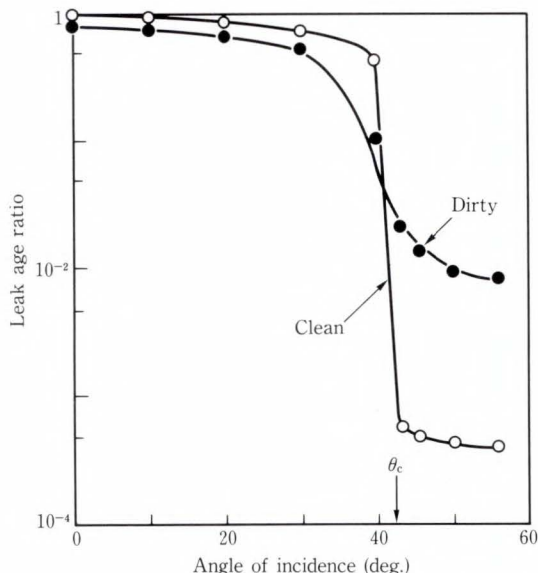
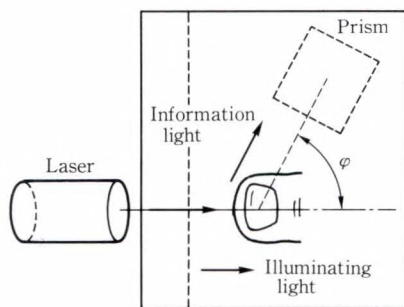


Fig. 14—Leakage ratio as a function of angle of incidence.



reach an operator’s eyes. In our system, a maximum of 0.08 mW reaches the operator’s eye, even when the plate is dirty. This more than satisfies the IEC standards.

5.2 Spatial separation of illuminating light and information light

If the ridge-selective lighting is adopted for safe use of the laser, the lighting angle within the plane perpendicular to the fingerprint input port cannot be optimized as explained in section 4.3.

If the hologram is positioned in a positive reflecting direction from the lighting, a high output will be produced but the scattered beams from latent fingerprints will adversely affect the signal-to-noise ratio. We tried improving the signal-to-noise ratio by: optimizing the detection angle between the light irradiated onto the surface parallel to the fingerprint input surface, and by optimizing the direction in which ridge information light propagates.

Figure 15 shows our experiment and its results. To simplify the experiment, a He-Ne laser ($\lambda = 633 \text{ nm}$) beam was used for lighting and a prism was used to pick up the light reflected from the finger. To check the relationship between the signal-to-noise ratio and detection angle, the signal-to-noise ratio was defined from: ① the output level S of the scattered light

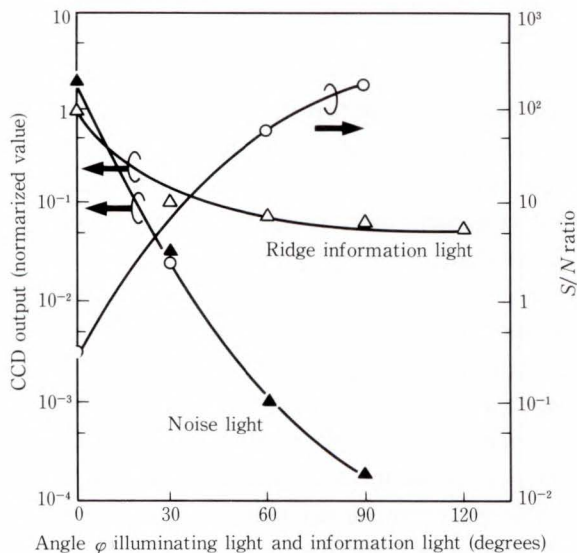


Fig. 15—Relationship between information light S/N ratio and crossing angle of illuminating and information light.

(information light) from fingerprint ridges when a finger was placed on the input surface, and ② from the output level N of the scattered light (noise light) from latent fingerprints with no finger on the input surface. Output level S of ridge information light decreased as detection angle φ increased. However, the signal-to-noise ratio improved because output level N of the scattered light from latent fingerprints decreased faster. The signal-to-noise ratio exceeded 100 when the detection angle was 90 degrees. This means that the influence of latent fingerprints can be ignored. When the detection angle was increased to 120 degrees, output level S of the ridge information light changed little, but output level N of the scattered light from latent fingerprints decreased to almost unmeasurable

levels. We finally set the detection angle at 90 degrees to simplify the design and manufacture of the flat glass plate and other mechanical components. At this angle, output level S of the information light from ridges is almost one-tenth that of the regular reflection component. However, this does not cause a problem if the light intensity is correct and optical components use the light efficiently.

5.3 Prototype fingerprint sensor

To verify the effectiveness of the optics explained above, we made a prototype fingerprint sensor (see Fig. 16). It is $230 \times 100 \times 70$ (mm). Figure 17 is an example of these optics using the holographic fingerprint sensor.

Figure 18 shows an example of a detected fingerprint image. A high-resolution image was produced only when a finger was placed on the

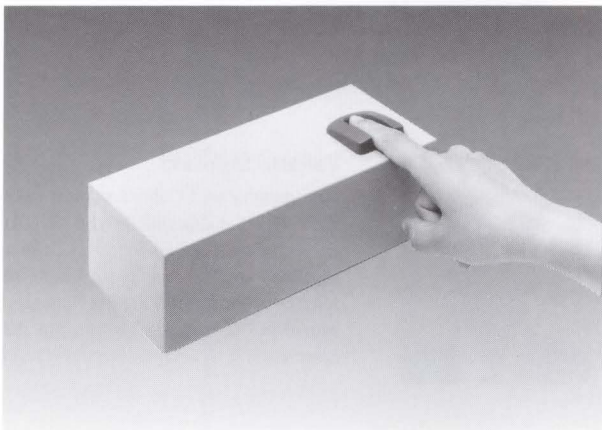


Fig. 16—Prototype fingerprint sensor.

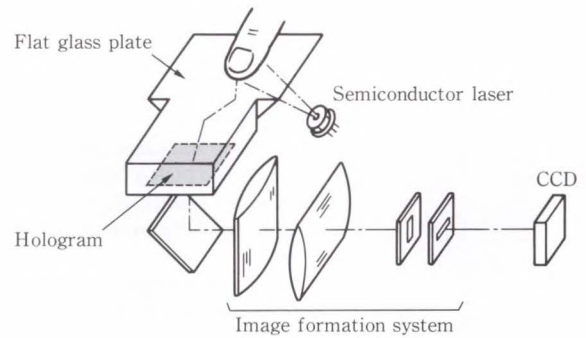
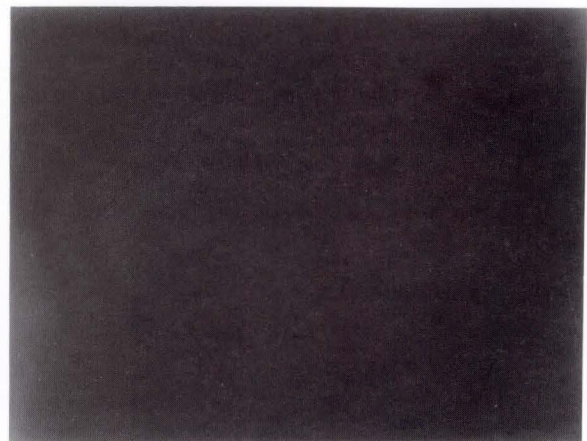


Fig. 17—Practical optical system of holographic fingerprint sensor.



a) Touching



b) Removed

Fig. 18—Examples of detected fingerprint images.

fingerprint input port. The scattered black spots in the white ridge lines are sweat glands, proving the sensor's high-resolution.

6. Conclusion

To solve the problem of trapezoidal distortion in conventional real-time fingerprint sensors for personnel identification, we developed a holographic fingerprint sensor consisting of a hologram and a flat glass plate. It uses a parallel-plane plate, so that the distance from each point on the fingerprint to the hologram element is equal and a distortion-free fingerprint image can be obtained. We also developed the hologram and flat glass plate for the sensor and external optics to correct astigmatism caused by the hologram. To make the sensor safe, we introduced ridge-selective lighting, which prevents laser light from leaking from the fingerprint

input port and possibly damaging the user's eyes.

If image forming can be integrated into a hologram several micrometers thick together with image pickup, no external optics will be needed, and the system can be made even more compact.

Our next job is to develop a self-image-forming hologram.

References

- 1) Kawagoe, M., and Tojo, A.: Fingerprint Pattern Classification. *Pattern Recognition*, **17**, 3, pp. 295-303 (1984).
- 2) Shimizu, A., and Hase, M.: Entry Method of Fingerprint Image Using Prism. (in Japanese), *Trans IECE, Jpn.*, **J67-D**, 5, pp. 627-628 (1984).
- 3) Igaki, S., Eguchi, S., Ikeda, H., and Inagaki, T.: Realtime Fingerprint Sensor Using a Hologram. Digest Tech. Papers, 1985 Annual Meet., OSA, Washington, DC, p. 78.



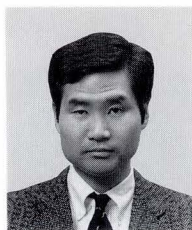
Seigo Igaki

Holography and Color-Imaging Laboratory
FUJITSU LABORATORIES, ATSUGI
Bachelor of Electronics Eng.
University of Electro-Communications
1973
Master of Electronics Eng.
Graduate School of Hokkaido University
1975
Specializing in Personal Identification
System



Takashi Shinzaki

Holography and Color-Imaging Laboratory
FUJITSU LABORATORIES, ATSUGI
Bachelor of Applied Material Science
Muroran Institute of Technology 1986
Master of Applied Material Science
Muroran Institute of Technology 1988
Specializing in Optical System Design



Shin Eguchi

Holography and Color-Imaging Laboratory
FUJITSU LABORATORIES, ATSUGI
Bachelor of Electrical Eng.
Keio University 1982
Master of Electrical Eng.
Keio University 1984
Specializing in Holography

Wavelength Independent Grating Lens System

• Masayuki Kato • Satoshi Maeda • Fumio Yamagishi

(Manuscript received November 7, 1989)

Grating lenses can be made small and light, and can be mass-produced. However, wavelength variations in the light source cause aberrations and change the focal length of the grating lens. Therefore, it has been difficult to use grating lenses in high-precision optical systems that use light sources with wavelength variation. A new grating lens system with a high numerical aperture was proposed to suppress the aberration and keep the focal length constant over a wavelength range of a few tens of nanometers. Aberration calculations showed that the acceptable wavelength range was ± 15 nm for a system with a numerical aperture of 0.50. The gratings were made using electron beam lithography, and their focusing ability was then evaluated.

1. Introduction

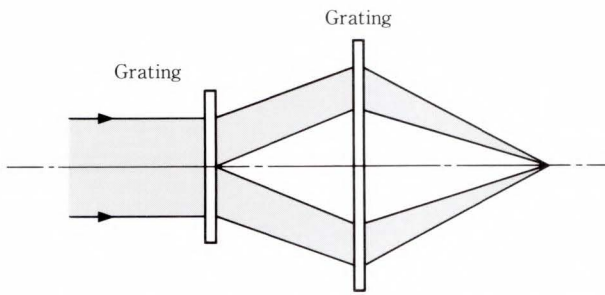
Because grating lenses can be made small and light and are easily mass-produced, various applications such as laser scanner lenses^{1), 2)}, diode laser lenses³⁾, and slide projector lenses⁴⁾ have been proposed. A diffraction lens can provide an arbitrarily designed wavelength, wavefront, and angle of incidence. However, if the reconstruction wavelength changes, this will cause aberrations in the reconstructed wave. Refractive optics generally have chromatic aberrations because refractive indexes have wavelength dispersion. However, the aberration caused by wavelength variation in a diffraction lens is much larger than that of a refractive lens. Therefore, if a diode laser is used to provide monochromatic light, the wavelength is not stable because of mode-hopping. Also, if a light source with a wide bandwidth is used, the beam cannot be precisely focused to a diffraction-limited spot using a conventional grating lens. If a grating lens has a large numerical aperture, the aberration will be severe.

Considerable research has been done on compensation for chromatic aberration of diffraction lenses, but no effective way of designing precise focusing grating lenses has been suggested. Weingärtner proposed an achromatic grating lens system consisting of two holographic elements⁵⁾. However, it is not suitable for precise beam focusing because there is no light in the paraxial region. A grating lens system that has compensation for chromatic aberration and a high numerical aperture has been designed. This system has about the same focusing ability as conventional aberration free lenses and was made using electron beam lithography. The results were satisfactory.

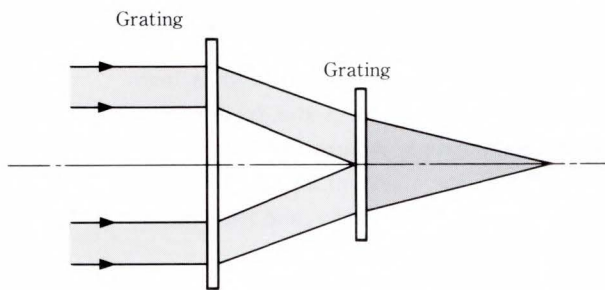
2. Grating lens structure

The grating lens systems of Weingärtner are shown in Fig. 1. Diffraction limited focusing of conventional lenses cannot be obtained with the structure shown in Fig. 1 a) because there is no light in the paraxial region. The structure in Fig. 1 b) is not suitable for use with a light

This paper is a reprint of the article published in *Appl. Opt.*, **28**, 4, pp. 682-686 (1989), entitled Wavelength independent grating lens system.



a) Two gratings with no light in the paraxial region of the converging beam



b) Two gratings in which the light in the paraxial region of the reconstruction beam does not contribute to beam focusing

Fig. 1—Achromatic grating lens systems proposed by Weingärtner⁵⁾.

source with a Gaussian power distribution because the light in the paraxial region is not used and therefore the efficiency is low.

The new grating lens system has two grating elements and because of its aberration compensation has almost no chromatic aberration over a wavelength range of a few tens of nanometers (See Fig. 2). In this lens system, diffraction angle variations due to wavelength changes are compensated by the second grating. Therefore, all rays converge on a focal point. A grating lens system that focuses a diverging spherical wave to a fine point requires a carefully designed lens structure.

Design of a grating lens can be started by assuming an in-line lens structure (See Fig. 3). The path between GL₁ and GL₂ is important. One solution is to cross rays between the gratings. Figure 4 shows how to determine the rays' paths.

Suppose a ray of wavelength λ_1 leaves from point O (a point source) and reaches point R₁

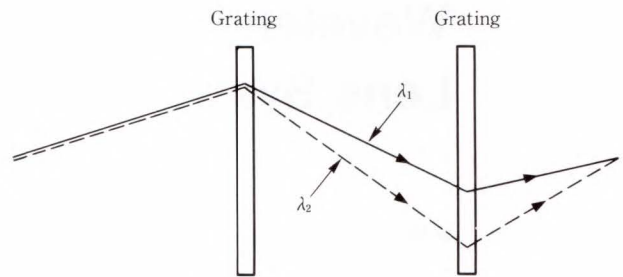


Fig. 2—Chromatic aberration compensation.

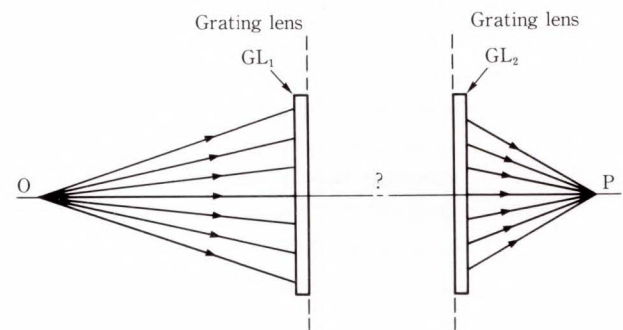


Fig. 3—In-line two grating lens system. To compensate aberration, the paths of rays between gratings GL₁ and GL₂ must be determined.

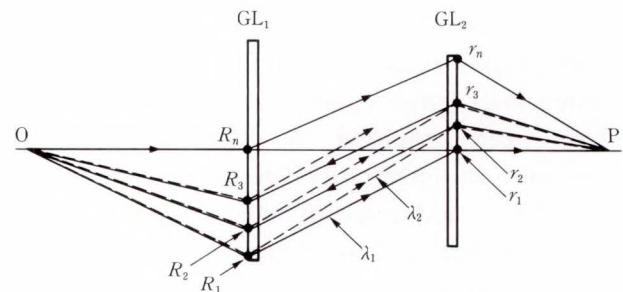


Fig. 4—Designing the spatial frequency distributions in radial directions of GL₁ and GL₂. λ_1 and λ_2 ($\lambda_1 < \lambda_2$) are design wavelengths, O is a point source, and P is the focal point.

on GL₁. The ray is diffracted toward r_1 , (the center of GL₂) and then diffracted again by GL₂. It then propagates along the axis of the grating system (O-P). Spatial frequencies F_1 and f_1 at points R₁ and r_1 can be calculated from the angles of incidence and the diffraction angles at the points. The wavelength then shifts to λ_2 ($\lambda_2 > \lambda_1$). Because the wavelength is longer, the diffraction angle at R₁ becomes larger, and the diffracted ray reaches point r_2 on GL₂. By assuming the diffracted ray at r_2

converges on point P on the axis, the spatial frequency f_2 at r_2 can be calculated. By returning the wavelength to λ_1 , it is possible to find point R_2 on GL_1 and the spatial frequency F_2 at the point by back-tracing the ray from P to O. Then, the location of point r_3 and spatial frequency f_3 at r_3 can be calculated by tracing the ray from O to P for wavelength λ_2 . Finally R_3 at GL_1 can be found by returning the wavelength to λ_1 and back-tracing the ray. The radial spatial frequency distributions of the gratings are determined by repeating the above procedure until R_n reaches the center of GL_1 . R_1 and r_n are the radii of GL_1 and GL_2 respectively. An aberration-free in-line grating

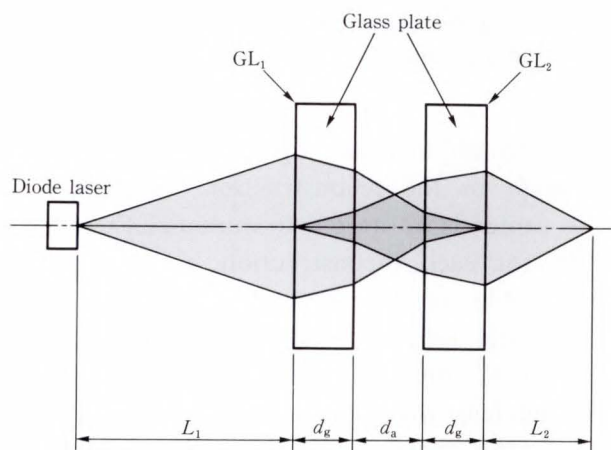


Fig. 5—The grating lens system and its parameters. The parameters are listed in Table 1.

lens system for a wavelength of λ_1 and λ_2 is obtained by rotating the structure in Fig. 4 around the axis.

Figure 5 shows the basic parameters of this grating lens system. It consists of two glass plates with gratings on the outer side of the plates. Table 1 lists the parameters used in calculations and experiments. The typical wavelength of the light source was chosen to be 830.0 nm. Design wavelengths λ_1 and λ_2 can be chosen arbitrarily, but should not be too different from the typical wavelength. To determine the spatial frequency distribution of GL_1

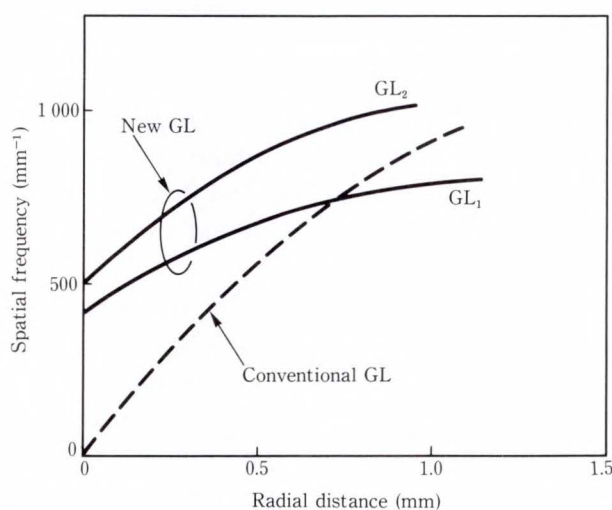


Fig. 6—Spatial frequency distributions of the grating lenses (GL_1 , GL_2) and a conventional in-line type grating lens.

Table 1. Parameters of the grating lens system

Parameter		Notation	Value
Initial	Wavelength	Typical	λ_0 830.0 nm
		Design	λ_1 830.0 nm
	λ_2 830.3 nm		
	Focal length	GL_1	L_1 3.75 mm
		GL_2	L_2 1.70 mm
	Substrate	Thickness	d_g 1.00 mm
Refractive index		n 1.51	
Distance between substrates		d_a 1.25 mm	
Dependent	Numerical Aperture	GL_1	NA_1 0.3
		GL_2	NA_2 0.5
	Spatial frequency range	GL_1	F 434–872/mm
		GL_2	f 512–1 047/mm

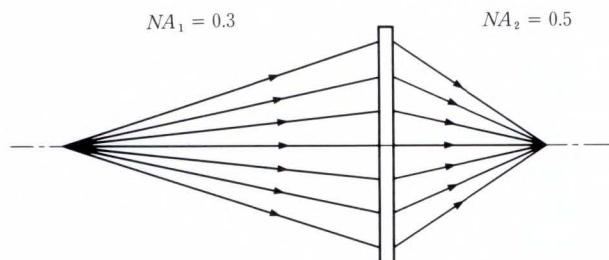


Fig. 7—Conventional in-line grating lens with numerical apertures of 0.3 and 0.5.

and GL_2 , the initial parameters must be set. The diameter of GL_1 can be calculated from NA_1 and L_1 (the numerical aperture and focal length of GL_1). NA_2 (the numerical aperture of GL_2) is determined from the spatial frequency distributions. The designated NA_2 can be obtained by optimizing d_a (the distance between the two substrates). The numerical aperture of the gratings was set to 0.3 and 0.5. The spatial frequencies in Table 1 represent the minimum and maximum values.

Figure 6 shows the spatial frequency distribution for GL_1 and GL_2 . The spatial frequencies at the center of the concentric gratings have the minimum non-zero values, and are maximum at the peripheries. Figure 6 also shows the curve for the conventional in-line type grating lens shown in Fig. 7. The spatial frequency increases with the radius as it does in GL_1 and GL_2 , but the minimum spatial frequency is zero in the conventional grating.

3. Performance of a chromatic aberration compensated grating lens system

To find the wavelength bandwidth over which the aberration is negligible, the wavefront aberration of the grating lens system was calculated using reconstruction wavelengths which were different from λ_1 or λ_2 .

Figure 8 shows the calculated rms wavefront aberration for two examples designed using two pairs of wavelength:

- 1) $\lambda_1 = 825.0$ nm, $\lambda_2 = 835.0$ nm, and
- 2) $\lambda_1 = 830.0$ nm, $\lambda_2 = 830.3$ nm.

The center of the reference sphere (or the focal point) used in the calculation of the aberration was held constant. Actually the

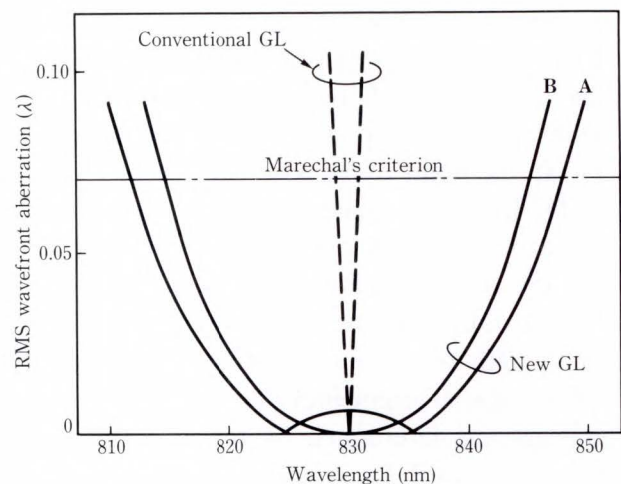


Fig. 8—Calculated rms wavefront aberration.

- A: grating lens system designed using wavelengths of 825.0 nm and 835.0 nm.
 B: grating lens system designed using wavelengths of 830.0 nm and 830.3 nm.

focal length increases by $0.15 \mu\text{m}$ for a 1 nm increase in the reconstruction wavelength. If the center is optimized to minimize the aberration for each reconstruction wavelength, the acceptable wavelength range will become wider. The focal length change ratio in this case is very small compared with that of a conventional grating lens with a ratio of $-6.3 \mu\text{m}/\text{nm}$. The amount of aberration at each design wavelength is zero. In wave A, the rms wavefront aberration has a local maximum between the design wavelengths. In wave B, because the design wavelengths are very close, the curve looks parabolic, but the shape of the curve between λ_1 and λ_2 is like wave A. Marechal's criterion (an rms wavefront aberration below 0.07) was used to define the wavelength bandwidth over which aberration was negligible. The bandwidth was at least ± 18 nm for wave A, and ± 15 nm for wave B. The wavelength tolerance of the conventional grating lens was 830 ± 0.25 nm (Fig. 8). Therefore, the acceptable wavelength range of the aberration compensated grating lens system with the specifications listed in Table 1 is at least sixty times wider than that of the conventional grating lens.

The wavelength bandwidths of grating lens systems with various numerical apertures were

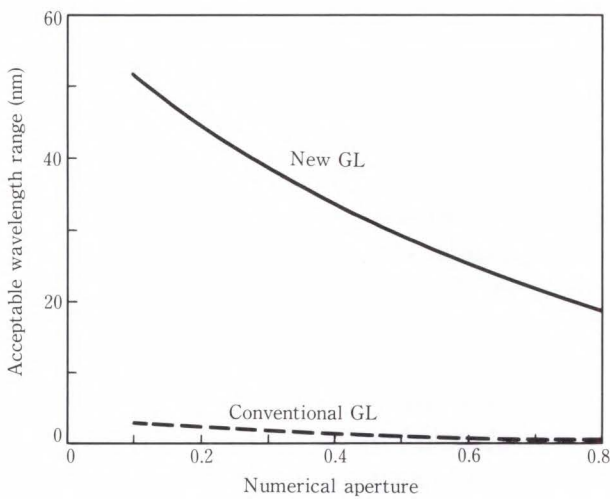
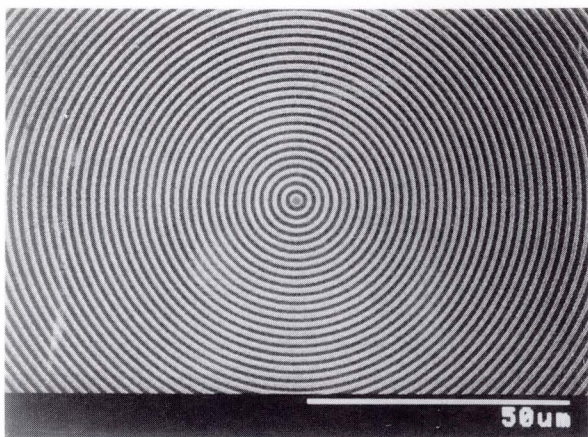
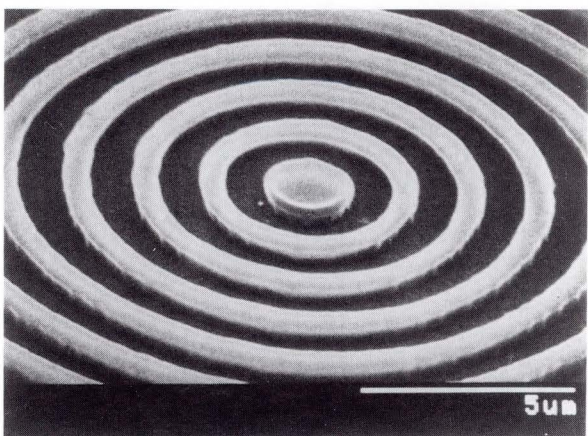


Fig. 9—Acceptable wavelength range as a function of NA_2 (numerical aperture of the second grating, GL_2) with $NA_1 = 0.3$.



a) Top view



b) Oblique view

Fig. 10—Grating lenses made using electron beam lithography (SEM photographs).

calculated by changing NA_2 and by keeping NA_1 constant at 0.3. The grating system was designed for wavelengths of 830.0 nm and 830.3 nm. Figure 9 shows the calculated results. As NA_2 increases, the acceptable wavelength range decreases. The dashed curve shows a conventional grating lens with the same numerical aperture as our grating lens system. The chromatic aberration compensated grating lens system has a much wider bandwidth than the conventional grating lens system.

4. Experiment

A chromatic aberration compensated grating lens system with the specifications listed in Table 1 was made, and its wavelength tolerance was examined. It was difficult to make a concentric circular equiphase pattern with a spatial frequency distribution that gradually increased from the center to the edge by using holographic exposure. This was because of difficulties in using two recording beams with complex wavefronts. Therefore, we used electron beam lithography. Polished optical quality glass (BK7) was used for substrates. A photoresist was spin-coated on the substrates, exposed to an electron beam, and then developed. Figure 10 shows scanning electron microscope photographs of the center of the grating. The concentric fringes are dense near the center, which is quite different from conventional in-line grating lenses.

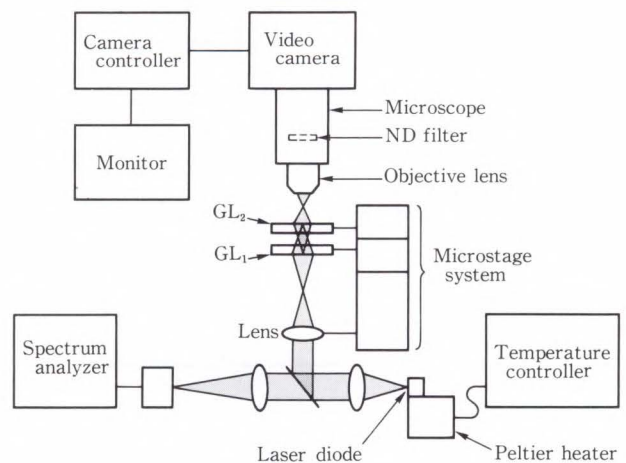


Fig. 11—Focused spot observation apparatus.

The two grating lenses, GL_1 and GL_2 , were coaxially aligned, and their focusing ability was evaluated using a laser diode with a wavelength of 830.5 nm. Figure 11 shows the setup used to measure the focused spot size. A diverging beam from the laser diode is collimated by a high quality lens with a numerical aperture of 0.3 and then divided into two by a beam splitter. The wavelength of the source is obtained by measuring the transmitted beam with a spectrum analyzer. The reflected beam from the beam splitter is focused on a diffraction-limited-size spot by an aberration free lens. The focal point is a 830.5 nm point source. GL_1 , GL_2 , and the point source were aligned by microstages.

The focused beam was observed using a

microscope and a video camera. To vary the wavelength of the laser diode, its temperature was changed by a Peltier heater.

Figure 12 shows photographs of the focused beam spots and laser diode spectra. The photographs in a) show the spot and spectra of a conventional objective lens with a numerical aperture of 0.5. The photographs in b) and c) show those of the chromatic aberration compensated grating lens system. A single wavelength was used in a) and b), and multi-mode light (obtained by modulating the laser diode current by a high frequency signal) was used in c). In a) the diameter of the focused spot was $1.5 \mu\text{m}$ along the major axis, and $1.3 \mu\text{m}$ along the minor axis. In b) and c) the diameter was $1.9 \mu\text{m}$ along the major axis and $1.6 \mu\text{m}$

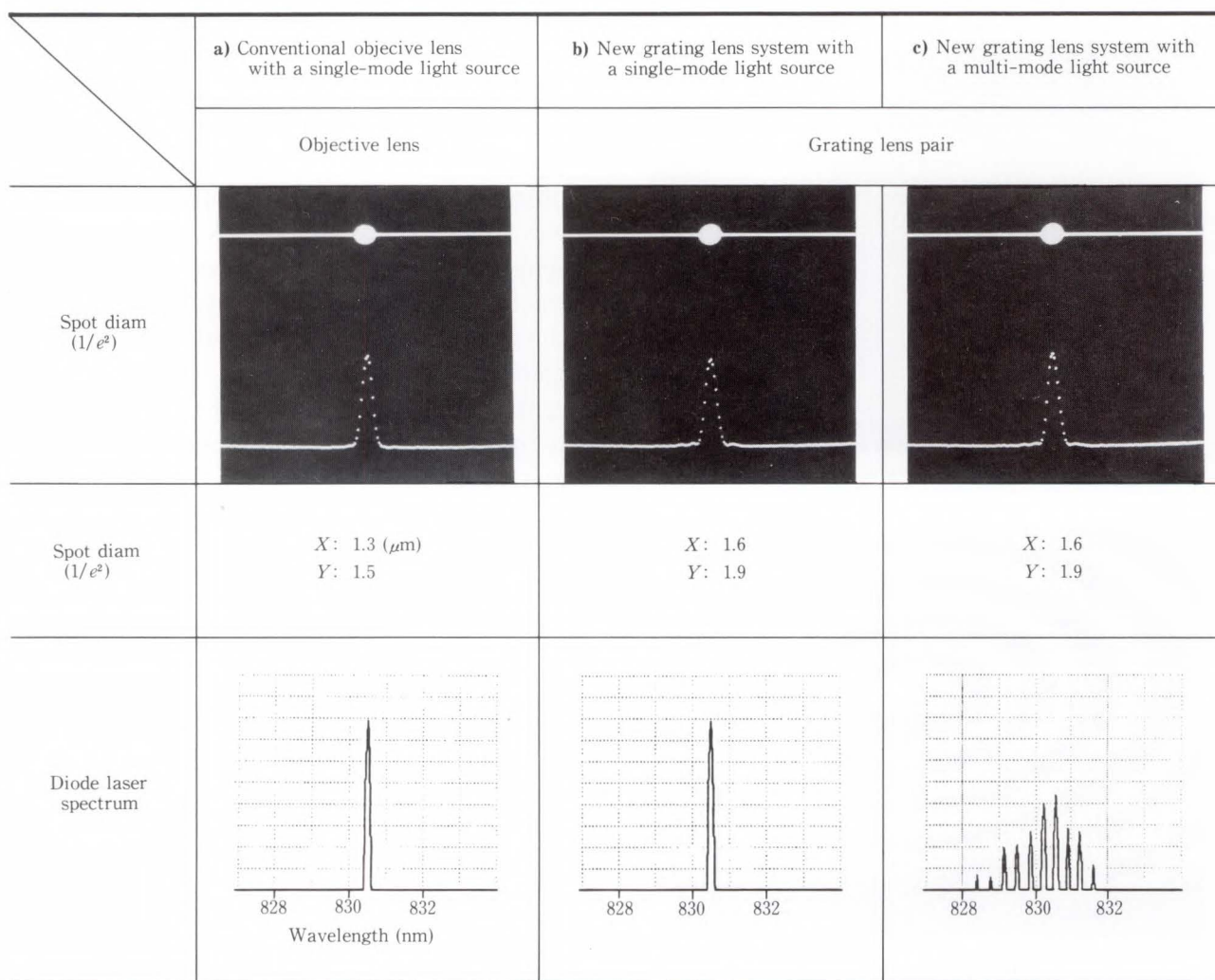


Fig. 12—Focused spot sizes and laser diode spectra.

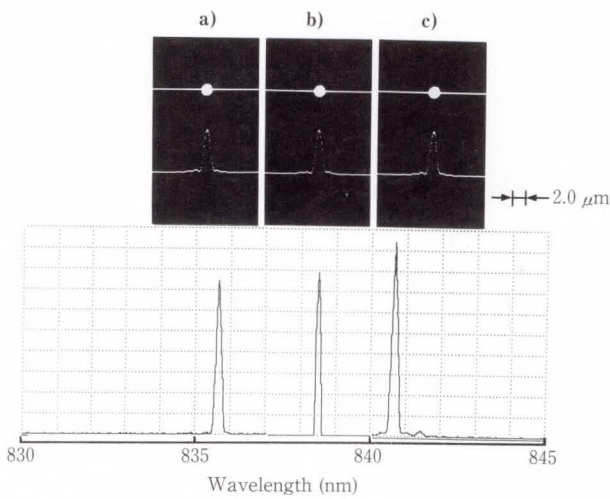


Fig. 13—Beam focusing with single wavelengths of a) 835.7 nm, b) 838.5 nm, and c) 840.7 nm.

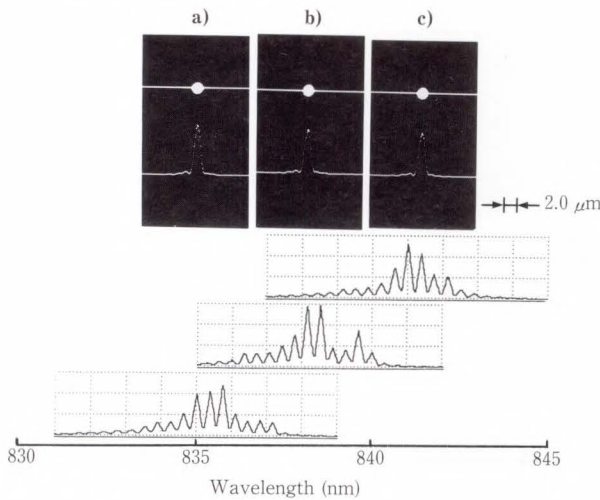


Fig. 14—Beam focusing using a multi-mode laser diode with various center wavelengths.

along the minor axis.

The spots focused by the grating lens system have small sidelobes, but these are only slightly larger than those produced by a conventional optical lens. The spot size is larger because of the light intensity distribution of the beam-crossing lens structure. A comparison between b) and c) shows that the grating lens can focus multi-mode light as well as single-mode light to a diffraction-limited-size spot.

The wavelength of the laser diode was varied to determine the focusing ability of the grating lens system at different wavelengths. Figure 13 shows the focused spots obtained at single wavelength of a) 835.7 nm, b) 838.5 nm,

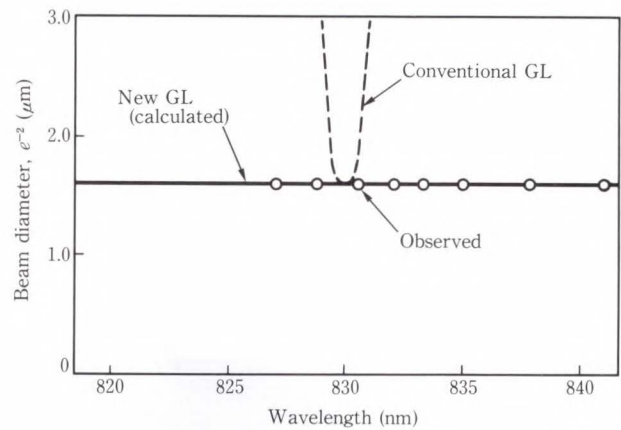


Fig. 15—Chromatic aberration compensation. The solid line shows the calculated beam diameters (minor axis) of the grating lens system. The dashed line shows the calculated beam diameters (minor axis) of a conventional grating lens. The circles are measurements.

and c) 840.7 nm. The diameters of the spots were about equal to the ones shown in Figs. 12b) and c). Multi-mode light with different center wavelengths was then used to evaluate the chromatic aberration compensation. The spectra of multi-mode light had twelve or thirteen modes, and the bandwidth was about 5 nm (see Fig. 14). Again, the diameters of the focused spots were almost the same as those shown in Figs. 12b) and c). Two laser diodes with different typical wavelengths were used to determine the acceptable wavelength range. Figure 15 shows the spot diameter vs. wavelength. The results show that the beam diameters remain constant for wavelengths between 827 nm and 841 nm. In future work, we plan to measure the wavelength dependence at more widely separated wavelengths.

5. Discussion

The spots focused by the conventional optical lens with a 0.5 numerical aperture were 1.5 μm along the major axis and 1.3 μm along the minor axis. The spots formed by the grating lens system were 1.9 μm along the major axis and 1.6 μm along the minor axis. These are slightly larger than those of a conventional lens. These differences are due to the light intensity distribution at the second grating,

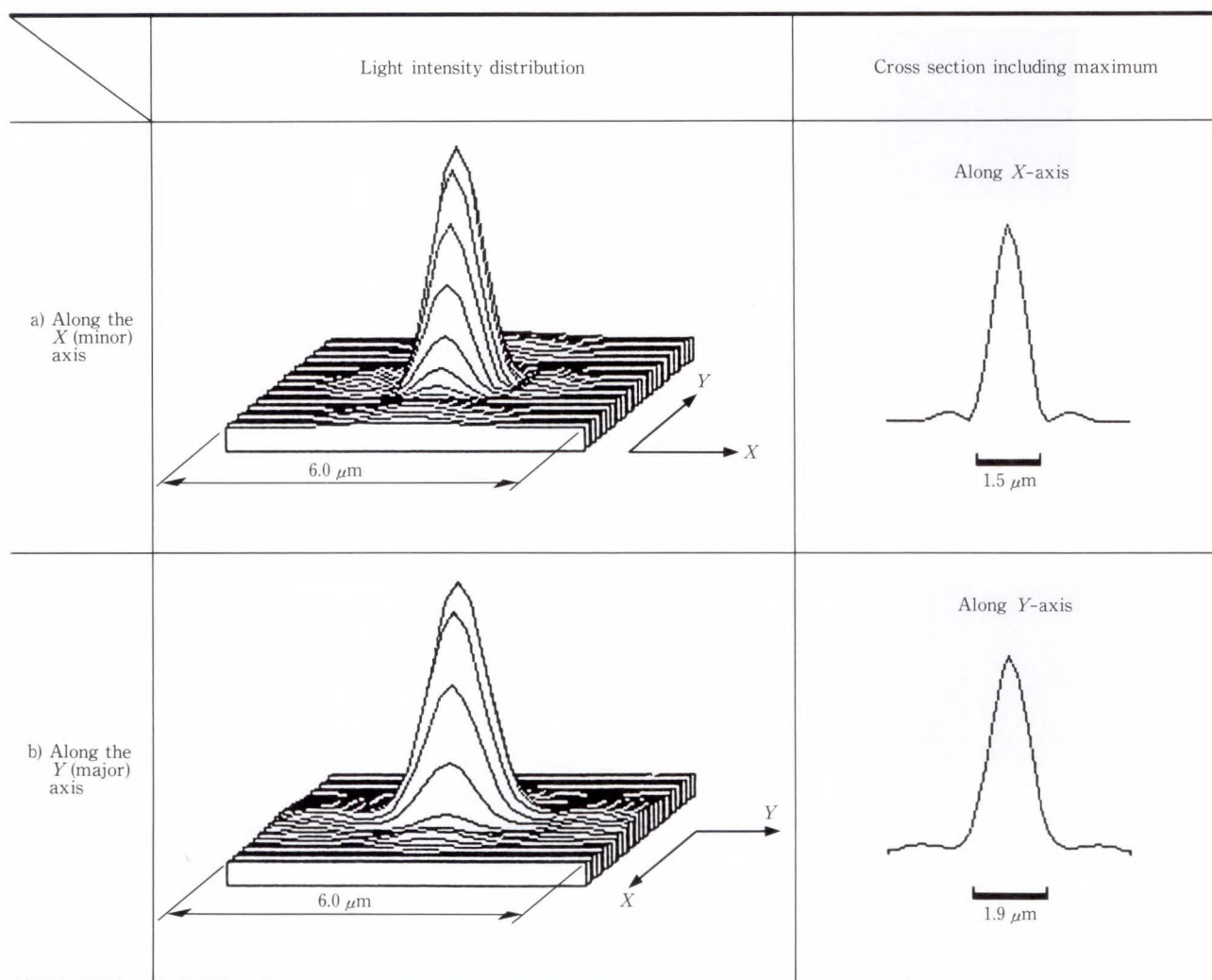


Fig. 16—Calculated light intensity distribution on the focal plane.

GL₂, caused by the beam crossing between GL₁ and GL₂. To check the validity of these results, the intensity distribution of the focused spot was calculated using the method proposed by Nowak and Zajac⁶). The intensity distribution at GL₂ was taken into account. Figure 16 shows the relative intensity distribution on the focal plane. The difference between the diameters measured in the major axis (Y) and minor axis (X) are due to the elliptical intensity distribution of the diverging light emitted from a diode laser. The major and minor axes of the elliptical beam correspond to the minor and major axes of the focused spot. The calculated diameters are very close to the measured values. A more rigorous discussion of the beam focusing performance requires wavefront measurement.

The chromatic aberration compensated grating lenses that were made using electron beam lithography were binary phase gratings (BPGs) with two phase levels. The maximum diffraction efficiency attainable with BPGs is about 41 percent. It is possible to increase the efficiency by increasing the number of phase levels. Micro-stages were used to align the new grating lens system and no special effort was needed for alignment. But it will be necessary to calculate the acceptable alignment error.

6. Conclusion

The design, fabrication, and wavelength tolerance of a chromatic aberration compensated grating lens system have been discussed. Our grating lens system had a wider bandwidth

than conventional inline grating lenses in terms of acceptable wavelength for aberration-free focusing. The focal length did not change with the wavelength of the light source. Calculations showed that a lens system with a 0.5 numerical aperture had a wide bandwidth (30 nm or wider) and that the wavelength tolerance was at least sixty times larger than that of a conventional grating lens.

The grating lens system was made using electron beam lithography. The spot size measurement showed that the chromatic aberration was compensated and that the focal length remained constant when the wavelength (or wavelengths in multi-mode) was varied. We expect this grating lens system to be used with laser diodes and wide wavelength bandwidth sources such as LEDs.

References

- 1) Ikeda, H., Yamazaki, K., Yamagishi, F., Sebata, I., and Inagaki, T.: Shallow-type Truncated Symbol-Reading Point-of-Sale Hologram Scanner. *Appl. Opt.*, **24**, 9, pp. 1366-1370 (1985).
- 2) Hasegawa, S., Yamagishi, F., Ikeda, H., and Inagaki, T.: High resolution Holographic Line Scanner for Use in Diode Laser Printers. *Proc. SPIE*, **747**, pp. 8-16 (1987).
- 3) Hatakoshi, G., and Goto, K.: Grating Lenses for the Semiconductor Laser Wavelength. *Appl. Opt.*, **24**, 24, pp. 4307-4311 (1985).
- 4) Weingärtner, I., and Stenger, H.: Entwurf und Realisierung eines Projectionssystems mit holographischer Abbildungspotik. *Optik*, **66**, 3, pp. 277-287 (1984).
- 5) Weingärtner, I.: Real and Achromatic Imaging with Two Planner Holographic Elements. *Opt. Commun.*, **58**, 6, pp. 385-388 (1986).
- 6) Nowak, J., and Zajac, M.: Investigation of the Influence of Hologram Aberrations on the Light Intensity Distribution in the Image Plane. *Opt. Acta*, **30**, 12, pp. 1749-1767 (1983).



Masayuki Kato

Holography and Color-Imaging
Laboratory
FUJITSU LABORATORIES, ATSUGI
Bachelor of Applied Physics
Tokyo Institute of Technology 1981
Master of Applied Physics
Tokyo Institute of Technology 1983
Specializing in Holography and Laser
Optics



Fumio Yamagishi

Holography and Color-Imaging
Laboratory
FUJITSU LABORATORIES, ATSUGI
Bachelor of Electronics Eng.
Nagoya Institute of Technology 1970
Dr. of Electronics Eng.
Tohoku University 1976
Specializing in Holography and Laser
Optics



Satoshi Maeda

Holography and Color-Imaging
Laboratory
FUJITSU LABORATORIES, ATSUGI
Electronics Eng.
Kanazawa Technical College 1985
Specializing in Holography and Laser
Optics

SVEX: Switching Program Verification Expert System

• Jun'ichi Yamazaki • Kiyoshi Miyazaki • Tadamichi Suzuki

(Manuscript received September 1, 1989)

This paper describes SVEX, which can automatically find errors in switching programs. SVEX can also generate service specifications from the programs for testers to confirm that the programs meet the original specifications.

SVEX simulates switching on an object-oriented model of a target switching system. Logic errors are found by comparing the behavior of the model with the verification rules represented by demons. State transition diagrams are generated by tracing the behavior of the model.

SVEX has been applied to the development of Fujitsu's digital PBXs. SVEX has found 72 percent of all errors in logic, including some errors overlooked by the usual online testing.

1. Introduction

To develop highly reliable switching programs efficiently, it is important to confirm precisely and quickly whether the switching programs meet the requirements. Since testing of switching programs is time consuming, efficient verification of the programs is in demand to reduce development cost.

Verification of switching programs is usually done manually by online testing. A technician at a terminal checks the response of the system to confirm that the program is running correctly. The cost of present online testing is more than half of the total program development cost.

This high cost is due to the following reasons:

- 1) As the number of target switching systems and terminals for online testing are limited, programs to be tested form long queues.
- 2) Because online testing uses a black box test which checks only the response of the system caused by terminal operation, implicit errors are often overlooked. If an illegal response is observed, it is difficult to analyze the cause.
- 3) It is very difficult for a novice to select test items which cover all possible cases. The

program reliability after testing depends highly on the tester's skill.

An approach to solve these problems is to detect errors in the programs without using a real switching system. Syntax errors can be detected by a compiler. Errors which cannot be detected by a compiler are found by running programs on a simulator. To improve error detection, several tools such as visual debugger¹⁾ have been developed. Although the tools show the program's behavior, they cannot select test items, find errors, or analyze their causes.

SVEX^{2),3)} (switching program verification expert system) can simulate the behavior of the switching programs, cover all possible test items, find errors, and analyze their causes automatically. For simulation, a model reflecting a target switching system must be constructed. Using object-oriented methodology⁴⁾ enables a flexible model to be constructed at low cost. For error detection and analysis, the authors applied two kinds of technology: demon⁵⁾, which was developed to represent knowledge in artificial intelligence, and reverse engineering. The errors are found by comparing the behavior of the model with verification rules represented

by demons. State transition diagrams are used as service specifications and are generated in reverse from the programs by tracing the behavior of the model. This enables the programmers to confirm that the developed programs meet the original service specifications.

Errors in switching programs are classified in Chap. 2. The configuration of SVEX and the verification method are explained in Chap. 3. SVEX has been applied to the development of Fujitsu's digital PBXs. The results are described in Chap. 4. To make SVEX practical, it must be maintained without degrading current performance. The authors are now developing maintenance support facilities, which are described in Chap. 5. The concluding chapter summarizes the authors research and development and discusses future plans.

2. Errors in switching programs

SVEX verifies a kind of switching program, called call-processing programs, which consist of standardized program units called macroinstructions. These programs analyze signals generated according to the user's operations on telecommunication terminals and control hardware such as speech path networks, terminals, and trunks. It is necessary to verify that the programs provide the service requested by the user, that switching hardware is correctly controlled, and that data such as office data, subscriber data, and call control data are correctly used. However, errors are inevitable because of misunderstanding of the specifications, design errors, and coding errors.

We have divided errors into three classes:

1) Syntax errors

Syntax errors violate the programming language grammar. They are usually found by a compiler.

2) Logic errors

Logic errors violate the general rules which call-processing programs must follow and are independent of service specifications. Logic errors usually cause internal logical contradictions and catastrophic faults such as protocol deadlocks, and inconsistencies between the transaction memory and hardware status.

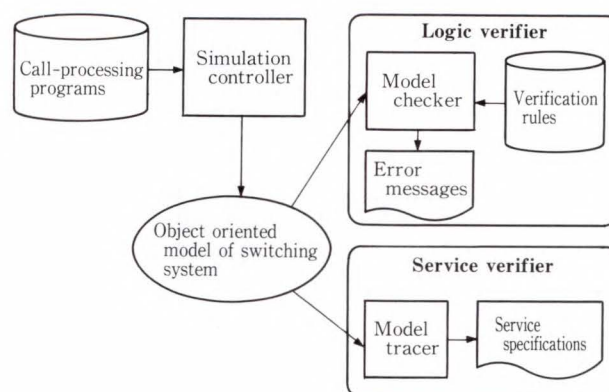


Fig. 1—Configuration of SVEX.

3) Service errors

Even in the absence of syntax and logic errors, when programs don't meet the original service specifications, service errors can exist. For example, the beep tone heard at a terminal or a lamp displayed on an attendance console may be inadequate. Traffic may be measured incorrectly.

Since a compiler can find syntax errors, our objective is to achieve logic and service verification.

3. Configuration and verification method

Figure 1 shows the configuration of SVEX. It consists of four components: a model of the target switching system, a simulation controller, a logic verifier, and a service verified.

The simulation controller reads call processing programs and simulates all possible situations of the model according to the input programs. The model checker (see Fig. 1) compares the model behavior with the verification rules. If it detects a logic error as a violation of the rules, it outputs an error message. The model tracer (see Fig. 1) traces the behavior of the model and outputs tracing results as service specifications for the programmers to point out service errors. Implementation of these components are described in the following sections.

3.1 Object-oriented model of the switching system

The model of the switching system is made by using a set of objects. Each object corre-

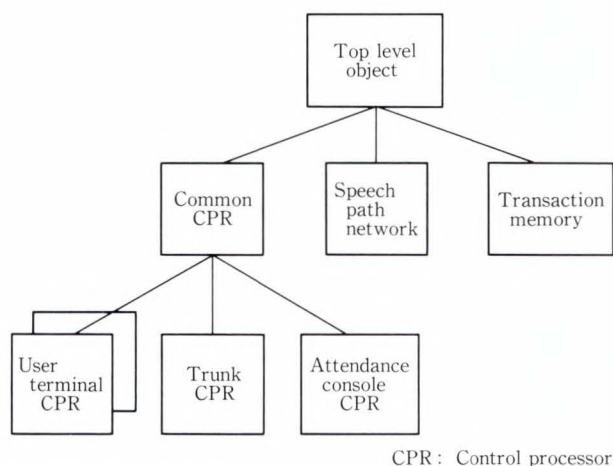


Fig. 2—Hierarchical structure of objects constructing model.

sponds to a component of the target switching system, such as a terminal controller, which controls user terminals, trunks, an attendance console, a speech path network, and transaction memory.

When a macroinstruction of the call-processing program is executed on a component, the component causes a state transition and generates output signals. In the model, the state of a component represented by instance variable of the object and the functions of macroinstructions are represented by methods which update instance variables.

There are common macroinstructions and specific macroinstructions for each terminal controller. The methods corresponding to common macroinstructions are written in a superclass of the objects. Figure 2 shows the hierarchical structure of objects constructing the model. Using this hierarchical structure, when a new type of terminal and a new terminal controller are added, a new object is defined as a subclass of the common object and write methods which simulate specific macroinstructions for the new terminal controller. Similarly, basic methods used in all objects in common are written at the top level object.

3.2 Simulation control by reachability tree analysis

The simulation controller reads and parses the source code of call-processing programs. It

checks whether the values for parameters of macroinstructions are in the range defined by the specifications for the macroinstructions. If it finds a parameter error, it outputs an error message.

To verify a switching program as completely as possible, all possible behavior of the switching system must be simulated using the model. The basic behavior of the switching system is as follows. While the switching system is stable, the call processing program supervises events generated by terminal controllers. When it detects an event, it executes the sequence of macroinstructions and changes the switching system into another stable state.

The switching system controlled by the call-processing programs is generally regarded as a finite state machine. Therefore, a reachability tree analysis⁶⁾ is applicable. The simulation controller controls simulation according to the following algorithm to obtain all possible system states.

- 1) Initialize the instance variables of objects corresponding to the initial system state.
- 2) Examine which events can be generated by terminal controllers in the system state.
- 3) Execute the following steps as sequences of macroinstructions following all events which are generated.
 - i) Invoke methods corresponding to macroinstructions in the sequence.
 - ii) Update instance variables by executing the methods.
 - iii) After executing all methods in the sequence, if there is a state equal to the current state in the list of states, stop the processing. Otherwise, add the current state to the list and go to step 2).

3.3 Logic verification by demons⁵⁾

Logic errors are found by comparing the behavior of the model with the formalized verification rules. To change and add verification rules, verification rules are represented by demons individually.

The general form of a demon is as follows:

```
(DEMON <demon name>
  (<parameter list>)
```

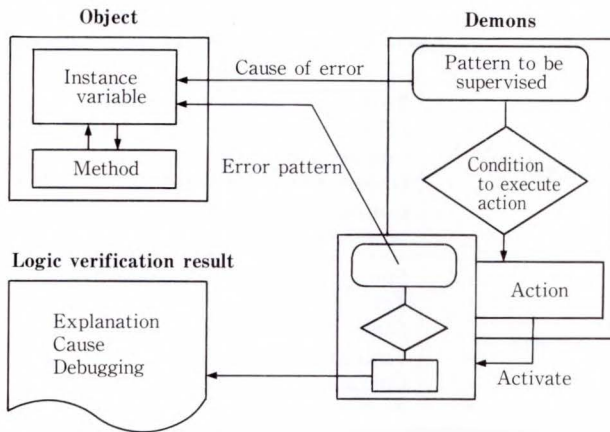


Fig. 3—Logic verification by demons.

```

((pattern to be supervised))
((condition to execute action))
.<action>
    
```

The method of verification using demons is as follows.

When the model checker (see Fig. 1) compares the instance variables of the objects with the pattern of the demon to be supervised (referred to below as the pattern), if there is a match, control is immediately transferred to the demon which has the matched pattern, the demon examines the condition to execute action, and if the condition is satisfied the action is executed.

Whenever an instance variable of an object is updated, the patterns of all demons are compared with the instance variables. This method can deal with any form of demon, but is very inefficient because much time is spent comparing all the demons, and the conditions to execute action must be detailed to prevent other actions of demons from being executed.

To control demons efficiently, the number of comparisons between the patterns and instance variables is minimized by using the following two methods.

1) Control of demons by their scope

Demons are divided into groups according to their supervising objects. When an instance variable in an object is updated, the only demons which supervise the object are compared with the instance variable.

2) Control of demons by their lifetime

ERR163	
Position	: line 866.
Explanation	: PB receiver is not driven at end of transition. Nevertheless it is hunted at line 860.
Cause	: not to send a drive order to PB receiver.
Debugging	: add a drive order “%RPROD TOPBCR, C6” to SP order part.
ERR135	
Position	: from line 953 to 972.
Explanation	: macroinstructions are nonexecutable.
Cause	: LC cannot generate EVENT LNHK.
Debugging	: change line 923 order into “%RPROD ODSPON, C1, HKN”

Fig. 4—Examples of logic verification results.

The demons are activated and deactivated according to the order of the pattern appearance. The pattern of a demon which supervises the first pattern appearing is compared initially. When the first pattern appearing is found, the demon executes its action, activates the next demon for the next pattern appearing, and the first demon is deactivated. Using this method, only demons that are useful at the time supervise the objects.

Figure 3 explains the error detection and analysis of the causes of errors. A demon which supervises the causes of errors is activated. When the cause of an error is found, the demon activates the next demon for the next error pattern appearing. If the next demon finds the error pattern, it outputs an error message with the cause.

Figure 4 shows examples of logic verification results obtained by demons. The logic verification results include positions where errors occurred, explanation of errors, causes of errors, and advice for debugging.

3.4 Service verification by generating service specifications

If complete service specifications are described formally, the service errors can be found automatically. However, it is difficult to define service specifications completely including exceptional sequences at an early phase of the

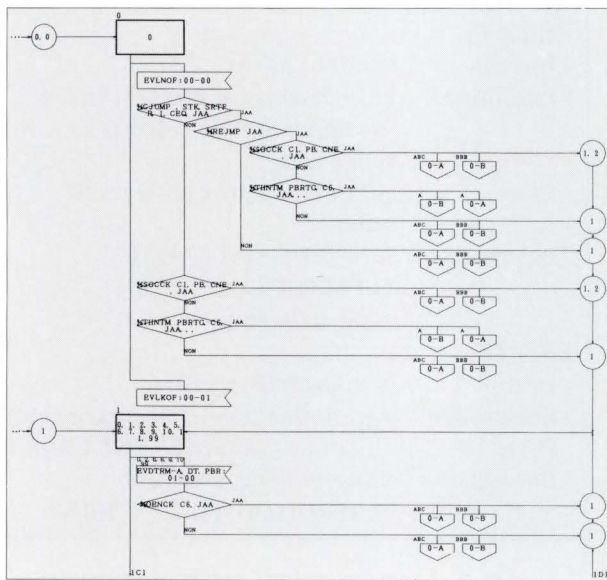


Fig. 5—Example of the transition chart.

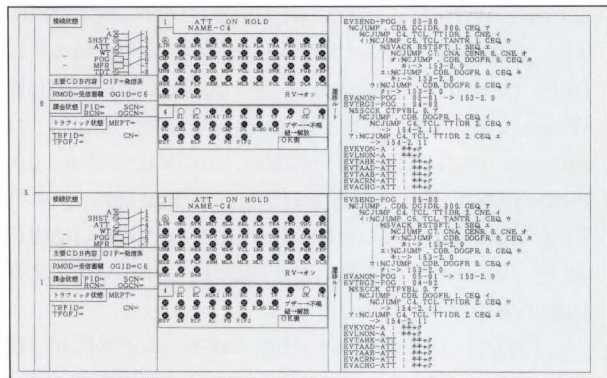


Fig. 6—Example of the state table.

practical switching program development process.

As a practical solution for detecting the service errors, SVEX generates service specifications based on state transitions from the programs to be verified. Comparing the generated specifications with the original specifications, the programmer then confirms that the program meets the original specifications.

SVEX outputs two types of state transition diagrams, a transition-oriented one called a transition chart and a state-oriented one called a state table.

The transition charts show the processing summary of each transition. Figure 5 shows an example of the transition charts which SVEX

Table 1. Verification items of SVEX

Verification	Function
Logic	Protocol between processors (Deadlock, unspecified receptions, nonexecutable transitions)
	Order of macroinstructions
	Consistency between memory operation and hardware operation
Service	Speech path network connections
	Terminal indications
	Digits receiving and sending
	Timing processing
	Charging processing
	Traffic measurement

Table 2. Evaluation results

Item	Capacity
Applied program size	146-Kstep
Total processing CPU time	11 h
Logic verification performance	72 percent
Logic verification reliability	76 percent

outputs.

The state tables show the details of each system state, such as speech path network connection patterns, status of transaction memory, and terminal indications. When a new element, for example a new type of terminal, is added to the switching system, the item must be shown on the state table. SVEX formats items in the state table according to the data which can be re-defined. Figure 6 shows an example of the state tables which SVEX outputs.

4. Evaluation

SVEX is implemented on a FACOM M series mainframe computer. About 150 demons and 20 objects are currently installed. The system is written in LISP. Table 1 shows the SVEX verification items.

SVEX has been applied to the development of Fujitsu's digital PBXs. SVEX verifies the call-processing programs before online testing. The evaluation results are listed in Table 2. The logic verification performance is the percentage of logic errors found by SVEX of the total errors including errors found by online testing. Logic verification reliability is the percentage of correct error messages.

There were two types of logic errors which were missed by SVEX and found by online testing. These were errors missed by demons and errors missed by the model. The errors missed by demons could have been found by SVEX if the required demons had been added beforehand. The errors missed by the model cause illegal behavior out of the modeling range. However, it is too costly to enhance the model to find some of these errors which are found by online testing easily. The proper modeling range should be selected by carefully considering both verification performance and model construction costs. If the model and the demons had been maintained in advance, the logic verification performance is estimated to have been more than 90 percent.

Incorrect error messages were caused by exceptions of demons and modification of the target system. They should have been removed by updating the model and demons.

SVEX detected errors overlooked during online testing in the programs which were made by adding some steps to old programs. These errors include those which are not errors in the present program, but that will become errors in the future if the program is enhanced or modified.

5. Maintenance support facilities

According to the evaluation results, it is necessary to maintain the model and the demons so that SVEX can be used without degrading its performance. The authors are now developing maintenance support facilities for the model and demons. Information which is necessary to maintain them can be taken from the documents which are produced in the call-processing programs development process.

The documents stored in a data base should be formalized sufficiently to enable them to be translated into the model and demons. The methods of objects in the model are made by translating the descriptions of the documents which specifies the function of the macro-instructions. The descriptions are formally represented by a set of predetermined primitive switching functions. Demons are obtained by

translating the descriptions of how to use the macroinstructions. Some types of templates are prepared so that demons may be written easily.

The use of multiwindows on a workstation makes the document data base easier to access. Because the data base is constructed based on hypertext⁷⁾, related documents can be referenced by link traversing. Consistency between documents which are linked by the special type of links are checked automatically. By using this mechanism, synchronous updating between documents and SVEX is confirmed.

6. Conclusion

SVEX can automatically find errors in call-processing programs. SVEX can also generate service specifications from the programs in reverse. The verification is performed by simulation based on the object oriented model of the switching system and AI technology.

SVEX was applied to the development of Fujitsu's digital PBXs. It is confirmed that SVEX is useful in the development of reliable switching programs.

To continue its use without degrading performance, maintenance of SVEX along with target modification is necessary. The authors are now developing the maintenance support facilities, in which design information including expertise is represented formally, stored in a data base, and the consistency between them is confirmed.

If such a development environment is constructed, it will be possible to develop other powerful automatic tools which can accelerate software development⁸⁾.

References

- 1) Isoda, S., Shimomura, T., and Ono, Y.: VIPS: A Visual Debugger. *IEEE Software*, 4, 3, pp. 8-19 (1987).
- 2) Yamazaki, J., Fujii, Y., Kakemizu, M., Iwami, Y., Kishida, T., and Kiyokane, Y.: Verification of Switching Program by Object Oriented Simulator. *IEEE Proc. 7th IPCCC*, 1988, pp. 296-300.
- 3) Miyazaki, K., Yamazaki, J., Kakemizu, M., Iwami, Y., Kishida, T., and Suzuki, T.: SVEX: Switching

Program Verification Expert System. IEEE Proc. 7th SETSS, 1989, pp. 178-182.

- 4) Goldberg, A.: Smalltalk-80 The Interactive Programming Environment. Series in Comput. Sci., Mass., Addison-Wesley, 1984, 516p.
- 5) Charniak, T.: Toward a Model of Children's Story Comprehension. MIT AL Lab., 1972, Ph.D. Thesis.
- 6) Zafiropulo, P., West, C.H., Rudin, H., Cowan, D.D,

and Brand, D.: Towards Analyzing and Synthesizing Protocols. *IEEE Trans. Couun.*, **COM-28**, 4, pp. 651-661 (1980).

- 7) Conklin, J.: Hypertext: An Introduction and Survey *IEEE Computer*, **20**, 9, pp. 17-41 (1987).
- 8) Sugioka, R.: Telecommunications Software Development; Today and Tommorrow. IEEE Proc. GLOBECOM, 1988, pp. 730-734.



Jun'ichi Yamazaki

Integrated Communications Network Laboratory
FUJITSU LABORATORIES,
KAWASAKI
Bachelor of Electric Eng.
Keio University, 1979
Master of Electric Eng.
Keio University, 1981
Specializing in Switching Software Development Technology



Tadamichi Suzuki

Engineering Dept.
Communications
Software Development Div.
FUJITSU LIMITED
Bachelor of Electronic Eng.
tohoku University, 1973
Specializing in Telecommunications Software Development Technology



Kiyoshi Miyazaki

Integrated Communication Network Laboratory
FUJITSU LABORATORIES,
KAWASAKI
Bachelor of Physics
Osaka University, 1967
Master of Physics
Osaka University, 1969
Specializing in Switching Software Development Technology

Compact Three-Axis Accelerometer System (CTAS) for Microgravity Experiments

• Fumio Takei

(Manuscript received August 31, 1989)

The measurement of the acceleration environment in microgravity experiments is very important. Conventional accelerometer systems, however, are too large and bulky for microgravity experiments. A microcomputer-based compact system that uses a static memory IC module for data storage was developed. The system's servo accelerometers ensure its accuracy and reliability. Usefulness of the system was verified in a microgravity experiment on-board NASA's KC-135, which is designed for parabolic flight.

1. Introduction

Scientific experiments in microgravity have become more common because of the progress achieved in space technology. Craft such as the space shuttle have made possible several microgravity experiments related to life sciences, materials processing, and the study of basic physical phenomena¹⁾.

In microgravity, there is no convection or precipitation such as that occurring in gravity due to density differences in liquid phases. The unique environment microgravity provides is expected to enable new materials to be developed, and as yet unknown phenomena to be discovered.

The measurement of gravitational acceleration in microgravity experiments is important in determining the results of experiments²⁾, especially in quantitative analysis. However, conventional accelerometer systems are too large and bulky for use in launch payloads. This is because most systems use magnetic tape or disks as the data recording media, and therefore contain heavy mechanical drives. Moreover, mechanical drives tend to generate vibrations causing perturbations in microgravity. Such recording systems are also too sensitive to withstand the shock and vibration of space

vehicle launching and landing.

We developed a compact three-axis accelerometer system (CTAS) that uses a memory cassette to store data. To verify the CTAS operation, we used it in microgravity experiments on-board aircraft designed for parabolic flight.

2. CTAS structure

2.1 Requirements

The CTAS had to meet the following requirements:

- 1) Compact light-weight structure that meets restrictions in payload size
- 2) Low power consumption to conserve energy
- 3) Wide measurement range
- 4) Ability to withstand the mechanical shock and vibration of launching and landing.

2.2 Hardware design

To meet the above requirements, we decided the following:

- 1) The experiment payload will only consist of equipment for the collection and recording of acceleration data. Data will be read and processed after the experiment has been completed (possibly on the ground).
- 2) No mechanical moving parts will be used

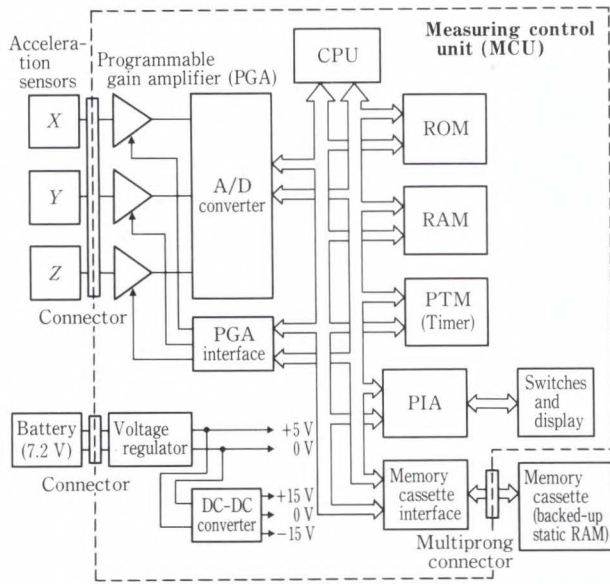


Fig. 1—CTAS block diagram.

in the data recording media.

Based on the above, we designed the CTAS in three functional blocks (see Fig. 1).

2.2.1 Acceleration sensor block

Japanese Aviation Electronics Industry's JA-5V servo accelerometers were used because they provide highly precise measurement in microgravity. These accelerometers usually have a resolution of 1 μ G and the ability to detect both vibration and static change in acceleration. In addition, they have a measurement range of up to 20 G. The system can also be used to measure the shock and hyper gravity of a space vehicle launching.

The three accelerometers are arranged orthogonally. Output voltage signals are proportional to acceleration and are sent directly to the measuring control unit.

Calibration of the sensors was carried out by settling the sensors parallel (0 G) and perpendicular (± 1 G) to the ground. The calibration data was input to the computer file to calculate the acceleration value from the voltage signal after completion of the experiment.

2.2.2 Measuring control unit (MCU)

The (MCU) is microcomputer-based. It collects and stores acceleration data as binary digital data. The MCU use the MBL6809 8-bit microprocessor.

Table 1. CTAS specification

Item	Specifications
Maximum range	± 10 G
Resolution	10 μ G
Sampling rate	10-100 ms
Memory cassette capacity	128 Kbyte
Measurement time (dependent on sampling rate)	210-2 100 s per memory cassette
Power consumption	7.2 V DC, 8 W
Size of MCU	180 (l) \times 120 (b) \times 120 (h), mm
Maximum weight	3.0 kg

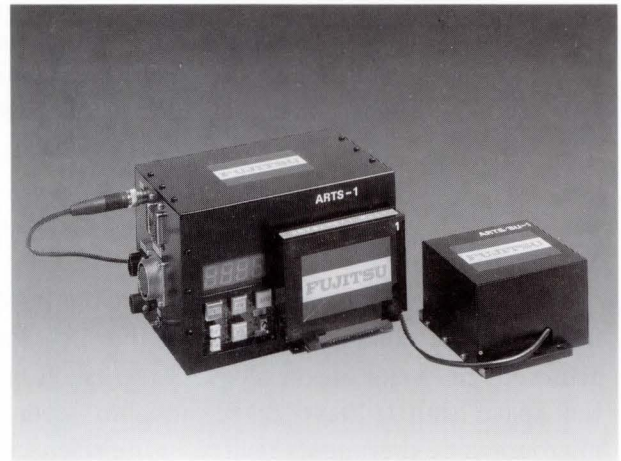


Fig. 2—Prototype CTAS.

This device does the following:

- 1) Optimizes the amplification of the accelerometer signal.
- 2) Generates sample timing signals.
- 3) Controls the storage of data in the memory cassette.
- 4) Display the CTAS status.

The MCU runs for one hour on a 7.2 V, 1 200 mAh Ni-Cd battery module.

2.2.3 Memory cassette

The memory cassette used to record data consists of four 256-Kbit static RAM ICs backed up by a lithium battery. This system serves as a pseudo non-volatile memory. The cassette prototype has a capacity of 128 Kbytes, enabling it to record acceleration changes for up to 2 100 s at a 100-ms sampling rate.

The cassette is connected to the MCU by a multiprong connector. After measurement

data has been collected and stored, the cassette data is processed by a personal computer through an interface circuit. This enables different types of data processing, for example, graph drawing and statistical calculation.

The memory cassette's size greatly reduces the system's size and weight. The memory cassette also records data reliably during high and low acceleration. The system's low power consumption enables it to run on its own battery.

Table 1 gives the CTAS specifications. The prototype CTAS is shown in Fig. 2.

3. Experiments in microgravity

3.1 KC-135 designed for parabolic flight

NASA's KC-135³⁾ Weightless Wonder IV (see Fig. 3) is a specialized plane used in parabolic flight to produce microgravity. Figure 4 shows the flight trajectory and shows that each parabola provides 20 s of microgravity.

3.2 Results of the acceleration measurement

3.2.1 Acceleration change during parabolic flight

The CTAS was put in an experiment module on-board the KC-135. Figure 5 shows typical acceleration changes in the KC-135 during its parabolic flight. This data was collected with the module fixed to the floor of the KC-135. At the beginning of the parabola, the gravity was 1.8 G along the Z axis (perpendicular to the floor). When the engine thrust was reduced, a low gravity state was reached within 3 s. This state lasted for 20 s. After the microgravity state, a gravity of 1.8 G was reached in the last part of the parabola.

Along the Y axis (aircraft nose-to-tail axis), the acceleration was about 0.2 G at the beginning of the parabola. When the engine thrust was reduced, a low gravity state similar to that reached in the Z axis was reached in the Y axis.

Data for the Y and Z axes changes markedly during parabolic flight, but data for the X axis (parallel to the wings) changes little.

Thus, the CTAS provides precise acceleration data in high and low gravity.

3.2.2 Measurement during free-floating

The microgravity provided by the KC-135 leaves something to be desired. As shown in Fig. 5, vibration and acceleration remained

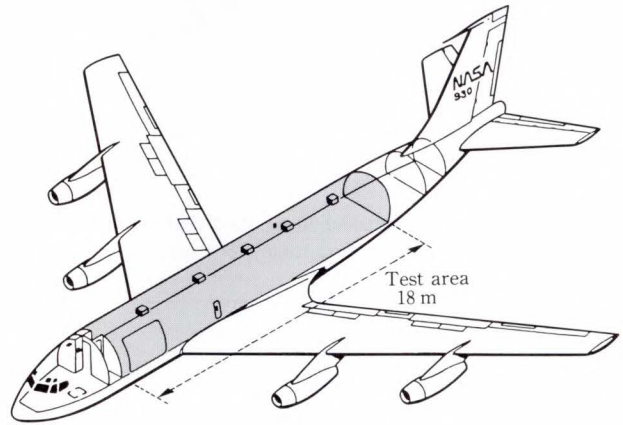


Fig. 3—Parabolic-flight aircraft KC-135³⁾.

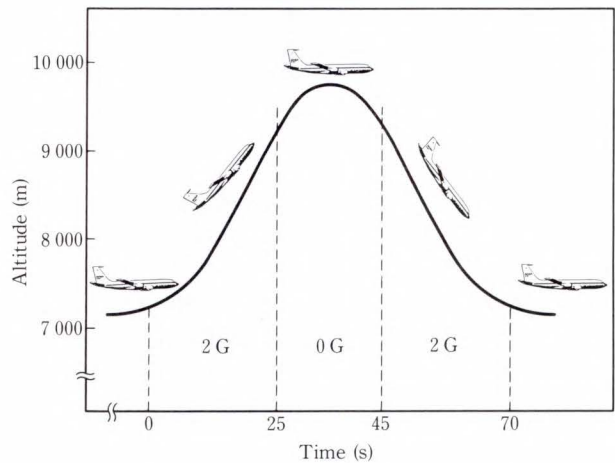


Fig. 4—KC-135 trajectory.

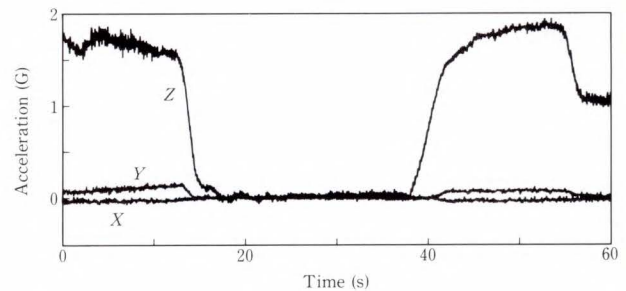


Fig. 5—Acceleration change during parabolic flight (X-axis: Parallel to wings, Y-axis: Aircraft nose-to-tail axis, and Z-axis: Perpendicular to aircraft floor).

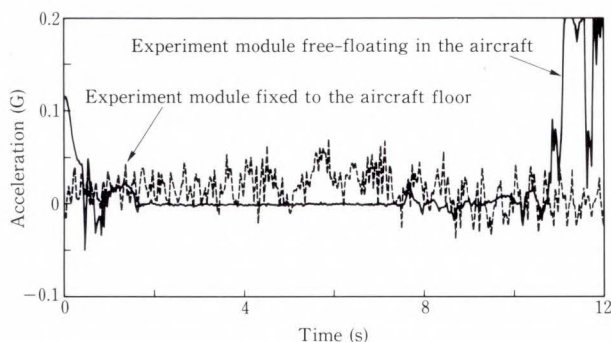


Fig. 6—Comparison of acceleration data (Sampling rate: 33.3 ms).

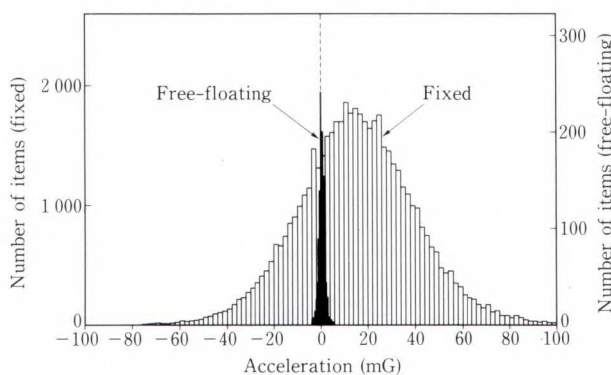


Fig. 7—Distribution of acceleration data (Sampling rate: 33.3 ms).

as fluctuation components. This fluctuation is due to engine vibration and deviation from the ideal parabolic trajectory. The microgravity in space is almost zero, and this is needed to eliminate fluctuation in parabolic flight.

To improve the microgravity environment, we tried making the experiment module free-floating. Figure 6 shows the acceleration change of the free-floating module (solid line), and that of the fixed module (broken line). Vibration and 20-30 mG gravity can be observed in the fixed module, but by free-floating the module, the acceleration change was reduced to almost zero. The large changes in acceleration in the free-floating module are caused by the module being supported by hand.

The differences become clearer after statistical analysis. The histogram in Fig. 7 plots data for each division of acceleration and shows that the distribution definitely differs. Clearly, the acceleration environment can be improved by free-floating the experiment module.

CTAS enables the measurement of acceleration during free-floating. Its unique data recording media, (the memory cassette), greatly reduce the system size and weight. Moreover, highly accurate measurement using servo accelerometers was verified in the free-floating experiment.

4. Conclusion

We have developed a compact three-axis accelerometer system and verified its operation. This system runs on batteries. Its low size, weight, and power consumption make it suitable for microgravity experiments on-board an aircraft or space vehicle. We are now improving the safety of the CTAS for use in space experiments.

References

- 1) DeLucas, L.J., Suddath, F.L., Snyder, R., Naumann, R., Broom, M.B., Pusey, M., Yost, V., Herren, B., Carter, D., Nelson, B., Meeham, E.J., McPherson, A., and Bugg, C.E.: Preliminary Investigations of Protein Crystal Growth Using the Space Shuttle. *J. Cryst. Growth*, **76**, pp. 681-693 (1986).
- 2) Feuerbacher, B., Hamacher, H., and Jirg, R.: Analysis of Microgravity Measurement on D1.IAF-87-395, (1987).
- 3) NASA: JSC Reduced Gravity Aircraft User's Guide. NASA Johnson Space Center, Houston, Tex., (1981).



Fumio Takei

Organic Materials Laboratory
FUJITSU LABORATORIES, ATSUGI
Bachelor of Applied Chemistry
Tokyo Metropolitan University, 1982
Master of Polymer Science
Tokyo Metropolitan University, 1984
Specializing in Chemistry

Soft X-Ray Lithography Using Synchrotron Radiation

• Yoshimi Yamashita • Syunji Gotoh • Hidetoshi Ishiwari

(Manuscript received September 14, 1989)

The BL-17C beamline was constructed for soft X-ray lithography at the Photon Factory of the National Laboratory for High Energy Physics. Research on the fundamental characteristics of pattern replication has been conducted using the beamline.

This report describes replicated resist pattern profiles and pattern replication accuracy. A method of accuracy evaluation was proposed and the exposure conditions necessary for accurate replication using positive resist (CMR) were obtained.

These results indicated a fair possibility of high replication accuracy in sub quarter-micron patterns.

1. Introduction

Microfabrication technology in VLSIs is continuously advancing. If the current rate of advance is projected, VLSI device patterns will reach quarter-micron size within several years.

For the fabrication of such device patterns, soft X-ray lithography using synchrotron radiation (SR) is a promising technology because of its high brightness, high intensity, and collimation. The SR emitted from an electron storage ring has a broad continuous spectrum ranging from X-ray to infrared. In soft X-ray lithography, the region between 0.4 nm to 1.5 nm is used.

We constructed the BL-17C beamline for soft X-ray lithography at the Photon Factory of the National Laboratory for High Energy Physics. This beamline accepts SR emitted from a bending magnet B17 at the 2.5 GeV ring. An SR spectrum measurement system for measuring X-rays scattered by helium (He) gas was developed.

The BL-17C beamline has double quartz mirrors with a variable glancing angle and a 200 μm -thick beryllium (Be) window. The wavelength distribution of X-rays emitted through the Be window is set by adjusting the glancing angle of the double mirror.

This system was used to determine the

optimum conditions and configuration of the beamline for soft X-ray lithography. In replication experiments, the dependence of mask contrast and resist profile on wavelength was obtained. The dependence of the replicated pattern accuracy on the glancing angle and proximity gap was also investigated.

These results will greatly assist in the future development of soft X-ray lithography using SR.

2. Optics of the beamline BL-17C

2.1 Beamline

BL-17C is a branch beamline for X-ray lithography. Figure 1 is a schematic drawing of the beamline. To obtain a photon energy region suitable for X-ray lithography, we used a double mirror (two parallel mirrors) to remove high energy photons and a Be window to remove low energy photons.

The cutoff energies can be changed by changing the material and glancing angle of the mirrors and by changing the Be window thickness. Fused quartz mirrors were used in this experiment. By using two parallel mirrors, the reflected beam can be made to fall on the same position on the target even if the glancing angle is changed.

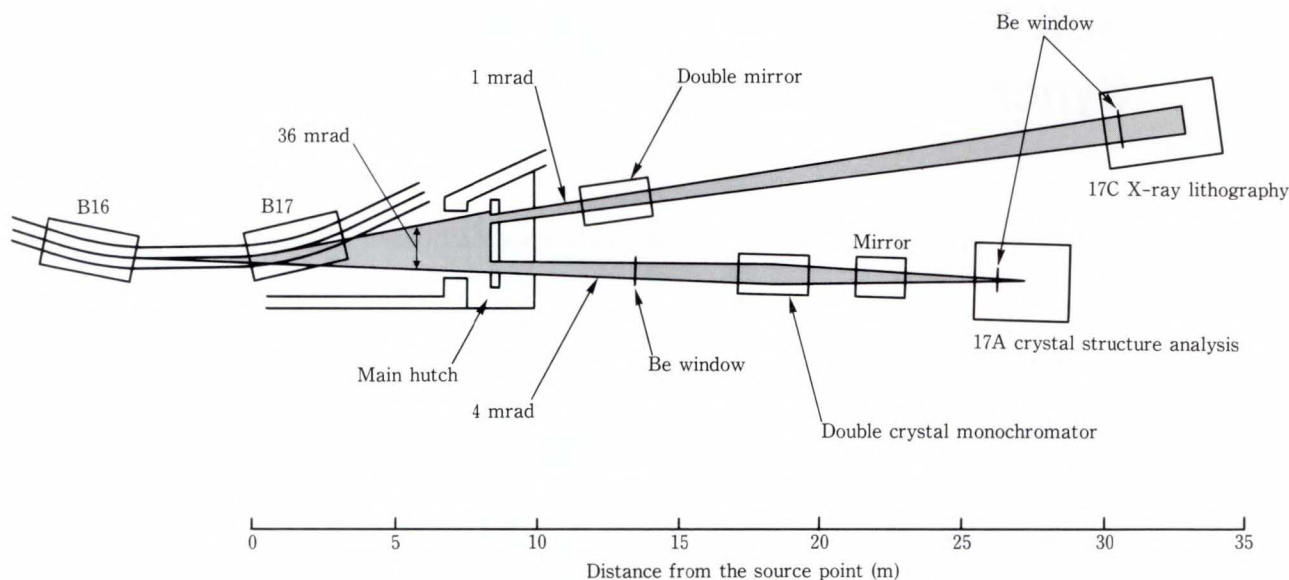


Fig. 1—Schematic drawing of the branch beam line BI-17C.

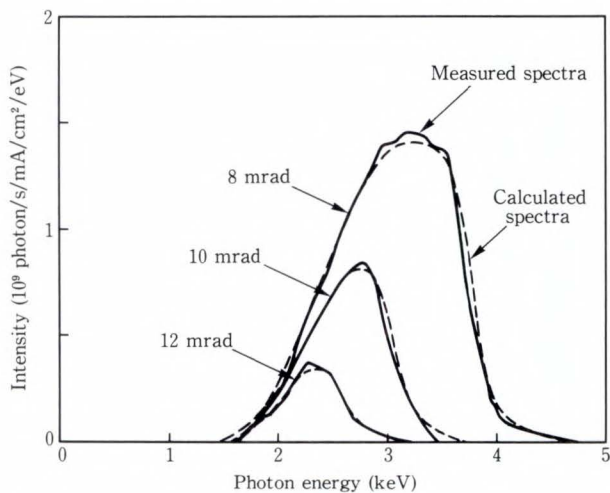


Fig. 2—Spectra of SR reflected by two quartz mirrors and passed through a 200 μm -thick Be window.

2.2 SR spectrum measurement

To evaluate the optical characteristics of the beamline, the SR spectrum was measured. We developed a method to measure the SR spectrum that passed through the beamline. This method uses He gas scattering and an energy-dispersive Si (Li) detector¹⁾. Under a ring current of 200 mA, the photon flux at the end of the beamline reaches 10^{12} photon/s. It is, however, not possible to count such a high intensity of photons because the Si (Li) detector is limited to a few thousand count/s. Therefore,

we measured the reduced intensity of X-rays scattered by He gas at 1 atm and estimated the SR spectrum using He gas scattering theory.

We measured the SR spectra at the end of the beamline²⁾. The solid curves in Fig. 2 show the measured spectra of SR that passed through a 200 μm -thick Be window after being reflected by the double mirror. The glancing angle of the mirrors was set to 8-, 10-, and 12-mrad. The dashed curves were obtained from a calculation that takes into account the reflection at the double mirror and absorption in the Be window. These results agree very well with the measured spectra. The critical energy at which the incident X-rays are totally reflected decreases as the glancing angle increases. The cut off at about 2 keV is due to absorption by the Be window.

3. Replication experiment

3.1 Mask and equipment

The structure of the X-ray mask at each fabrication step is shown in Fig. 3. The mask consists of a 0.65 μm -thick tantalum (Ta) absorber on a 2 μm -thick silicon nitride (SiN) membrane. Ta patterns including a 0.2 μm line and space were defined by reactive ion etching (RIE). After Ta etching, a silicon back etching process was used to form a SiN membrane window. A photograph of the X-ray mask is

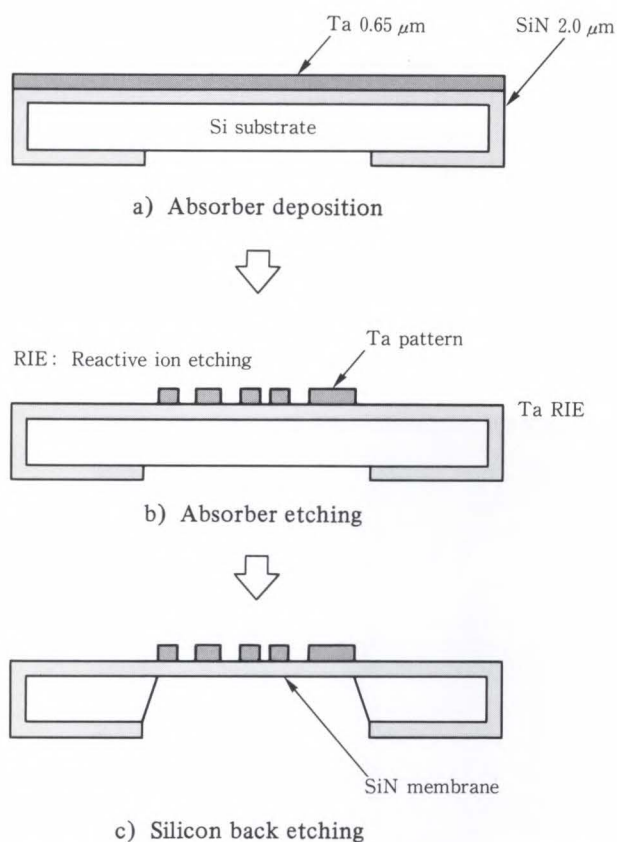


Fig. 3—Structure and fabrication steps of X-ray mask.

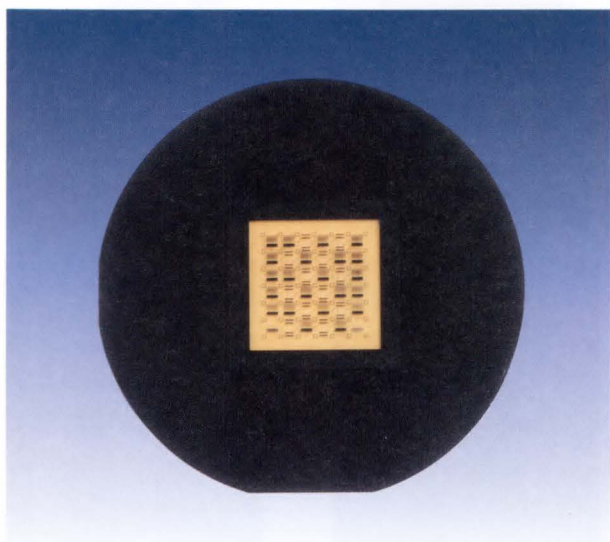


Fig. 4—Photograph of X-ray mask (76.2 mm dia).

shown in Fig. 4. This mask has a $25 \times 25 \text{ mm}^2$ SiN membrane window in a 76.2 mm dia silicon wafer substrate.

The equipment for the replication experi-

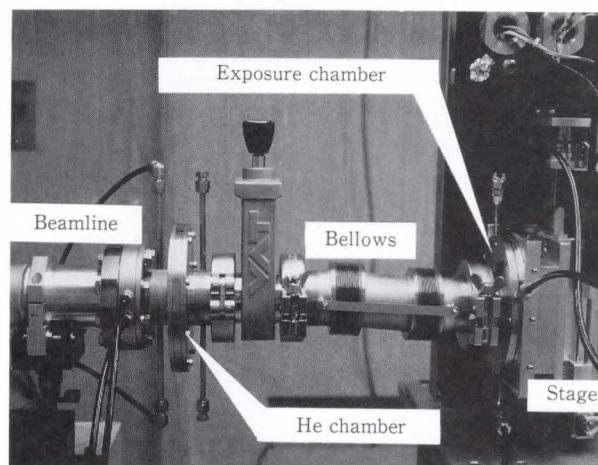


Fig. 5—Photograph of equipment for the replication experiment.

ments is shown in Fig. 5. This equipment was fixed behind the Be window. It consists of a He chamber that protects the Be window against erosion, a connecting bellows, and an exposure chamber on a moving stage. To control the gas environment, this exposure chamber has a vacuum line and a gas line. The distance between the He chamber and mask is about 330 mm.

3.2 Exposure characteristics

A positive resist of $0.5 \mu\text{m}$ -thick polyfluoro methacrylate (Daikin, FBM-120) was used in the experiment. Resist films were spin-coated on Si wafers and prebaked at 140°C for 30 min.

The critical exposure time, defined as the minimum exposure time necessary to completely remove the resist in development, was measured at different spectra by changing the glancing angle of the mirrors. The resist was developed at 23°C for 90 s in 0.7 percent methyl isobutyl ketone (MIBK) diluted with isopropyl alcohol (IPA).

The results are summarized in Table 1. In this paper, we have defined a dose as the product of the beam current $I(\text{A})$ in the storage ring and the exposure time $t(\text{s})$. This minimum $I \times t$ product required to completely remove the resist is referred to as the critical dose. Because the exposure level under the Ta absorber decreases due to larger absorption, the critical

dose increases for the Ta region. The mask contrast, defined as the ratio of transmitted doses under the SiN membrane to that under the Ta absorber, was obtained experimentally as the inverse of the ratio of critical doses in these two regions.

Table 1 shows that the critical dose and the mask contrast increase as the glancing angle increases from 8 mrad to 12 mrad. The experimental results of mask contrast agree with calculations based on absorption by the Ta absorber.

3.3 Effect of exposure conditions on pattern profile

We used 5 μm -thick crosslinked polymethyl methacrylate resist (CMR) to investigate the resist pattern profile. Resist films were spin-coated on Si wafers and prebaked at 200 $^{\circ}\text{C}$ for 270 s. Development was mainly performed in MIBK at 23 $^{\circ}\text{C}$ for 120 s.

Table 1. Wavelength peak, critical dose under the SiN membrane, and contrast for various glancing angles

Glancing angle (mrad)	8	10	12	
Wavelength peak λ_p (nm)	0.35	0.42	0.50	
Critical dose (A·s)	~0.3	1.3	5.0	
Contrast	Experiment	~4	~10	~18
	Calculation	5.8	11	19

SEM photograph of replicated patterns exposed in air are shown in Fig. 6. The replicated resist patterns have negative tapering at the upper corner and under-cutting at the bottom corner. These pattern profiles have a bad influence on mask pattern replication. The under-cut profile above the silicon substrate is caused by Auger electrons from the substrate^{3),4)}. However, the cause of the negative tapering at the upper corner remains unknown.

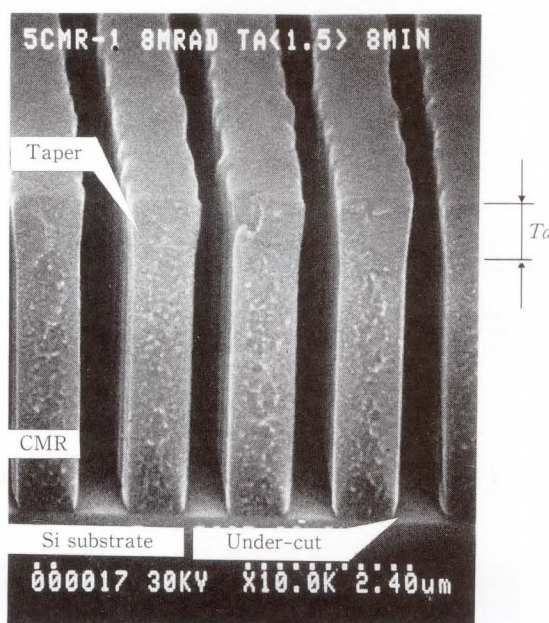


Fig. 6—Cross sectional SEM photomicrograph of a replicated resist pattern exposed in air.

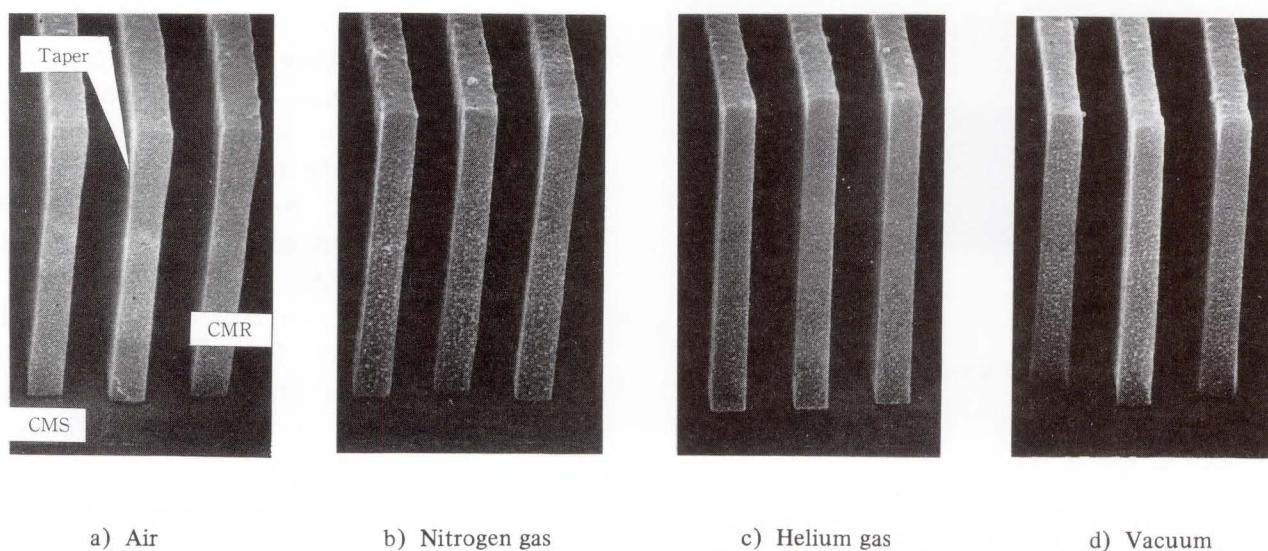


Fig. 7—Cross sectional profile of replicated resist patterns exposed in various environments.

Because the efficiency of emitting Auger electrons is smaller in chloromethylated polystyrene (CMS) than in Si, we inserted a 0.8 μm-thick resist between the CMR and Si substrate to eliminate Auger electrons. The CMS was hardened by UV exposure for 10 min before the CMR was coated. The results for exposures in a) air, b) nitrogen (N₂) gas, c) He gas, and d) vacuum are shown in Fig. 7.

These profiles have no under-cutting, which suggests that the under-cutting of the Si substrate was caused by Auger electrons. A negative taper of the upper corner was only observed in the sample exposed in air. The cause of these taper profiles may be diffusion of oxygen. The measured dissolution rates of CMR exposed in N₂ and air were 240 nm/min and 75 nm/min at 10 mrad and 100 A·s respectively. This indicates that a low dissolution layer is formed in air.

In Fig. 6, the negative taper depth is defined as *Td*. If the taper is caused by diffusion of oxygen, *Td* will change with exposure time and oxygen density.

The general diffusion equation is given by

$$n(x, t) = n_0 \operatorname{erfc} \left(\frac{x}{2\sqrt{D \cdot t}} \right), \quad \dots (1)$$

where *x* is the distance from the surface, *n*₀ is the surface oxygen density at atmospheric pressure, *n* is the density at *x*, *t* is the diffusion time and *D* is the diffusion coefficient. (*D* is constant at room temperature.)

The negative taper depth *Td*₀ at atmospheric pressure is derived as

$$Td_0 = 2\sqrt{D \cdot t} \operatorname{erfc}^{-1} \left(\frac{n_j}{n_0} \right), \quad \dots (2)$$

where *n*_{*j*} is the density at *x* = *Td*₀. *Td*₀ in Equation (2) is proportional to *t*^{1/2}.

If the pressure *P* differs from atmospheric pressure *P*₀, the surface density *n*₁ changes so that

$$n_1 = r \cdot n_0, \quad \dots (3)$$

where *r* is the pressure ratio $\frac{P}{P_0}$. Then, *Td* at pressure *P* is given by

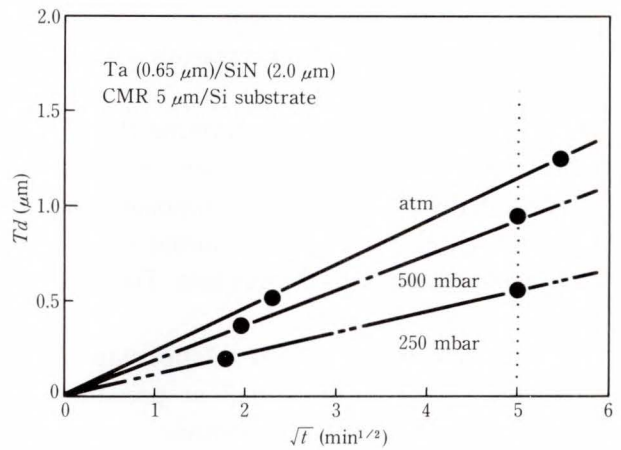


Fig. 8—Negative taper depth *Td* for various pressures and times.

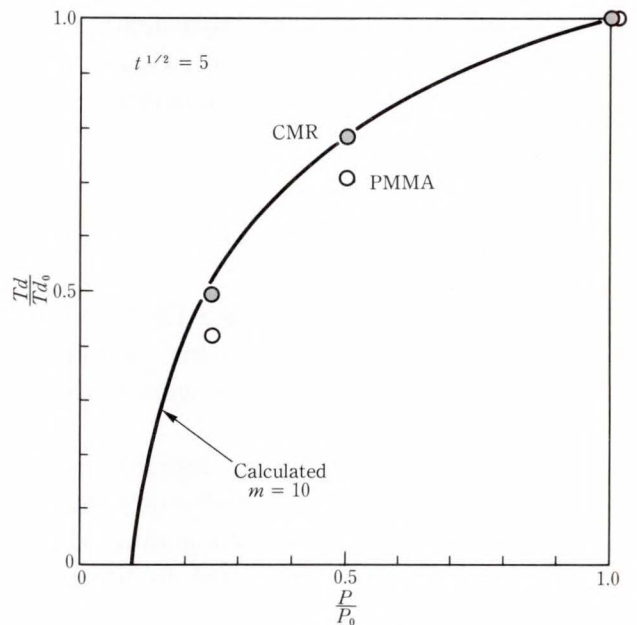


Fig. 9— $\frac{Td}{Td_0}$ vs. $\frac{P}{P_0}$.

$$Td = .2 \sqrt{D \cdot t} \operatorname{erfc}^{-1} \left(\frac{1}{r \cdot m} \right), \quad \dots (4)$$

where $m = \frac{n_0}{n_j}$ is constant.

So, the relative change of *Td* caused by a decrease in pressure is given by

$$\frac{Td}{Td_0} = \frac{\operatorname{erfc}^{-1} \left(\frac{1}{r \cdot m} \right)}{\operatorname{erfc}^{-1} \left(\frac{1}{m} \right)}, \quad \dots (5)$$

where *m* is operated as a fitting parameter.

To confirm the diffusion effect of oxygen, it is necessary to know the relationship between Td , t , and n_0 .

In an experiment to determine this relationship, the oxygen density was decreased by lowering the pressure of the exposure chamber, and the exposure time was varied by changing the glancing angle of the mirrors. The results are shown in Figs. 8 and 9.

Figure 8 shows that the relationship between Td and $t^{1/2}$ is proportional at pressures from 250 mbar to atmospheric pressure.

In Fig. 9, the points shown by the shaded circles for CMR were obtained experimentally at $t^{1/2} = 5$, and agreed well with calculated values when m was assumed to be ten. From Figs. 8 and 9, the negative taper depth Td was found to depend on diffusion of oxygen.

Using $m = 10$, the diffusion coefficient D is obtained by

$$D = \frac{Td_0^2}{4t \left\{ \operatorname{erfc}^{-1} \left(\frac{1}{m} \right) \right\}^2}, \quad \dots \dots (6)$$

and was calculated to be $4 \times 10^{-2} \mu\text{m}^2/\text{min}$. The diffusion coefficient for polymethyl methacrylate (PMMA) was the same as that for CMR.

Therefore, He and N_2 are desirable environments for precise pattern replication on CMR and PMMA by soft X-ray lithography. O_2 less than two percent is permitted in the atmosphere.

An example of a replicated resist pattern made using 3 μm -thick CMR in 1 atm He at a glancing angle of 10 mrad and a proximity gap of 30 μm is shown in Fig. 10.

3.4 Pattern replication accuracy

The pattern replication accuracy depends on the exposure dose, X-ray spectrum, and proximity gap⁵⁾.

At first, we examined the influence of exposure dose on pattern replication accuracy. Pattern accuracy was defined as the deviation of replicated resist pattern width (W_r) from the mask pattern width (W_m).

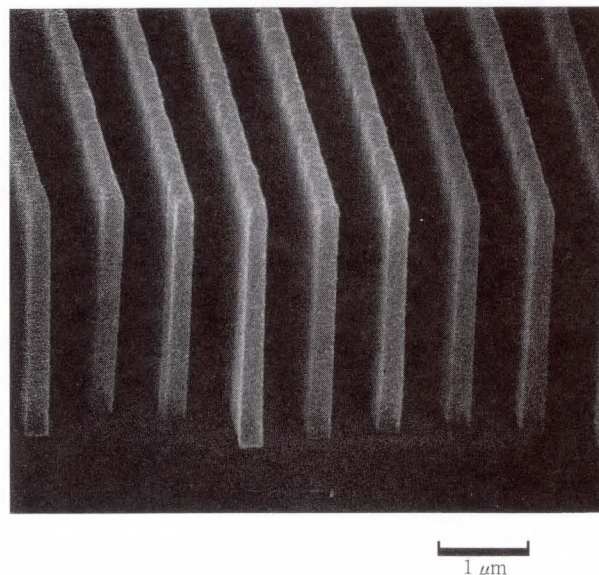


Fig. 10—High aspect 0.4 μm line and space patterns replicated into 3 μm -thick CMR using 10 mrad, 30 μm -gap, and He gas exposure.

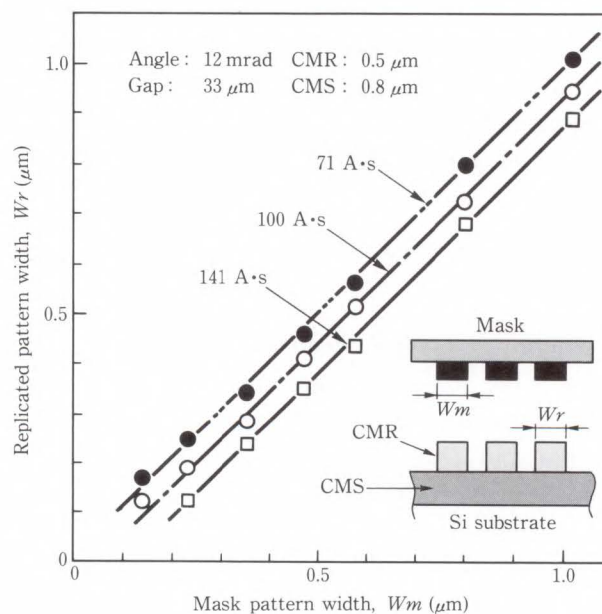


Fig. 11—Replicated resist pattern width of 0.5 μm -thick CMR for various mask pattern widths.

The resist used to evaluate the accuracy was 0.5 μm -thick CMR on 0.8 μm -thick CMS. The UV exposure described in Sec. 3.3 was used. Using a typical glancing angle of 12 mrad and a proximity gap of 33 μm , the relationship between W_m and W_r at different doses was examined in detail. The results are shown in

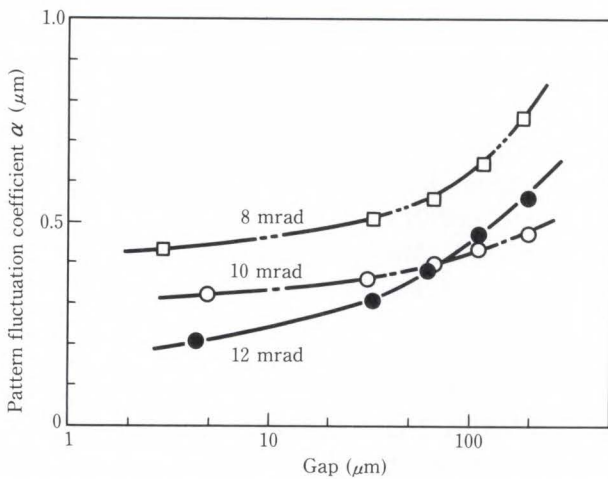


Fig. 12—Pattern width fluctuation coefficient vs. glancing angle of mirrors and proximity gap.

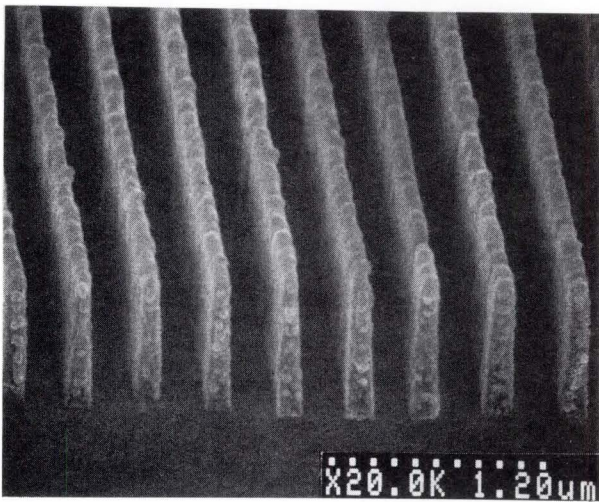


Fig. 13—0.2 μm line and space patterns replicated into 1 μm-thick CMR using 10 mrad, 30-μm gap, and He gas exposure.

Fig. 11. The dose was varied between 71 A·s and 141 A·s for exposures in atmospheric He.

The $Wm - Wr$ plot shows straight lines of spole 1 with a parallel shift for different doses. The degree of shift is nearly proportional to the logarithm of the dose difference. This can be approximated by the following equation

$$Wr = Wm - \alpha \cdot \log \left(\frac{D}{D_0} \right), \dots\dots\dots (7)$$

where D is the actual dose, D_0 is the optimum dose for $Wr = Wm$, α is the pattern width fluctuation coefficient which represents a sensitivity

of the pattern width to dose fluctuation. α was calculated to be ~ 0.3 .

We expected α to depend on the exposure conditions, the glancing angle of the mirrors (wavelength), and the proximity gap. In short, mask contrast and X-ray diffractions have an effect on the surface exposure intensity distribution of the CMR resist surface.

We then investigated the dependence of α . The results are shown in Fig. 12. The proximity gap was varied between 5 μm and 200 μm for three glancing angles: 8-, 10-, and 12-mrad. The results show that α decreases when the promixity gap decreases or the glancing angle increases.

A figure of $\alpha \leq 0.3$ was obtained at a gap of less than 30 μm and a glancing angle larger than 10 mrad. When $\alpha = 0.3$, a dose fluctuation of $\frac{D}{D_0} = 1.17$ can be permitted for a pattern width deviation of $Wm - Wr = 0.02 \mu m$ from Equation (7). An example of a 1.0 μm-thick, 0.2 μm line and space CMR pattern replicated at 10 mrad and 30 μm is shown in Fig. 13.

4. Conclusion

We constructed the BL-17C beamline for soft X-ray lithography experiments at the Photon Factory of the National Laboratory for High Energy Physics. We developed a method to measure the SR spectrum by He scattering. The fundamental characteristics of soft X-ray lithography using SR have been investigated using a spectrum measurement system.

Mask contrast, replicated resist profile, and replication accuracy were investigated for various exposure conditions.

The results can be summarized as follows.

- 1) We observed that the mask contrast and critical dose depended on the glancing angle.
- 2) The cause of the taper profiles in atmospheric exposures was found to be diffusion of oxygen. He and N₂ are desirable exposure environments for precise pattern replication on CMR and PMMA.
- 3) If the dose fluctuation is kept to within 17 percent, the replication error can be kept to within 0.02 μm using a proximity gap of 30 μm and a wavelength peak between 0.42 nm and 0.50 nm.

These results clearly show the fundamental characteristics of soft X-ray lithography using SR. The future development targets for soft X-ray lithography using SR are longer wavelengths and higher intensities using a thin Be window.

5. Acknowledgement

The authors wish to thank the staff at the Photon Factory of the National Laboratory for High Energy Physics for their valuable advice on the construction of the beamline.

References

- 1) Gotoh, S., Taguchi, T., Okamura, S., and Hisatsugu, T.: Measurement of Spectral and Spatial Intensity Distributions of Synchrotron Radiation in Soft X-ray Region by Means of Helium Gas Scattering. Proc. 3rd Int. Conf. Synchrotron Radiation Instrum., *Rev. Sci. Instrum.*, **60**, 7, pp. 2239-2242 (1989).
- 2) Taguchi, T., Gotoh, S., Okamura, S., and Hisatsugu, T.: X-ray Lithography Beam Line BL-17C at the Photon Factory. Proc. 6th Conf. Synchrotron Radiation Instrum., to be published in *Nucl. Instr. Meth.*, (1990).
- 3) Ogawa, T., Mochiji, K., Soda, Y., and Kimura, T.: Effects of the Secondary Electrons from Silicon Substrate on SR X-ray Lithography. *Jpn. J. Appl. Phys.*, **28**, p. 2070 (1989).
- 4) Tischer, P., and Hundt, E.: Profiles of Structure in PMMA by X-ray Lithography. Proc. 8th Int. Conf. Electron Ion Beam Sci. Technol., Bakish, R. ed., New Jersey, 1978, Electrochem. Soc., Princeton, p. 444.
- 5) Suzuki, M., Kaneko, T., and Saitoh, Y.: Replicated resist pattern resolution with synchrotron orbital radiation. *J. Vac. Sci. Technol.*, **B7**, 1, pp. 47-54 (1989).



Yoshimi Yamashita
Semiconductor Devices Laboratory
FUJITSU LABORATORIES, ATSUGI
Fujitsu Technical College, 1978
Specializing in Semiconductor Process



Hidetoshi Ishiwari
Semiconductor Devices Laboratory
FUJITSU LABORATORIES, ATSUGI
Maiya Technical Highschool, 1969
Specializing in Semiconductor Processes



Syunji Gotoh
Corporate Technology Advancement
Group Technology Development Div.
FUJITSU LIMITED
Bachelor of Applied Physics
The University of Tokyo, 1984
Master of Applied Physics
The University of Tokyo, 1986
Specializing in X-ray Lithography

FUJITSU

SCIENTIFIC & TECHNICAL JOURNAL

VOL.25, NOs.1-4

INDEX

 •SUBJECT INDEX •AUTHOR INDEX

Spring	1989	VOL.25, NO.1
--------	------	--------------

Summer	1989	VOL.25, NO.2
--------	------	--------------

Autumn	1989	VOL.25, NO.3
--------	------	--------------

Winter	1989	VOL.25, NO.4
--------	------	--------------

Special Issue on Printers and I/O Technology

Subject Index

(® marks are Review articles.)

A

An Analysis of Two-Component Magnetic Brush Development **4**, 251

● Masatoshi Kimura ● Makoto Kato ● Junzo Nakajima

C

CAD System for Three-Dimensional Layout Design **3**, 201

● Teruo Shibahara ● Naoki Nishimura ● Kazuhiro Takeuchi

Characterization of 8 K-bit Niobium Josephson Memory Cell Array for LSI Applications **2**, 135

● Hiromasa Hoko ● Takeshi Imamura

Clark-Type Oxygen Electrode and Biosensor Fabricated by Semiconductor Techniques **1**, 52

● Hiroaki Suzuki

Color Gamut Evaluation Method for Color Hard Copies **4**, 272

● Jun Moroo ● Toshio Konaka ● Tomohisa Mikami

Compact Three-Axis Accelerometer System (CTAS) for Microgravity Experiments **4**, 313

● Fumio Takei

D

Development of Tag Memory: MB81C51 **2**, 156

● Atushi Suzuki ● Kazuya Kobayashi ● Masashi Nagashima

Diamond-Film Synthesis Using DC Plasma Jet CVD **1**, 44

● Kazuaki Kurihara ● Ken-ichi Sasaki ● Motonobu Kawarada

® Digital Signal Processor **3**, 171

● Toshitaka Tsuda ● Hirohisa Gambe ● Ryusuke Hoshikawa

E

The Electrostatic Transfer of Toner Images **4**, 262

● Masatoshi Kimura ● Masahiro Wanou ● Hiroshi Nou

Environmental Test of FETEX-150 Digital Switching System **2**, 126

● Takashi Nara ● Katsuo Okuyama ● Masateru Tagami

Experimental System for Imaging In-Vivo Tissue Characteristics **3**, 194

● Keiichi Murakami ● Yuichi Sugiyama ● Isamu Yamada

F

A Filter-Alternating Color Scanner **4**, 279

● Shoji Suzuki ● Mitsuhiro Tsuda ● Masahiro Mori

565-Mbit/s Optical Fiber Transmission System **1**, 60

● Nobuhide Yamaguchi ● Kazuo Yamane ● Takashi Kihara

H

Holographic Fingerprint Sensor **4**, 287

● Seigo Igaki ● Shin Eguchi ● Takashi Shinzaki

I

Integrated CAD and Manufacturing System/FORM Design Support System 3, 215

● Hatsuko Kohroku ● Kenichi Abe

L

Low-Pressure Metalorganic Vapor Phase Epitaxial Growth of InGaAsP/InP Quantum Well Structures 2, 146

● Makoto Kondo ● Mitsuru Sugawara ● Takuya Fujii

M

MCPC Terminal for Satellite Communication 1, 26

● Mitsuru Seta ● Atsushi Yamashita ● Mitsuhiro Ono

N

A New Path Memory for Viterbi Decoders 1, 37

● Atsushi Yamashita ● Tadashi Nakamura ● Tadayoshi Katoh

O

1.6-Gbit/s Optical Fiber Transmission Equipment 3, 228

● Akira Miyauchi ● Masaru Onishi

P

Plastic Optical Fiber Doped with Organic Fluorescent Materials 2, 163

● Hisashi Sawada ● Akira Tanaka ● Noboru Wakatsuki

R

Reliability Analysis of FETEX-150 Digital Switching System 2, 113

● Yoshihiro Kubota ● Kousei Mano ● Hiroyuki Ohtaguro

S

Soft X-Ray Lithography Using Synchrotron Radiation 4, 317

● Yoshimi Yamashita ● Syunji Gotoh ● Hidetoshi Ishiwari

Ⓡ Space Technology 1, 1

● Tomoyoshi Yamashita ● Koji Ishizaka ● Takashi Uchiyama

SVEX: Switching Program Verification Expert System 4, 306

● Jun'ichi Yamazaki ● Kiyoshi Miyazaki ● Tadamichi Suzuki

T

Ⓡ Technology for Pattern Information Processing 2, 81

● Masumi Yoshida ● Yoshikazu Ito ● Yasuhiro Nara

Thermal Expansion of Glass/Ceramic Composites for Multilayer Ceramic Circuit Boards 1, 73

● Yoshihiko Imanaka ● Shigenori Aoki ● Nobuo Kamehara

W

Wavelength Independent Grating Lens System 4, 297

● Masayuki Kato ● Satoshi Maeda ● Fumio Yamagishi

Author Index

(R marks are Review articles.)

A

Abe Kenichi see **Kohroku** Hatsuko
Aoki Shigenori see **Imanaka** Yoshihiko

E

Eguchi Shin see **Igaki** Seigo

F

Fujii Takuya see **Kondo** Makoto

G

Gambe Hirohisa see **Tsuda** Toshitaka
Gotoh Syunji see **Yamashita** Yoshimi

H

Hoko Hiromasa
Characterization of 8 K-bit Niobium Josephson Memory Cell Array for LSI
Applications **2**, 135
Hoshikawa Ryusuke see **Tsuda** Toshitaka

I

Igaki Seigo
Holographic Fingerprint Sensor **4**, 287
Imamura Takeshi see **Hoko** Hiromasa
Imanaka Yoshihiko
Thermal Expansion of Glass/Ceramic Composites for Multilayer Ceramic Circuit
Boards **1**, 73
Ishiwari Hidetoshi see **Yamashita** Yoshimi
Ishizaka Koji see **Yamashita** Tomoyoshi
Ito Yoshikazu see **Yoshida** Masumi

K

- Kamehara** Nobuo see **Imanaka** Yoshihiko
Kato Makoto see **Kimura** Masatoshi
Kato Masayuki
 Wavelength Independent Grating Lens System **4**, 297
Katoh Tadayoshi see **Yamashita** Atsushi
Kawarada Motonobu see **Kurihara** Kazuaki
Kihara Takashi see **Yamaguchi** Nobuhide
Kimura Masatoshi
 An Analysis of Two-Component Magnetic Brush Development **4**, 251
 The Electrostatic Transfer of Toner Images **4**, 262
Kobayashi Kazuya see **Suzuki** Atsushi
Kohroku Hatsuko
 Integrated CAD and Manufacturing System/FORM Design Support System **3**, 215
Konaka Toshio see **Moroo** Jun
Kondo Makoto
 Low-Pressure Metalorganic Vapor Phase Epitaxial Growth of InGaAsP/InP
 Quantum Well Structures **2**, 146
Kubota Yoshihiro
 Reliability Analysis of FETEX-150 Digital Switching System **2**, 113
Kurihara Kazuaki
 Diamond-Film Synthesis Using DC Plasma Jet CVD **1**, 44

M

- Maeda** Satoshi see **Kato** Masayuki
Mano Kousei see **Kubota** Yoshihiro
Mikami Tomohisa see **Moroo** Jun
Miyauchi Akira
 1.6-Gbit/s Optical Fiber Transmission Equipment **3**, 228
Miyazaki Kiyoshi see **Yamazaki** Jun'ichi
Mori Masahiro see **Suzuki** Shoji
Moroo Jun
 Color Gamut Evaluation Method for Color Hard Copies **4**, 272
Murakami Keiichi
 Experimental System for Imaging In-Vivo Tissue Characteristics **3**, 194

N

- Nagashima** Masashi see **Suzuki** Atsushi
Nakajima Junzo see **Kimura** Masatoshi
Nakamura Tadashi see **Yamashita** Atsushi
Nara Takashi
 Environmental Test of FETEX-150 Digital Switching System **2**, 126
Nara Yasuhiro see **Yoshida** Masumi
Nishimura Naoki see **Shibahara** Teruo
Nou Hiroshi see **Kimura** Masatoshi

O

Ohtaguro Hiroyuki see **Kubota** Yoshihiro
Okuyama Katsuo see **Nara** Takashi
Onishi Masaru see **Miyauchi** Akira
Ono Mitsuhiro see **Seta** Mitsuru

S

Sasaki Ken-ichi see **Kurihara** Kazuaki
Sawada Hisashi
 Plastic Optical Fiber Doped with Organic Fluorescent Materials **2**, 163
Seta Mitsuru
 MCPC Terminal for Satellite Communication **1**, 26
Shibahara Teruo
 CAD System for Three-Dimensional Layout Design **3**, 201
Shinzaki Takashi see **Igaki** Seigo
Sugawara Mitsuru see **Kondo** Makoto
Sugiyama Yuichi see **Murakami** Keiichi
Suzuki Atushi
 Development of Tag Memory: MB81C51 **2**, 156
Suzuki Hiroaki
 Clark-Type Oxygen Electrode and Biosensor Fabricated by Semiconductor Techniques
 1, 52
Suzuki Shoji
 A Filter-Alternating Color Scanner **4**, 279
Suzuki Tadamichi see **Yamazaki** Jun'ichi

T

Tagami Masateru see **Nara** Takashi
Takei Fumio
 Compact Three-Axis Accelerometer System (CTAS) for Microgravity Experiments **4**, 313
Takeuchi Kazuhiro see **Shibahara** Teruo
Tanaka Akira see **Sawada** Hisashi
Tsuda Mitsuhiro see **Suzuki** Shoji
Tsuda Toshitaka
 Ⓜ Digital Signal Processor **3**, 171

U

Uchiyama Takashi see **Yamashita** Tomoyoshi

W

Wakatsuki Noboru see **Sawada** Hisashi
Wanou Masahiro see **Kimura** Masatoshi

Y

- Yamada** Isamu see **Murakami** Keiichi
- Yamagishi** Fumio see **Kato** Masayuki
- Yamaguchi** Nobuhide
565-Mbit/s Optical Fiber Transmission System **1**, 60
- Yamane** Kazuo see **Yamaguchi** Nobuhide
- Yamashita** Atsushi
A New Path Memory for Viterbi Decoders **1**, 37
- Yamashita** Atsushi see **Seta** Mitsuru
- Yamashita** Tomoyoshi
Ⓡ Space Technology **1**, 1
- Yamashita** Yoshimi
Soft X-Ray Lithography Using Synchrotron Radiation **4**, 317
- Yamazaki** Jun'ichi
SVEX: Switching Program Verification Expert System **4**, 306
- Yoshida** Masumi
Ⓡ Technology for Pattern Information Processing **2**, 81

Overseas Offices

Abu Dhabi Office

8th Floor, A1 Masood Tower,
P.O. Box 322, Abu Dhabi, U.A.E.
Telephone: (971-2)-333440
FAX: (971-2)-333436

Algiers Office

6, Boulevard Colonel,
Amirouche, Alger, Algeria
Telephone: (213)-2-78-5542
Telex: 408-67522

Amman Office

P.O. Box 5420, Ammán, Jordan
Telephone: (962)-6-66241
FAX: (962)-6-662417

Bangkok Office

Room 405, 4th Floor, Dusit
Thani Bldg., 1-3, Rama IV,
Bangkok, Thailand
Telephone: (66-2)-236-7930
FAX: (66-2)-238-3666

Beijing Office

Room 1601, Scite Tower
Jianguomen-wai Dajie, Beijing,
People's Republic of China
Telephone: (86-1)-512-3610
FAX: (86-1)-512-9041

Bogotá Office

Cra. 13 No. 27-50,
Edificio Centro Internacional
Tequendama, Oficina No. 326.
Bogotá, D.E. Colombia
Telephone: (57-1)-296-8258
FAX: (57-1)-286-7148

Hawaii Branch

6660 Hawaii Kai Drive, Honolulu,
HI 96825, U.S.A.
Telephone: (1-808)-395-2314
FAX: (1-808)-396-0059

Indonesia Project Office

16th Floor, Skyline Bldg.,
Jalan M.H. Thamrin No. 9,
Jakarta, Indonesia
Telephone: (62-21)-3105981
FAX: (62-21)-3105983

Jakarta Office

16th Floor, Skyline Bldg.,
Jalan M.H. Thamrin No. 9,
Jakarta, Indonesia
Telephone: (62-21)-333245
FAX: (62-21)-327904

Kuala Lumpur Office

Letter Box No. 47, 22nd Floor,
UBN Tower No. 10, Jalan P.
Ramlee, 50250, Kuala Lumpur,
Malaysia
Telephone: (60-3)-238-4870
FAX: (60-3)-238-4869

London Office

2, Longwalk Road, Stockley Park,
Uxbridge, Middlesex, UB11 1AB,
England
Telephone: (44-1)-573-4444
FAX: (44-1)-573-2643

Munich Office

c/o D V 18 Siemens AG, Otto-
Hahn-Ring 6, D-8000, München
83, F.R. Germany
Telephone: (49-89)-636-3244
FAX: (49-89)-636-45345

New Delhi Office

Flat No. 517-B, 5th Floor, World
Trade Centre, Barakhamba Lane,
New Delhi, 110001, India
Telephone: (91-11)-331-1311
FAX: (91-11)-332-1321

New York Office

680 Fifth Avenue, New York,
N.Y. 10019, U.S.A.
Telephone: (1-212)-265-5360
FAX: (1-212)-541-9071

Paris Office

Batiment Aristote,
Rue Olof Palme 94006,
Creteil Cedex, France
Telephone: (33-1)-4-399-0897
FAX: (33-1)-4-399-0700

Shanghai Office

Room 1504 Ruijin Bldg.,
205 Maoming Road South,
Shanghai, People's Republic
of China
Telephone: (86-21)-336-462
FAX: (86-21)-336-480

Taipei Office

Sunglow Bldg. 66, Sung Chiang
Road, Taipei, Taiwan
Telephone: (886-2)-561-7715
FAX: (886-2)-536-7454

Washington Office

Republic Place, 1776 Eye Street,
N.W. Washington D.C., U.S.A.

Overseas Subsidiaries

		Telephone	Telex
FKL Dong-Hwa Ltd.	338-13, Daehong-Ri, Sunghwan-Eub, Chunwon-Gun, Chungnam, Republic of Korea	(82-417)-4-3660	(82-417)-63-3671
Fujian Fujitsu Communications Software Ltd.	Wuliting Fuma Road, Fuzhou, Fujian, People's Republic of China	(86-591)-560070	(86-591)-56-0022
Fujitsu America, Inc.	3055 Orchard Drive, San Jose, CA 95134-2017, USA	(1-408)-432-1300	(1-408)-432-1318
Fujitsu Australia Ltd.	475 Victoria Ave., Chatswood, NSW 2067, Australia	(61-2)-410-4555	(61-2)-411-8603
Fujitsu Australia Software Technology Pty. Ltd.	1st Floor, Techway House, Forest Corporate Park, 18 Rodborough Road, Frenchs Forest, N.S.W. 2086, Australia	(61-2)-975-2922	(61-2)-975-2899
Fujitsu Business Communication System, Inc. (Sales Headquarter)	3190 Mira Loma Ave., Anaheim, CA 92806-1906, USA	(1-714)-630-7721	(1-714)-630-7660
Fujitsu Canada, Inc.	2411 West 14th Street, Tempe, AZ 85281, USA	(1-602)-921-5900	(1-602)-921-5999
Fujitsu Component (Malaysia) Sdn. Bhd.	6280 Northwest Drive, Mississauga, Ontario, Canada L4V 1J7	(1-416)-673-8666	(1-416)-673-8677
Fujitsu Component of America, Inc.	No. 1, Lorong Satu, Kawasan Perindustrian Parit Raja, 86400 Batu Pahat, Johor, Malaysia	(60-7)-482111	(60-7)-481-771
Fujitsu Customer Service of America, Inc.	3320 Scott Boulevard, Santa Clara, CA 95054-3197, USA	(1-408)-562-1000	(1-408)-748-7655 or (1-408)-727-0355
Fujitsu Deutschland GmbH	12670 High Bluff Drive, San Diego, CA 92130-2013, USA	(1-619)-481-4004	(1-619)-481-5175
Fujitsu do Brasil Ltda.	Rosenheimer Strasse 145, D-8000, München 80, F.R. Germany	(49-89)-413010	(49-89)-652143
Fujitsu Electronics (Singapore) Pte. Ltd.	Rua Manoel da Nóbrega, 1280, 2 ^o Andar, C.E.P. 04001, São Paulo, SP, Brazil	(55-11)-885-7099	(55-11)-885-9132
Fujitsu España, S.A.	7500A, Beach Road, #05-301/2 The Plaza, Singapore 0719, Singapore	(65)-296-1818	(65)-298-1571
Fujitsu Europe Ltd.	Edificio Torre Europa 5 ^a , Paseo de la Castellana, 95, 28046 Madrid, Spain	(34-1)-581-8000	(34-1)-581-8300
Fujitsu Finance (U.K.) PLC	2, Longwalk Road, Stockley Park, Uxbridge, Middlesex, UB11 1AB, England	(44-1)-573-4444	(44-1)-573-2643
Fujitsu Hong Kong Ltd.	2, Longwalk Road, Stockley Park, Uxbridge, Middlesex, UB11 1AB, England	(44-1)-573-4444	(44-1)-573-2643
Fujitsu Imaging Systems of America, Inc.	Room 2521, Sun Hung Kai Centre, 30 Harbour Road, Hong Kong	(852-5)-8915780	(852-5)-721724 or (852-5) 8383630
Fujitsu International Finance (Netherlands) B.V.	3 Corporate Drive, Commerce Park, Danbury, CT 06810, USA	(1-203)-796-5400	(1-203)-796-5665 or (1-203)-796-5723
Fujitsu Italia S.p.A.	Officia 1, De Boelelaan 7, 1083 HJ Amsterdam, The Netherlands	—	—
Fujitsu Korea Ltd.	Via Melchiorre, Gioia No. 8, 20124 Milano, Italy	(39-2)-657-2741	(39-2)-657-2257
Fujitsu Microelectronics Asia Pte. Ltd.	9th Floor, Korean Reinsurance Bldg., 80, Susong-Dong, Chongro-Gu, Seoul Special City, Republic of Korea	(82-2)-739-3281	(82)-417-63-3671
Fujitsu Microelectronics, Inc.	No. 2, Second Chin Bee Road, Jurong Town, Singapore 2261, Singapore	(65)-265-6511	(65)-265-6275
Fujitsu Microelectronics Ireland Limited	3545 North First Street, San Jose, CA 95134-1804, USA	(1-408)-922-9000	(1-408)-432-9044
Fujitsu Microelectronics Italia S.r.l.	Greenhills Centre, Greenhills Rd., Tallaght, Dublin 24, Ireland	(353-1)-520744	(353-1)-520539
Fujitsu Microelectronics Limited	Centro Direzionale, Milanofiori, Strada No. 4-Palazzo A2, 20090 Assago-Milano, Italy	(39-2)-824-6170	(39-2)-824-6189
Fujitsu Microelectronics (Malaysia) Sdn. Bhd.	Hargrave House, Belmont Road, Maidenhead, Berkshire SL6 6NE, U.K.	(44-628)-76100	(44)-628-781484
Fujitsu Microelectronics Pacific Asia Limited	Lot P.T. 717, Jalan Persiaran Sabah, Kawasan Perindustrian HICOM, Section 26, 40000 Shah Alam, Selangor Darul Ehsan, Malaysia	(60-3)-511-1155	(60-3)-511-1227
Fujitsu Microsystems of America, Inc.	805, Tsim Sha Tsui Centre, West Wing, 66 Mody Road, Kowloon, Hong Kong	(852-3)-7320100	(852-3)-722-7984
Fujitsu Mikroelektronik GmbH	3025 Orchard Parkway, San Jose, CA 95134-2017, USA	(1-408)-434-1160	(1-408)-434-0359
Fujitsu Network Switching of America, Inc.	Lyoner Strasse 44-48, Arabella Centre 9, OG/A, 6000 Frankfurt/Niederrad 71, F.R. Germany	(49-69)-66320	(49-69)-6632122
Fujitsu New Zealand Ltd.	4403 Bland Road, Somerset Park, Raleigh, NC 27609, USA	(1-919)-790-2211	(1-919)-790-8376
Fujitsu Nordic AB	6th Floor, National Insurance House, 119-123 Featherston Street, Wellington, New Zealand	(64-4) 733-420	(64-4)-733-429
Fujitsu Philippines, Inc.	Torggatan 8, S-171 54 Solna, Sweden	(46-8)-764-7690	(46-8)-28-0345
Fujitsu (Singapore) Pte. Ltd.	2nd Floor, United Life Bldg., Pasay Road, Legaspi Village, Makati, Metro Manila, Philippines	(63-2)-85-49-51	(63-2)-817-7576
Fujitsu Systems Engineering of America, Inc.	200, Cantonment Road, #11-01 South Point, Singapore 0208, Singapore	(65)-224-0159	(65)-225-5075
Fujitsu Systems of America, Inc.	2986 Oakmead Village Court, Santa Clara, CA 95054, USA	(1-408)-988-8012	(1-408)-492-1982
Fujitsu (Thailand) Co., Ltd.	12670 High Bluff Drive, San Diego, CA 92130-2013, USA	(1-619)-481-4004	(1-619)-481-4093
Fujitsu Vitória Computadores e Serviços Ltda.	3rd Floor, Olympia Thai Bldg., 444 (3rd Floor), Rachadaphisek Road, Bangkok 10310, Thailand	(662-512)-1736	(662-513)-2574
Information Switching Technology Pty. Ltd.	Avenida Nossa, Senhora da Penha, 570, 8 ^o Andar, Praia do Canto-Vitória-Espirito Santo, Brazil	(55-27)-225-0355	(55-27)-225-0954
Intellistor, Inc.	Level 32, 200 Queen Street, Melbourne 3000, Australia	(61-3)-670-4755	—
Tatung-Fujitsu Co., Ltd.	2120 Miller Drive, Longmont, CO 80501, USA	(1-303)-678-0697	—
	5 Floor Tatung Bldg., 225, Nanking East Road 3rd Section, Taipei, Taiwan	(886-2)-713-5396	(886-2)-717-4644

(The information here as of December 28, 1989)

FUJITSU LIMITED

6-1, Marunouchi 1-chome, Chiyoda-ku, Tokyo 100, Japan

Phone: National (03) 216-3211 International (Int'l Prefix) 81-3-216-3211 Telex: J22833 Cable: "FUJITSULIMITED TOKYO"